Thermodynamic Stability and Implications of Anisotropic Boundary Particles

by

Ellen J. Siem

B.S. Materials Science & Engineering
Northwestern University, 2000

SUBMITTED TO THE DEPARTMENT OF MATERIALS SCIENCE & ENGINEERING
IN PARTIAL FULFILLMENT OF THE REQUIREMENTS FOR THE DEGREE OF

DOCTOR OF PHILOSOPHY IN MATERIALS SCIENCE & ENGINEERING
AT THE
MASSACHUSETTS INSTITUTE OF TECHNOLOGY

FEBRUARY 2005

Signature of Author: _____

Department of Materials Science & Engineering
January 10, 2005

Certified by: _____

W. Craig Carter
Lord Foundation Professor of Materials Science & Engineering
Thesis Supervisor

_____

Samuel M. Allen
POSCO Professor of Physical Metallurgy
Thesis co-Supervisor

Accepted by: _____

Carl V. Thompson II
Stavros Salapatas Professor of Materials Science & Engineering
Chair, Departmental Committee for Graduate Students

Thermodynamic Stability and Implications of Anisotropic Boundary Particles

by

Ellen J. Siem

Submitted to the Department of Materials Science and Engineering on January 10, 2005 in Partial Fulfillment of the Requirements for the Degree of Doctor of Philosophy in Materials Science and Engineering

ABSTRACT

Many material properties depend on grain and phase boundary morphology. Equilibrium boundary and particle morphologies are determined by their interactions through interfacial free energy. Currently, the determination of boundary and particle morphology is, for most materials systems, experimentally difficult.

This thesis demonstrates that geometric constructions from capillarity theory for anisotropic interfaces cannot predict boundary and particle morphology, even in systems with uniform temperature, pressure, and chemical potentials. In this thesis, numerical methods are developed and implemented for calculations of anisotropic particles of fixed volumes attached to one or more interfaces that are also subject to specified constraints.

Some boundary properties can be found experimentally, such as: the crystallographic misorientation across the boundary, the fixed average unit normal to the boundary, the Wulff shape ($\mathcal{W}$) of the boundary, and the particle $\mathcal{W}$ within each grain or phase abutting the boundary. These properties become model parameters in addition to the $\mathcal{W}$ associated with each interface. This thesis also presents methods of generating algebraic expressions for interfacial free energy densities, $\gamma^{\mathcal{W}}(\hat{\mathbf{n}})$, that produce $\mathcal{W}$ for a given symmetry.

Calculated examples show that equilibrium configurations are formed from portions of the boundary and particle $\mathcal{W}$s and do not contain orientations absent from the respective $\mathcal{W}$s. Under the constraint that the pressure difference across

a boundary is zero, the boundary will develop a constant weighted mean curvature (κ_γ) of zero. Generally, a boundary is nonplanar in the neighborhood of an attached particle—even when anisotropic interfacial free energies do not produce faceting—and maintains a $\kappa_\gamma = 0$ while the boundary particles maintain a nonzero κ_γ. This is consistent with independent observations of Pb–rich particles at grain boundaries in dilute Pb–Al alloys.

Predicted particle/boundary morphologies give a trade-off between boundary and particle interface—a particle replaces some boundary but also produces boundary area through local distortions. This result has several implications. The transition to perfect wetting requires a larger boundary energy density. The steady-state heterogeneous nucleation rate is increased when facets appear on the nucleus, but the increase is diminished if the boundary distorts.

A corollary result presented in this thesis, that particles can induce rotations or serration through torques, has implications in microstructural stability and illustrates avenues for future research.

Thesis Supervisor: W. Craig Carter
Title: Lord Foundation Professor of Materials Science & Engineering

Thesis co-Supervisor: Samuel M. Allen
Title: POSCO Professor of Physical Metallurgy

Acknowledgments

I would like to thank W. Craig Carter, my advisor, for: (a) introducing me to an enjoyable research area and several colleagues concerned with "good" science—*i.e.*, with applying fundamental principles to produce results that are correct and useful to others; (b) encouraging me to teach—*i.e.*, to embark on a career that I have found an intense interest in; (c) being a local hero—*i.e.*, always doing the right thing and setting a good example for everyone; and (d) going beyond the call of duty for his students, constantly encouraging them to do their best in science, in their family, and in their community.

I would also like to thank Sam Allen, my co-advisor, for: (a) discussing this research with me frequently and consistently providing insightful, direct feedback; (b) providing me with the opportunity to practice teaching as an assistant to the undergraduate materials thermodynamics and kinetics courses; (c) being a local hero; and (d) setting aside tasks at hand to ardently maintain the "open door" policy that applies to all of his students.

I owe a big thanks to the other members of my thesis committee for devoting countless hours becoming acquainted with my research. I would like to individually thank Chris Schuh for asking difficult questions, Dominique Chatain for critical reviews of the thesis and papers following from this research, and Ken Russell for sharing his passion for Wulff shapes.

The micrographs in this thesis were taken by Uli Dahmen, Tamara Radetic, and Lihua Zhang. I would like to thank them for use of the micrographs and Uli Dahmen for funding me as a visitor to the National Center of Electron Microscopy at LBNL during 2003.

I would also like to thank my thesis committee, Erik Johnson, my mother, and especially Ming Tang for a close read of the thesis.

Finally, I would like to thank my family. My mother, my father, my little brother Ben, and my big brother Mike are my primary source of inspiration.

Contents

List of Figures

List of Tables

Part I

Introduction

Chapter 1

Research Summary

In two dimensions ($\mathbf{R^2}$), the equilibrium shape of a fixed area attached to a boundary separating two grains or phases (denoted C_1 and C_2) at constant temperature, pressure, and chemical potential for each species can be determined, exactly, by a geometric construction when the following four properties are known: the boundary energy per unit length, the boundary orientation, and the oriented Wulff shape of the fixed area on both sides of the boundary ($\mathcal{W}_1'$ and $\mathcal{W}_2'$, Wulff shapes oriented with respect to the embedding crystals, C_1 and C_2, respectively).

In three dimensions ($\mathbf{R^3}$), the determination of the equilibrium shape of a fixed volume is difficult when the boundary is not constrained to remain planar: truncated portions of $\mathcal{W}_1'$ and $\mathcal{W}_2'$ meet the boundary along a triple line that may depart from the original (particle-free) boundary if the boundary, or at least one of the Wulff shapes, is anisotropic. For small particle volumes, elastic strains are negligible. In the absence of other such external influences, the equilibrium configuration follows a minimization in the total interfacial free energy, and the degree of Wulff shape truncation is proportional to the net removal of boundary energy.

Because particles attached to boundaries frequently influence the mechanical, chemical, and electrical properties of a polycrystalline material, a principal question is: What is the energy-minimizing geometry for a boundary particle in $\mathbf{R^3}$?

This thesis provides numerical methods for determining the equilibrium configuration of a boundary particle. The methods apply to particles and boundaries of *any* interfacial free energy density. The methods can be extended to particles

attached to an intersection of distinct boundaries (*e.g.*, grain or heterophase edges and corners), and the calculated results can be used to predict, or interpret, microstructures that can be observed through transmission electron microscopy.

The thesis is divided into four parts. Part I defines interfacial free energy and presents known particle shape constructions that approximate the observed particle shapes. It further defines the central problem addressed by the thesis and shows that the solution is applicable to general questions coupling anisotropy and boundary particles.

Part II gives the methods of calculating the equilibrium structure of anisotropic particles attached to isotropic boundaries in $\mathbf{R^3}$ developed for this work. Specifically, it demonstrates how anisotropic interfacial free energy density functions, $\gamma(\hat{\mathbf{n}})$, can be combined with Rodrigues rotation matrices and the energy minimization methods of the *Surface Evolver* to calculate particles of fixed volume attached to boundaries characterized by a known free energy density (γ_B), a fixed crystallographic misorientation ($\vec{\mathbf{R}}_\Phi$) that maps C_2 into coincidence with C_1, and a fixed *average* boundary orientation ($\hat{\mathbf{n}}_B^{avg}$) that separates C_1 from C_2.

Part III provides basic examples that show the utility of the methods. The examples calculate configurations that could appear in a microstructure that results from minimizations in interfacial free energy. Part III discusses three of these examples, outlined below, in detail.

Example one (Ch. 9) considers the heterogeneous nucleation of a particle at an isotropic boundary. Crystallographic misorientation is fixed, and the nucleation barrier for an anisotropic boundary particle relative to an isotropic one of specified dihedral angle is calculated as a function of $\mathcal{W}_1$, $\mathcal{W}_2$, γ_B, and $\hat{\mathbf{n}}_B^{avg}$. Numerical approximations to the exact configuration show that the simplifying geometrical assumption of Lee and Aaronson, which uses catenoid surfaces to approximate the boundary distortion resulting from particle anisotropy, is fairly accurate. This thesis adds five degrees of complexity to the original work of Lee and Aaronson, and the resulting calculations show the nucleation barrier to depend more strongly on particle Wulff shape and γ_B than $\hat{\mathbf{n}}_B^{avg}$ when $\vec{\mathbf{R}}_\Phi$ is fixed.

Example two (Ch. 10) considers the effect of an anisotropic boundary energy ($\gamma_B(\hat{\mathbf{n}}_B)$) that derives from the Read Shockley model for low angle grain boundaries in crystals with primitive cubic structures. This example shows that even *isotropic*

particles may induce boundary distortion, and that particular heterogeneous nucleation sites (boundary orientations) may be more favorable when the boundary is anisotropic.

Example three (Ch. 11.2.2) considers two classes of torque driven by changes to boundary particle configuration that reduce the total interfacial free energy. For this example, γ_B is isotropic in $\hat{\mathbf{n}}_B$ and $\vec{\mathbf{R}}_\Phi$. The first class of torque acts on the boundary and shows that a reduction in interfacial free energy may accompany boundary rotation when $\vec{\mathbf{R}}_\Phi$ is fixed—in other words, the particle may rotate the boundary to produce a geometry of lower free energy. The second class of torque acts on one grain for a fixed $\hat{\mathbf{n}}_B^{avg}$—here, the particle may rotate a grain. A general torque would consist of components tending to rotate the boundary as well as the grain. To focus on the effect of boundary particle anisotropy, general torques and constraints imposed by neighboring grains are not considered.

Part IV summarizes the contributions of this thesis and the results from the three examples detailed in Part III. Part IV also outlines steps for modifications to the model developed in Part II and lists further applications of the model to problems related to microstructure.

Chapter 2

Interfacial Free Energy, Boundaries, and Interfaces

2.1 Interfacial Free Energy

Results from this thesis apply to equilibrium at constant temperature, pressure, and chemical potential of each species. It is assumed that equilibrium is achieved when interfacial free energy is minimized. Interfacial free energy is that part of a system's free energy in excess of the contributions from the bulk phases that abut to form an interface [1, 2, 3]. Interfaces can be treated as mathematically sharp, composed of differential elements of area, and joining bulk phases that are completely homogeneous. The interfacial free energy density, γ, is an intensive quantity giving the free energy per unit area of interface.

Interfacial free energy is often dependent on the unit normal to the interface, which is called the *orientation* of the interface in this thesis. Common experimental methods of determining relative interfacial free energy values for interfaces in solids include measurements of: (1) dihedral angles at junctions of three or more interfaces separating bulk grains or phases [4, 5, 6, 7]; (2) the equilibrium shapes of small particles [8, 9, 10], voids, or bubbles [11]; (3) zero-creep techniques in thin foils and fine wires [12]; and (4) the energy released during grain growth [12, 13]. There are other methods, but they are difficult to apply with precision and are therefore not used extensively [13].

2.2 Equilibrium of Bulk Interfaces: *Boundaries*

In this work, bulk interfaces—interfaces of fixed average unit normal separating two phases or grains that are infinite in extent—are distinguished from interfaces bounding particles. For clarity, bulk interfaces are collectively called *boundaries*, while *interface* is reserved for particle surface.

Consider a system at constant T, p, and $\vec{\mu}$ containing boundaries, where T is the temperature, p is the pressure, and $\vec{\mu}$ is a vector representing the chemical potential of each species [14]. For this system, equilibrium is determined by the minimization of

$$\int \gamma_{\mathrm{B}}(\hat{\mathbf{n}}_{\mathrm{B}})dA \tag{2.1}$$

where $\gamma_{\mathrm{B}}(\hat{\mathbf{n}}_{\mathrm{B}})$ is the boundary free energy density as a function of the unit normal to the boundary, $\hat{\mathbf{n}}_{\mathrm{B}}$; dA is an infinitesimal area; and the integral is taken over all boundaries. (Note that the subscript B is used to address both phase and grain boundaries, but the subscript GB is used when grain boundaries are discussed explicitly.)

There are many physical examples of systems containing only isotropic boundaries [15, page 107–109] with direct applications in, *e.g.*, block copolymers [16] and ternary oil water systems [17, 18]. For isotropic boundaries, equilibrium requires that boundary area be a minimum [19, 20].

Material systems are often observed [21, 22, 23] to have *anisotropic* boundaries. For these cases, $\gamma_{\mathrm{B}}(\hat{\mathbf{n}}_{\mathrm{B}})$ must remain in the integrand of Eq. (2.1), and equilibrium occurs when the boundaries assume a geometry that minimizes the sum of the area of all boundary orientations, each weighted by its interfacial free energy density [14, 24, 25, 26].

2.3 Equilibrium of Interface Bounding Finite Volumes: *Interfaces*

For a particle interface, equilibrium is determined by a minimization of

$$\int \gamma(\hat{\mathbf{n}}) dA - \Delta p \int dV \tag{2.2}$$

where the first integral is taken over all particle interface and boundary, the second integral is taken over the particle volume, and Δp, the change in pressure across the interface, is the Lagrange multiplier for the volume constraint.

There are many examples of fixed volumes with an isotropic interface [15, page 109–123]. For isotropic interfaces, equilibrium occurs when the interfacial area of a fixed volume is minimized, giving an equilibrium Δp for a given volume and γ. The Young-Laplace equation [1, 27, 28] relates Δp to the mean curvature of an interface,

$$\Delta p = \gamma\kappa = \gamma\frac{\delta A}{\delta V} \tag{2.3}$$

where γ is the free energy density and κ is the mean curvature of the interface [29]. The second equality introduces a definition of κ as the change in area, δA, that occurs when the interface is moved along its normal to sweep out a volume δV [29]. Mean curvature is an important geometrical property, appearing as a parameter in, *e.g.*, studies of grain growth [4] and models of periodic structures [30] applicable to the coarsening of intermediate-stage sintering microstructures [31, 32, 33].

For *anisotropic* particle interfaces, stable equilibria occur when the total energy of the interface bounding the fixed volume is minimized. For these cases, an anisotropic analogue to mean curvature applies [29]. Anisotropic equilibrium particle shapes can be obtained through constructions reviewed in Ch. 4.1.2.

Chapter 3

Particle Shapes in Materials

3.1 Observations

Particles fully embedded within one phase and particles attached to boundaries are frequently observed microstructural features. The Wulff construction, summarized in Ch. 4.1.2, gives the equilibrium shape—the Wulff shape—of an isolated particle. Wulff shapes of single crystalline particles embedded within a solid phase have been observed in a number of material systems [10, 34, 35, 36, 37], and observations of equilibrated negative crystals (voids or bubbles containing a fluid) [11, 38, 39, 40, 41] are known to produce central inversions to a Wulff shape [25, 42].

The Winterbottom and Summertop constructions (Ch. 4.2.1–4.2.2) apply, respectively, to particles attached to a single boundary and those attached to the intersection of multiple boundaries. In these constructions, boundaries are non-deformable, and particle volume lies completely to one side of each boundary to which it is attached. (This thesis defines boundaries as *non-deformable* if boundary orientation, $\hat{\mathbf{n}}_{\mathrm{B}}$, remains everywhere unchanged. Otherwise, a boundary is *deformable*, and the average boundary orientation, $\hat{\mathbf{n}}_{\mathrm{B}}^{avg}$, is fixed through a global constraint while local orientations, $\hat{\mathbf{n}}_{\mathrm{B}}$, are unconstrained.) Winterbottom and Summertop shapes have been studied most extensively for particles attached to flat, inert substrates [43, 44, 45, 46] but also appear at non-deformable interfaces within materials when particle size is small relative to the extent of the non-deformable

interface [47, 48].

The double Winterbottom construction for non-deformable boundaries (Ch. 4.2.3) applies to cases for which a fraction of the particle volume lies to one side of a boundary and the remaining fraction lies to the other side of the boundary. Generally, this construction predicts the lenticular shape of fixed dihedral angle that is often observed for an isotropic particle attached to a flat boundary. A number of oxide particles in Si [49] and Pb particles in Al [50] attached to twin boundaries are examples of anisotropic particle shapes that are similar to those predicted by the construction.

There many observations [22, 47, 49, 50, 51, 52] of boundary particles that produce local variations in boundary orientation, forcing the boundary to "pucker" and reducing the net boundary energy replaced. However, for these cases, there is presently no construction giving the equilibrium shape of the particles and the boundaries to which they are attached.

3.2 Equilibrium Shape for Predictions of Microstructure

The Wulff shape is an equilibrium shape that is useful, for instance, for problems in the isothermal nucleation of a new phase in a supersaturated system. From $\mathcal{W}$, the homogeneous nucleation rate at a constant chemical driving force can be predicted [53, 54]. Likewise, equilibrium shapes derived from $\mathcal{W}$ (*e.g.*, Winterbottom shapes) allow predictions for heterogeneous nucleation at non-deformable substrates [55], at boundaries [56, 57, 58, 59], and at boundary junctions [60].

The Wulff shape is analogous to a phase diagram [14], indicating which orientations of interface are unstable to reorientation [24]. When the unit normal to an interface is not fixed, an unstable orientation will, in the absence of external forces, rotate into a neighboring orientation that appears on $\mathcal{W}$ to reduce its interfacial free energy. When an interface must maintain a fixed average orientation (as for the boundaries considered in this thesis), an unstable interface will break up to form a corrugated shape containing neighboring Wulff shape orientations (of interface) in proportions given by the convex interfacial free energy plot that is defined in Ch. 7 and can be derived from the Wulff shape [24, 25, 61].

A phase diagram shows that only certain phases can coexist at equilibrium.

Similarly, $\mathcal{W}$ shows that edges and corners formed by particular sets of orientations are not expected at equilibrium [14, 25, 42]. The the length of a facet appearing on the Wulff shape can be related to the length of a facet on an observed particle shape to determine the weighted mean curvature of a facet [29]. The weighted mean curvature is useful for thermodynamic models [3] and for kinetic models of shape changes in systems that do [62] and do not [63, 64, 65] conserve volume. Weighted mean curvature is defined in Ch. 5.4.1.

Many properties of polycrystalline and polyphase materials are controlled by boundaries. Boundaries can affect a material's corrosion resistance, electrical conductivity, yield strength and fracture toughness. In addition, they can facilitate the relaxation of lattice strains [37] and decrease the activation energy for phase transitions [66, 67]. Because boundary particles are often used as a means for controlling boundary morphology [68, 69, 70, 71], accurate predictions of equilibrium boundary particle configurations are necessary for grain boundary engineering that derives from the introduction of small particles.

Chapter 4

Particle Shape Constructions

4.1 The Wulff Shape

4.1.1 Definitions

The Wulff shape minimizes the interfacial free energy of a fixed volume in equilibrium with its surroundings at constant T and $\vec{\mu}$ (Ch. 2.3). Definitions regarding $\mathcal{W}$ are introduced here:

1. The $\mathcal{W}$ derived from $\gamma(\hat{\mathbf{n}})$ forms a convex set [25],

$$\mathcal{W} = \{\, \vec{\mathbf{x}} \in \mathbf{R}^3 \mid \vec{\mathbf{x}} \cdot \hat{\mathbf{n}} \;\leq\; \gamma(\hat{\mathbf{n}}) \} \tag{4.1}$$

   where $\hat{\mathbf{n}}$ is taken over all possible orientations on a unit sphere.

2. Orientations, $\hat{\mathbf{n}}$, that appear on $\mathcal{W}$ are *equilibrium orientations* and have relatively low energy and/or are necessary to enclose the fixed volume.
3. $\mathcal{W}$ are invariant to *homotheities*—an equilibrium shape does not change if the length, which is in units of [ENERGY/AREA], is multiplied by the same constant in each dimension [72, page 319].
4. $\mathcal{W}$ that are polygons in $\mathbf{R^2}$ and polyhedra in $\mathbf{R^3}$ are *crystalline shapes* [25].

Figure 4.1 shows four methods of obtaining the Wulff shape from a known $\gamma(\hat{\mathbf{n}})$. These methods are briefly described in Ch. 4.1.2.

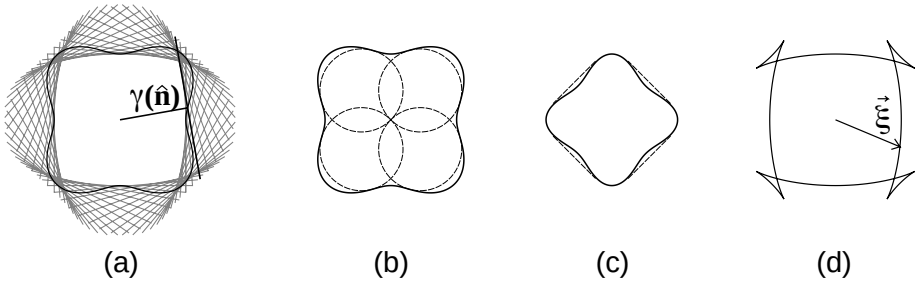

Figure 4.1: Two-dimensional projections of geometric constructions of $\mathcal{W}$, adapted from W.C. Carter: (a) the Wulff construction, giving $\mathcal{W}$ as the inner envelope of perpendicular planes; (b) Herring's method, showing the orientations that appear on $\mathcal{W}$ to fall between tangential points of neighboring spheres that pass through the $\gamma(\hat{\mathbf{n}})$–origin and lie inside the $\gamma(\hat{\mathbf{n}})$–plot; (c) Frank's method, showing $\mathcal{W}$ orientations to fall between planes that are tangential to, but do not extend to the interior of, an inverted $\gamma(\hat{\mathbf{n}})$–plot; and (d) the Cahn-Hoffman capillarity vector, which traces $\mathcal{W}$ as well as the unstable portions that appear where $\vec{\xi}(\hat{\mathbf{n}})$ is multi-valued. Constructions (b)–(d) indicate (1) which orientations are unstable and (2) the orientations (and the proportions of them) that an unstable orientation will dissociate into when the average orientation, $\hat{\mathbf{n}}^{avg}$, is fixed. The constructions *do not* specify the exact shape of such a dissociated $\hat{\mathbf{n}}^{avg}$.

4.1.2 Methods of Construction

The Wulff construction [8], given by example in Fig. 4.1, extracts $\mathcal{W}$ from a polar plot of $\gamma(\hat{\mathbf{n}})$ by drawing, for each orientation $\hat{\mathbf{n}}$, a plane perpendicular to $\hat{\mathbf{n}}$ a distance $\gamma(\hat{\mathbf{n}})$ along $\hat{\mathbf{n}}$ from the origin of the plot (Fig. 4.1(a)). Each such plane eliminates a half-space from $\mathcal{W}$, and the inner envelope of all planes defines the $\mathcal{W}$ for the $\gamma(\hat{\mathbf{n}})$ that is plotted. The Wulff construction has been shown to produce the shape giving a global minimum in interfacial free energy [73, 74] that is unique [75].

The Wulff shape can be obtained through other geometric constructions, such as Herring's method of tangent spheres [24] (Fig. 4.1(b)) and Frank's method of inversion [76] (Fig. 4.1(c)). Herring's method is reconsidered for interfaces that do not bound a fixed volume (*i.e.*, boundaries) in Ch. 7 and in Ch. 10.

This work uses the Cahn-Hoffman capillarity vector, $\vec{\xi}$ [77, 78] (Fig. 4.1(d)),

to describe equilibrium orientations.

Important features of $\vec{\xi}$ include:

1. It is equivalent the gradient of a homogeneous extension of interfacial free energy with respect to the area vector,

$$\vec{\xi} = \vec{\nabla}_{\vec{\mathbf{A}}}(A\gamma(\hat{\mathbf{n}})) = \vec{\nabla}_{\vec{\mathbf{A}}}(\gamma(\vec{\mathbf{A}})) \tag{4.2}$$

   where

$$A\hat{\mathbf{n}} = \vec{\mathbf{A}} = \langle A_1, A_2, A_3 \rangle \qquad \vec{\nabla}_{\vec{\mathbf{A}}} = \langle \tfrac{\partial}{\partial A_1}, \tfrac{\partial}{\partial A_2}, \tfrac{\partial}{\partial A_3} \rangle$$

   and $A\gamma(\hat{\mathbf{n}}) = \gamma(\vec{\mathbf{A}})$ because $\gamma(\hat{\mathbf{n}})$ is homogeneous degree one (HD1) in $\hat{\mathbf{n}}$, meaning that multiplying $\hat{\mathbf{n}}$ by a number, λ, multiplies the entire function by that number raised to the first power, λ^1.
2. It is analogous to the gradient of other intrinsic thermodynamic quantities. For example, it is analogous to the chemical potential, and a common tangent construction applied to unstable orientations predicts corrugated structures [14].
3. It traces $\mathcal{W}$.
4. It recovers the relative free energies of equilibrium orientations, $\gamma(\hat{\mathbf{n}}) = \vec{\xi} \cdot \hat{\mathbf{n}}$
5. Its divergence with respect to $\hat{\mathbf{n}}$ is the weighted mean curvature, // $\vec{\kappa}_\gamma = \vec{\nabla}_{\hat{\mathbf{n}}} \cdot \vec{\xi}$ [29], which is discussed in Ch. 5.4.1.

For a fixed volume attached to a boundary joining two homogeneous phases or grains (*i.e.*, a heterophase boundary or grain boundary), the shape minimizing Eq. (2.2) is modified because two particle interfaces replace a portion of the boundary. The modifications to $\mathcal{W}$ depend on the properties of the replaced boundary. Known modified $\mathcal{W}$ constructions are described in Ch. 4.2.

4.2 Particles Attached to Boundaries: Truncated Wulff Shapes

4.2.1 Winterbottom Construction: Particle to One Side of a Non-Deformable Boundary

The *Winterbottom shape* [9] minimizes the total interfacial free energy for a configuration where a fixed volume (henceforth, a particle) locates to one side of a non-deformable, flat boundary.

The Winterbottom construction was derived [9] to explain observations [44] of faceted noble metal particles on substrates. The utility of the construction is apparent on considering the questions prior to [43, 79, 80] and applications following [45, 48] its development.

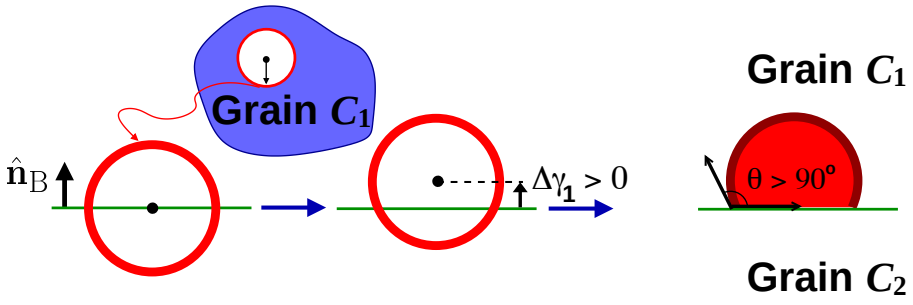

Figure 4.2: The isotropic Winterbottom shape is a spherical cap that results when the origin of the sphere $\mathcal{W}$ in C_1 is displaced from the boundary plane defined by $\hat{\mathbf{n}}_B$ by $\Delta\gamma_1$ along $\hat{\mathbf{n}}_B$. In this case, the boundary energy is relatively small, giving $\Delta\gamma_1 > 0$ and $\theta > 90^\circ$.

Consider an isotropic particle in $\mathbf{R^3}$. When the particle is not attached to a boundary, its equilibrium shape is a sphere [81]. When the particle attaches to a boundary joining C_1 and C_2 to form a Winterbottom shape, the first integral in Eq. (2.2), when applied to all particle interfaces and limited to boundary where changes occur, becomes

$$\int \gamma(\hat{\mathbf{n}})dA = (\gamma_{C_2} - \gamma_{\mathrm{B}})A_{\mathrm{B}} + \gamma_{C_1}A_{C_1} \tag{4.3}$$

for particle volume that locates in C_1. In Eq. (4.3), γ_{C_2} is the free energy density describing the (flat) particle interface that abuts C_2, γ_{B} describes the boundary, A_{B} is the replaced boundary area, and $\gamma_{C_1}A_{C_1}$ describes the total energy of the particle interface that abuts C_1. The Winterbottom shape in this case is a spherical cap characterized by the contact angle, θ, that satisfies Young's equation,

$$\gamma_{\mathrm{B}} = \gamma_{C_2} + \gamma_{C_1}\cos(\theta) \tag{4.4}$$

for a surface tension balance along the boundary-particle triple line in the plane of the boundary. Young's equation is a reduced form of the more general tension balance that considers components normal to the boundary plane and requires that, for three interfaces described by γ_1, γ_2, and γ_3,

$$\frac{\gamma_1}{\sin(\theta_{23})} = \frac{\gamma_2}{\sin(\theta_{31})} = \frac{\gamma_3}{\sin(\theta_{12})} \tag{4.5}$$

where θ_{ij} is the smallest angle between interfaces i and j.

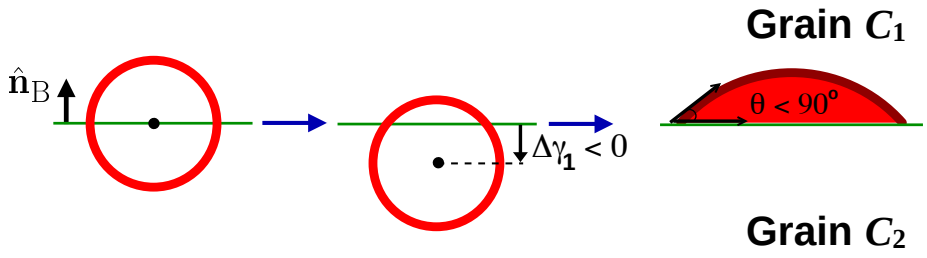

Figure 4.3: The isotropic Winterbottom shape for a particle of the same area (volume in $\mathbf{R^3}$) as in Fig. 4.2 but with $\Delta\gamma_1 < 0$ and $\theta < 90^{\circ}$.

The two-dimensional projections in Fig. 4.2 demonstrate that the spherical cap given by Eqs. (4.3)–(4.5) can be obtained graphically by placing the $\vec{\xi}$–origin of the spherical $\mathcal{W}$ that has a radius of magnitude γ_{C_1} and describes the particle embedded in C_1 (taking the center of the sphere as the Wulff point) on a plane representing the boundary position and displacing the sphere by the difference $\Delta\gamma_1 = (\gamma_{C_2} - \gamma_B)$ along a boundary normal that is oriented from C_2 to C_1. The portion of the sphere that remains to the C_1 side of the boundary after the displacement is a spherical cap with a contact angle of θ—the isotropic Winterbottom shape.

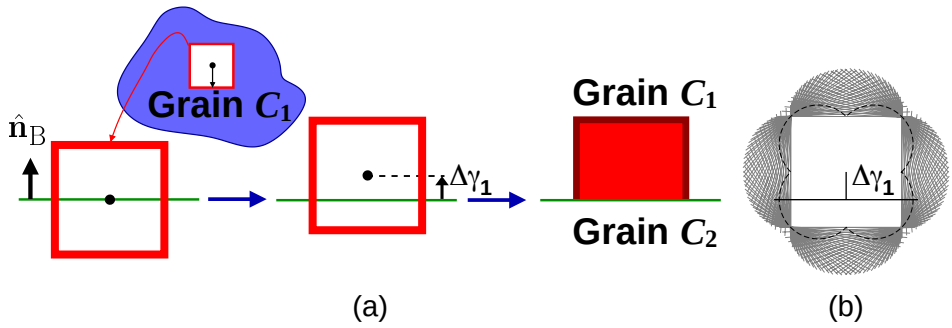

Figure 4.4: The Winterbottom construction is a modification of the Wulff construction, replacing the half-space of orientations that do not appear (due the removal of boundary energy) with an interface that has an effective energy density $\Delta\gamma_1$. The Winterbottom shape can be considered as (a) a truncation of the portion of the shape that lies above the boundary after a translation of $\Delta\gamma_1$ along $\hat{\mathbf{n}}_B$ or (b) the addition (to the Wulff construction) of a plane perpendicular to $\hat{\mathbf{n}}_B$ at a distance $\Delta\gamma_1$ along $-\hat{\mathbf{n}}_B$.

The cap in Fig. 4.2 results for a relatively small boundary free energy ($\Delta\gamma_1 > 0$) and thus has a contact angle of $\theta > 90^\circ$. The particle spreads to replace more boundary energy for the same particle volume as $\Delta\gamma_1$ is reduced. When the boundary energy is sufficiently high that $\Delta\gamma_1 < 0$, as in Fig. 4.3, the cap takes a shape for which $\theta < 90^\circ$.

Figure 4.4(a) shows the Winterbottom construction for an anisotropic shape. Figure 4.4(b) shows that the Winterbottom construction is equivalent to drawing a plane perpendicular to $-\hat{\mathbf{n}}_B$ (when $\hat{\mathbf{n}}_B$ points from C_2 to C_1 and the particle is located in C_1) at a distance of $\Delta\gamma_1$ and eliminating the portion of $\mathcal{W}$ that lies beyond (to the C_2 side of) this plane. The Winterbottom shape is thus a truncated Wulff shape.

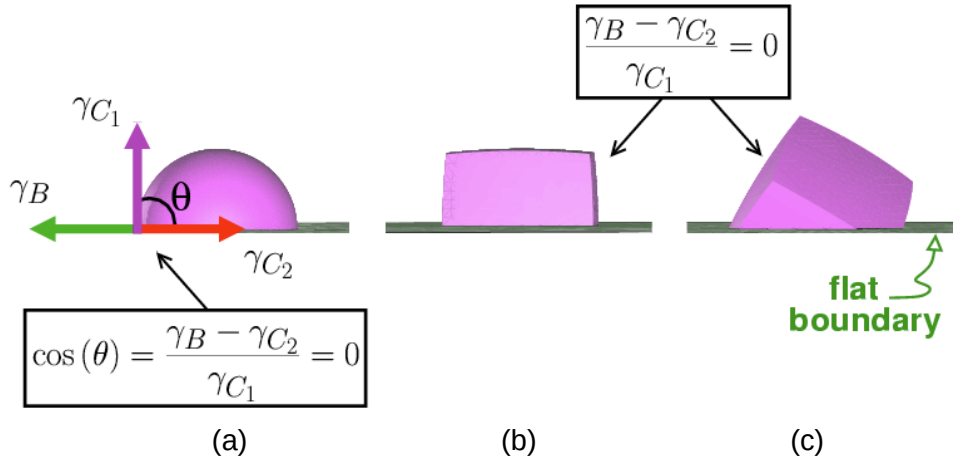

Figure 4.5: Winterbottom shapes of fixed volume for: (a) an isotropic particle, (b) a particle for which the Wulff shape is a cube and the boundary is parallel to a cube facet, and (c) the same cube $\mathcal{W}$ where particle facets are inclined to the boundary. In each case, the relative interfacial free energies give an effective dihedral angle of 90°—*i.e.*, $(\gamma_B - \gamma_{C_2})/\gamma_{C_1} = 1$. Interfaces of the anisotropic shapes are slightly rounded because they result from $\gamma(\hat{\mathbf{n}})$ that have shallow minima producing a range of neighboring stable orientations.

Winterbottom shapes for anisotropic particles can be constructed if the $\mathcal{W}$ describing the particle embedded in C_1 (Fig. 4.4) is known in addition to $\Delta\gamma_1$ and $\hat{\mathbf{n}}_B$. The calculated examples in Fig. 4.5 give complete shapes in $\mathbf{R^3}$ to emphasize that, for the anisotropic case, the orientation of the particle relative to the boundary must also be known—*e.g.*, different Winterbottom shapes, and different changes in the total interfacial energy, occur for cube $\mathcal{W}$ with facets parallel to the boundary and cube $\mathcal{W}$ with facets inclined to the boundary, a result with implications in the nucleation of thin films [43, 55]. The anisotropic particle shapes in the figure have interface with slight curvature. This curvature occurs because the $\gamma(\hat{\mathbf{n}})$ used to describe the shapes have shallow minima as in Fig. 4.1 that produce a small neighborhood of stable orientations.

4.2.2 Summertop Construction: Particle to One Side of Non-Deformable Boundaries

The *Summertop shape* [82] is a modified Winterbottom shape that gives the equilibrium form of a particle located to one side of two or more flat boundaries intersecting along a line (to make an edge) or at a point (corner).

Such shapes were initially considered for orthogonal corners in a study of the growth mechanisms of LiF evaporated on NaCl substrates [43], but the solution appeared later and was extended to general corners [82]. The analysis has since proven useful to problems in sintering [83] and surface lithography [84].

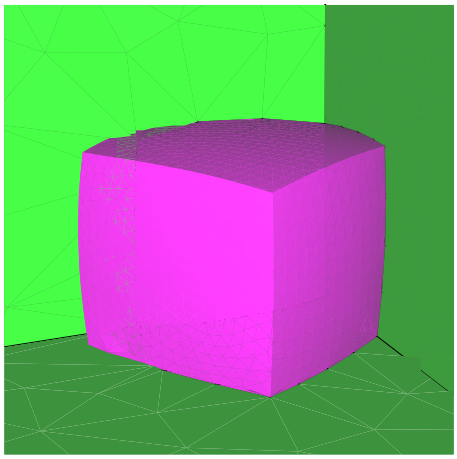

Figure 4.6: The Summertop shape of a cube in a corner defined by orthogonal planes of equal energy density $\gamma_B = 0.6\gamma_{C_1}$, where γ_{C_1} is the energy density of each particle facet.

Like the Winterbottom construction, the Summertop construction discards portions of the Wulff shape. In this case, a half-space is discarded for every substrate (flat boundary) the particle contacts. For example, Fig. 4.6 shows the shape of a particle attached to a corner of three orthogonal boundaries of equal energy. Such a shape might be observed in the valley of a hill-and-valley structure used to describe faceted boundaries. When boundaries have sufficiently large energy, the Summertop shape can be non-convex to allow a particle to increase the total boundary energy replaced [48, 82].

4.2.3 Double Winterbottom Construction: Non-Deformable Boundaries

Generally, when a particle attaches to boundary to eliminate boundary energy, particle volume locates to both sides of the replaced boundary. C.A. Johnson [85] suggested a simple method to determine the equilibrium shapes of particles with volume penetrating through a flat boundary. This suggestion was realized with two-dimensional constructions of single crystal particles attached to flat twin boundaries using Cahn-Hoffman capillarity vector [78]. The construction has since been used to interpret observations of octahedral [49] and truncated octahedral particles [47] at flat twin boundaries as well as the nucleation of lenticular particles at general flat boundaries [86].

The double Winterbottom construction is briefly described here, and a pedagogical example appears in Ch. 5.3.1. Let the boundary join C_1 and C_2, as before. If $\mathcal{W}_1'$ is the Wulff shape of the particle embedded in C_1 and $\mathcal{W}_2'$ is that in C_2, then the equilibrium shape is described by the union of (the portion of $\mathcal{W}_1'$ remaining in C_1 after a displacement of a fraction the boundary energy toward C_2) and (the portion of $\mathcal{W}_2'$ remaining in C_2 after a displacement of the remaining fraction of the boundary energy toward C_1). That is, the equilibrium shape is the union of two Winterbottom-type shapes. This double Winterbottom construction can be extended to boundary junctions that join non-deformable boundaries.

4.2.4 Double Winterbottom Construction: Deformable Boundaries

A double Winterbottom construction that allows the boundary to deform in the vicinity of a boundary particle was developed [56] to consider the nucleation of third-phase particles at isotropic boundaries in $\mathbf{R^2}$. The construction fixed the endpoints of the boundary, giving, for some cases, boundaries forced to curve to meet the $\mathcal{W}$ intersections producing a boundary particle shape.

A non-uniformly curved isotropic boundary in $\mathbf{R^2}$ gives gradients in chemical potential and is therefore an unstable structure. However, numerical calculations of particles attached to deformable isotropic boundaries in $\mathbf{R^3}$ based on the $\mathbf{R^2}$ construction applied to specific cases that give non-uniformly curved boundaries in $\mathbf{R^2}$ [57] indicate the complexity of *equilibrium* configurations in $\mathbf{R^3}$ for particles which are anisotropic.

4.3 Summary

Geometric constructions for the equilibrium shapes of particles embedded within a single phase and particles located to one side of one or more non-deformable boundaries have been developed prior to this thesis. The existing construction [56] in $\mathbf{R^2}$ for particles attached to deformable boundaries typically gives insufficient information regarding an equilibrium configuration in $\mathbf{R^3}$. Because one cannot generally predict changes to boundary shape in $\mathbf{R^3}$ that occur on particle attachment, finding the equilibrium configuration for a boundary particle is generally non-trivial [87], and a study involving boundary particle shape must rely on a numerical method.

Part II

Determination of the Equilibrium Shapes of Particles Attached to Deformable Boundaries

Chapter 5

Compromise in Shape due to Geometric Constraints

5.1 Geometric Description of Interfaces Between Crystalline Phases

A crystalline interface has eight degrees of freedom. Five degrees of freedom are macroscopic: three specify the misorientation between the crystal axes of the grains meeting at the boundary, and two specify the orientation of the unit normal to the boundary [88]. Here, it is assumed that the three microscopic translational degrees of freedom are eliminated by an automatic relaxation of the relative grain positions.

Figure 5.1 illustrates the geometry of a planar boundary separating two grains C_1 and C_2. For this example, the crystal axes of grain C_1 are chosen as the reference axes. Boundary orientation is given by the boundary unit normal defined relative to the reference axes and requires the specification two geometric variables. The boundary orientation in the figure is $\hat{\mathbf{n}}_{\mathrm{B}} = \left\langle 0, \frac{1}{\sqrt{3}}, \frac{2}{\sqrt{3}} \right\rangle$. To simplify the notation for unit normals, common denominators will be eliminated. For example, the boundary orientation in the figure will be referred to as $\hat{\mathbf{n}}_{\mathrm{B}} = \langle 012 \rangle$, and the reader can find $\hat{\mathbf{n}}_{\mathrm{B}}$ with the knowledge that, as a unit vector, $\|\hat{\mathbf{n}}_{\mathrm{B}}\| = 1$.

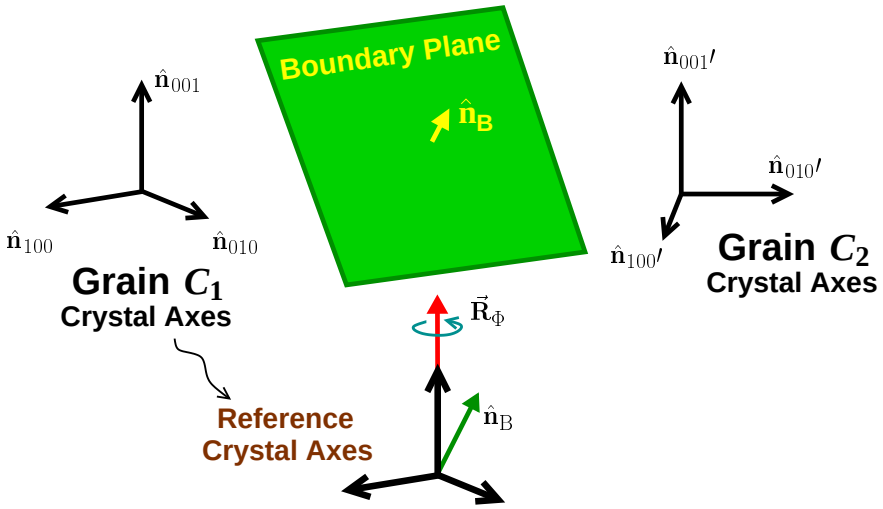

Figure 5.1: Definitions of $\vec{\mathbf{R}}_\Phi$ and $\hat{\mathbf{n}}_B$ for a planar boundary separating two crystals C_1 and C_2. The crystal axes of C_1 are taken as the reference axes.

The crystal axes of grain C_2 are related to the reference axes by a rotation about an axis $\hat{\mathbf{n}}_{001} = \langle 001 \rangle$ (specification of two variables) by an angle of Φ (one variable). The crystallographic misorientation that results is given as a vector that has a magnitude of the misorientation angle and is oriented along the rotation axis. In Fig. 5.1, $\vec{\mathbf{R}}_\Phi = \Phi\langle 001 \rangle$.

Often, several $\vec{\mathbf{R}}_\Phi$ can be used to describe the same crystallographic misorientation. The standard convention is to use the description with the smallest value of Φ. In this work, however, all $\vec{\mathbf{R}}_\Phi$ refer to misorientations about the $\langle 001 \rangle$ direction of C_1.

5.2 Assumptions

The Wulff shape minimizes the interfacial free energy of a fixed volume. As a result, particles with other shape- or size- dependent free energies can have equilibrium shapes different from $\mathcal{W}$. For instance, there are examples that assign energies to edges and corners [89, 90, 91] and determine equilibrium shapes that, for small particle volumes, deviate from the particle's $\mathcal{W}$. Generally, an observed particle shape is dependent on interfacial chemistry [92], disruptions to its internal structure [47, 93], and kinetic limitations to atomic rearrangements [48].

This thesis presents calculations and geometric constructions that neglect the above complications to determine the effects of interfaces that are arranged to form a morphology predicted from the isothermal minimization of interfacial free energy for a fixed (homogeneous) volume attached to a boundary characterized by $\vec{\mathbf{R}}_\Phi$, $\hat{\mathbf{n}}_{\mathrm{B}}^{avg}$, and $\gamma_{\mathrm{B}}(\hat{\mathbf{n}}_{\mathrm{B}})$. The calculations and geometric constructions take the following simplifying assumptions:

1. An interface can be treated as a continuum to avoid the need to deal directly with the its atomic structure.
2. Particles remove/contribute only interfacial energy so that there is no contribution from, *e.g.*, elastic energy.
3. Particles have no internal defects such as grain boundaries that depend on particle shape.
4. Interfacial free energy densities are fixed at a given temperature.

5. There are no limitations to the full relaxation of boundary particle configurations.

5.3 Straight Boundaries in Two Dimensions

5.3.1 Pedagogical Example

The pedagogical examples in this section demonstrate the construction of particle shapes attached to deformable boundaries in $\mathbf{R^2}$. The first example, illustrated in Fig. 5.2, is for an isotropic particle attached to a phase boundary. The second, illustrated in Fig. 5.4, is for an anisotropic particle attached to a grain boundary. The construction differs from that developed previously [56] in that the boundary is allowed to relax to an equilibrium morphology.

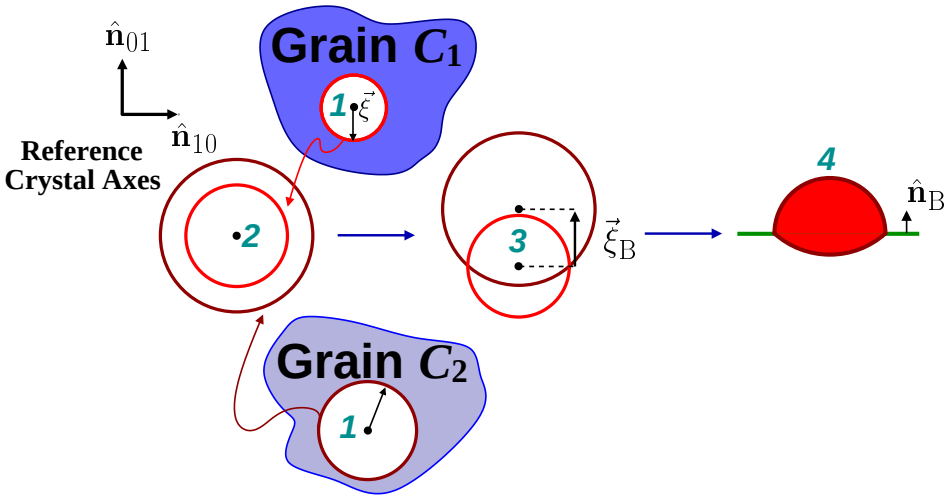

Figure 5.2: The boundary particle construction in $\mathbf{R^2}$ for an isotropic particle attached to a phase boundary. First, $\mathcal{W}_1'$ and $\mathcal{W}_2'$ are defined relative to C_1. Second, $\mathcal{W}_1'$ and $\mathcal{W}_2'$ are both drawn in $\mathbf{R}^\gamma$ from a common reference. Third, $\mathcal{W}_1'$ is displaced toward C_2, and $\mathcal{W}_2'$ is displaced toward C_1. Fourth, the intersection of the displaced shapes (defined here as the union of the displaced halves truncated by the boundary) is the equilibrium shape, and straight boundary line is attached where the two shapes meet.

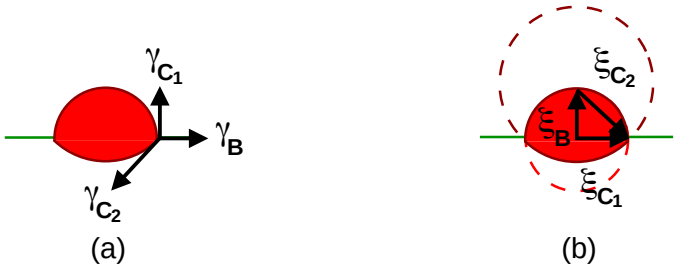

Figure 5.3: (a) The balance of surface tensions is equivalent to (b) a closed $\vec{\xi}$ triangle at intersections of interface.

Consider the phase boundary in Fig. 5.2, and take the crystal axes of grain C_1 as the reference axes. Let the Wulff shape of a particle embedded in C_1 be $\mathcal{W}_1'$ and that in C_2 be $\mathcal{W}_2'$. Although $\mathcal{W}_1'$ and $\mathcal{W}_2'$ have the same *shape*, they are of different size because the free energy density of particle interface is different on each side of the boundary—in the example, $\gamma_{C_2} = 1.5\gamma_{C_1}$.

Each $\mathcal{W}'$ is traced by a set of $\vec{\xi}$–vectors. Here, the origin chosen for the $\vec{\xi}$–vectors tracing a $\mathcal{W}'$ is called the Wulff center of that $\mathcal{W}'$ and marked with a black circle. In Fig. 5.2, the two $\mathcal{W}'$s are circles, and the Wulff centers are taken to coincide with the centers of the of the circles.

The general construction of a boundary particle shape in $\mathbf{R^2}$ involves four steps, which are numbered in Fig. 5.2 and described in the following:

1. Determine the Wulff shapes as they are oriented in grains C_1 and C_2.
2. Translate the Wulff centers of each shape to an arbitrary point in $\mathbf{R}^\gamma$, which is defined as the space taking directions as crystallographic but length as a free energy density.
3. Displace $\mathcal{W}_1'$ and $\mathcal{W}_2'$ from the origin by $\vec{\xi}_\mathrm{B}$, the capillarity vector for the replaced boundary—*i.e.*, for $\hat{\mathbf{n}}_\mathrm{B}$ oriented from C_2 to C_1, move $\mathcal{W}_1'$ along $-\hat{\mathbf{n}}_\mathrm{B}$ and $\mathcal{W}_1'$ along $\hat{\mathbf{n}}_\mathrm{B}$ until the distance between them is $\|\vec{\xi}_\mathrm{B}\|$
4. Attach boundary line of unit normal $\hat{\mathbf{n}}_\mathrm{B}$ to the intersection points of the displaced $\mathcal{W}_1'$ and $\mathcal{W}_2'$.

For particles embedded in $\mathbf{R^2}$, the Wulff shape of the boundary is irrelevant because the boundary is assumed to be infinite in extent (Ch. 5.2). That is, boundary curvature is eliminated as a consequence of equilibrium, meaning that boundaries maintain a fixed $\hat{\mathbf{n}}_\mathrm{B}$ and are therefore described by a single boundary free energy density.

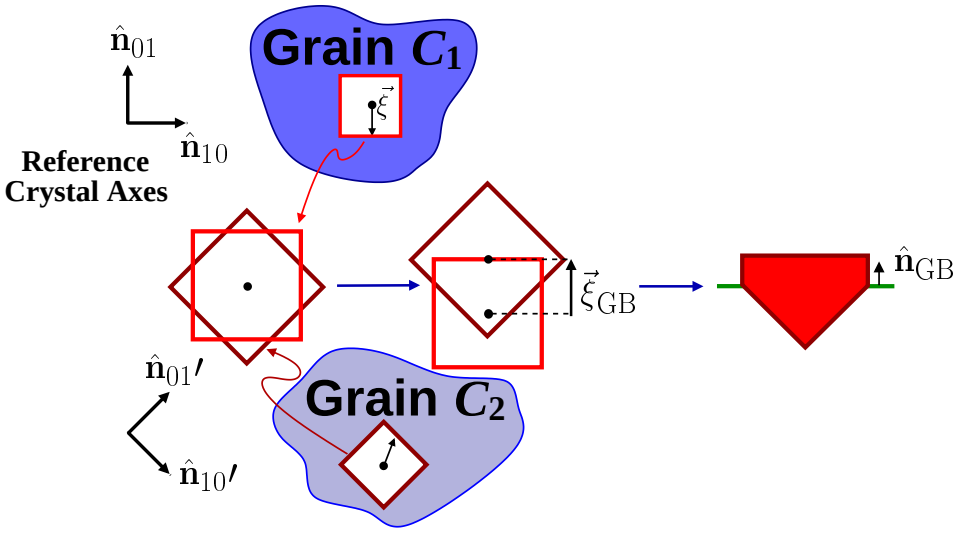

Figure 5.4: The boundary particle construction in $\mathbf{R^2}$ for an anisotropic particle at a grain boundary. The construction is analogous to that in Fig. 5.2. In this case, the $\mathcal{W}$s are squares related by $\vec{\mathbf{R}}_{\Phi} = 45^{\circ}$, and the orientation of the boundary relative to C_1 is $\hat{\mathbf{n}}_{\mathrm{B}} = \langle 01 \rangle$.

For the construction, the boundary and particle interfacial free energy must be taken from a common reference in $\mathbf{R}^{\gamma}$, where units of distance are in [ENERGY/LENGTH] for particles in $\mathbf{R^2}$ and [ENERGY/AREA] for particles in $\mathbf{R^3}$. If $\mathcal{W}_1'$ and $\mathcal{W}_2'$ denote the displaced Wulff shapes, the intersection $\mathcal{W}_1' \cap \mathcal{W}_2'$ defines the boundary particle shape. Note that the term "intersection" is used here to describe the union of the displaced halves truncated by the boundary. When the boundary energy is less than the sum of the two particle interfacial free energies, partial wetting occurs. Otherwise, the case is one of perfect wetting.

The interface of a boundary particle consists of two portions: one that abuts grain C_1 and another that abuts grain C_2. Triple points connect the boundary to the particle where particle interface in grain C_1 meets particle interface in grain C_2. Figure 5.3 shows that a balance of surface tensions at a triple point, which is required for the equilibrium shape of an isotropic particle attached to an isotropic boundary, is equivalent to the closure of the $\vec{\xi}$–triangle defined by the three interfaces that join at the triple point.

Figure 5.4 demonstrates the construction of an anisotropic grain boundary particle. In this case, the Wulff shapes are the same size and shape but have different orientations relative to the reference axes. The two $\mathcal{W}$ are related through $\vec{\mathbf{R}}_{\Phi}$—$\mathcal{W}_1$ and $\mathcal{W}_2$ (and grains C_1 and C_2) have the same orientation when grain C_2 is rotated by $-\vec{\mathbf{R}}_{\Phi}$, which is simply a magnitude (the angle Φ) in $\mathbf{R^2}$. Following the general construction outlined above and demonstrated for the isotropic case, the anisotropic boundary particle shape is given as the intersection between the $\mathcal{W}_1$ and $\mathcal{W}_2$ displaced by $\vec{\xi}_{\mathrm{GB}}$. When multiple triple points are possible, the equilibrium (minimum energy) boundary particle shape is that which gives the smallest volume in $\mathbf{R}^{\gamma}$ because

$$\sqrt[3]{V^{\gamma}} \propto \Delta E$$

where V^{γ} is the $\mathbf{R}^{\gamma}$ volume and ΔE is the change in the total interfacial free energy (Appendix D).

5.3.2 Boundary Particle Shape and Boundary Energy

The relative displacement of the oriented $\mathcal{W}$s meeting at a boundary described by $\vec{\xi}_{\mathrm{B}}$ (step three of the construction in Ch. 5.3.1) accounts for the changes to

particle shape due to the removal of boundary energy per unit length of boundary. This step distributes area along the boundary to balance the (energy reduction on removing a portion of the boundary) with the (energy created on changing particle shape). Figure 5.5 illustrates the dependence of the shape of a boundary particle of fixed area on boundary energy with an isotropic and an anisotropic example.

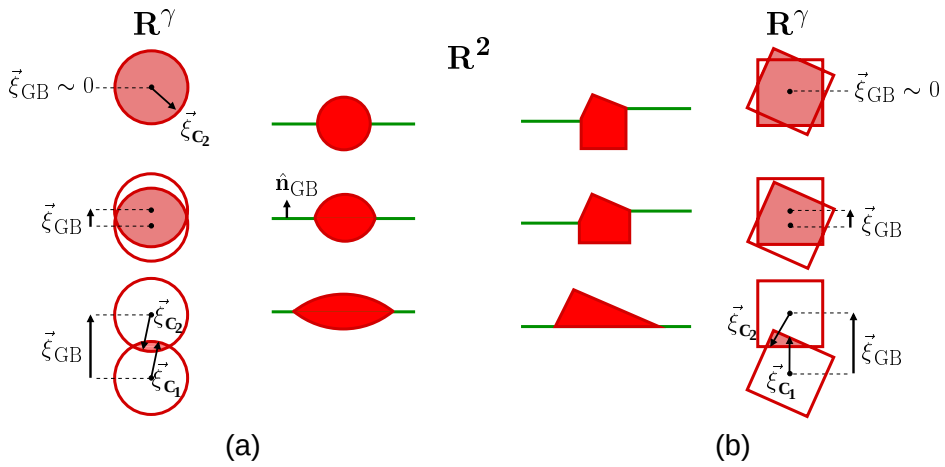

Figure 5.5: The effect of γ_B on boundary particle geometry. In the $\mathbf{R}^\gamma$ columns, $\mathcal{W}_1' \cap \mathcal{W}_2'$ is shaded and similar to the boundary particle shapes of constant area in $\mathbf{R}^2$. As γ_B is increased: (a) an isotropic boundary particle becomes and increasingly flat lens, and (b) an anisotropic boundary particle can pass through sharp transitions in shape when an edge is eliminated and retain the same shape for relative boundary energies above some threshold—in the large boundary energy (bottom) example of (b), it is not possible to determine the relative boundary energy from the construction.

For a fixed $\hat{\mathbf{n}}_B$ and $\vec{\mathbf{R}}_\Phi$, boundary energy controls the size of the $\mathcal{W}$ intersection in $\mathbf{R}^\gamma$. Larger boundary energies reduce $\mathcal{W}_1' \cap \mathcal{W}_2'$ because more energy is available to create particle interface per unit volume of particle. When $\mathcal{W}_1$ and $\mathcal{W}_2$ are isotropic (Fig. 5.5(a)), the equilibrium shape changes from a circle in the limit of zero boundary energy to a lens of vanishing thickness as γ_{GB} approaches the sum of the interfacial free energy densities describing each $\mathcal{W}$. Thus, the equilibrium shape of an isotropic boundary particle indicates the magnitude of γ_B relative to the particle interfacial free energy densities in C_1 and C_2.

In contrast, it is not always possible to determine the relative boundary energy from observations of an anisotropic particle shape. While the dihedral angle of the isotropic particle in Fig. 5.5(a) approaches zero as boundary energy is increased, the intersections of square $\mathcal{W}$ shown in Figs. 5.4 and 5.5(b) give particle shapes that change with increasing γ_B for $\gamma_B < \gamma_B^{\text{threshold}}$. The threshold, $\gamma_B^{\text{threshold}}$, is defined as the lower bound of γ_B producing a constant shape—*i.e.*, for $\gamma_B > \gamma_B^{\text{threshold}}$, the shape does not change as $\mathcal{W}_1' \cap \mathcal{W}_2'$ is reduced. Consequently, the condition for perfect wetting, which occurs when the particle completely replaces the boundary with two new interfaces, does not generally coincide with a limiting shape of zero dihedral angle.

The $\mathbf{R^2}$ construction, illustrated in Fig. 5.4 and 5.5(b) for anisotropic particles, allows the shape of the boundary to relax. The boundaries in Fig. 5.5, for instance, are everywhere straight. Chapters 6.2–6.4 implement this construction numerically for particles attached to general boundaries embedded in $\mathbf{R^3}$.

5.4 Ruffled Boundaries in Three Dimensions

A boundary particle in $\mathbf{R^2}$ divides a boundary into independent segments. Each segment attaches to the particle at a triple point. Generally, the requirements of particle shape result in non-colinear boundaries at equilibrium (Fig. 5.5(b)).

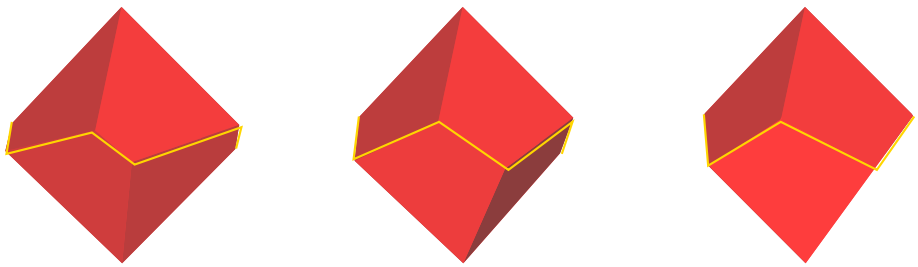

Figure 5.6: The intersection, $\mathcal{W}_1' \cap \mathcal{W}_2'$, between two similar octahedral Wulff shapes where $\mathcal{W}_2'$ is misoriented from $\mathcal{W}_1'$ about the $\langle 001 \rangle$ direction of C_1 by: (a) 15°, (b) 30°, and (c) 45°. The boundary must attach to complex intersection line, which is highlighted in the figure.

In $\mathbf{R^3}$, the boundary is contiguous around an attached particle, and it is not always possible for the boundary to be everywhere flat at equilibrium. Cylinders with non-circular curved cross-sections and prisms are physical examples of objects that produce non-planar boundaries—the cross-sections of such objects have been observed to twist liquid menisci that joined to them [94]. Anisotropic particles formed by the abutment of $\mathcal{W}_1'$ to $\mathcal{W}_2'$ can likewise require a deformable boundary to contort around the particle. For example, Fig. 5.6 shows the triple line that a boundary must attach to for particles with shapes formed by two displaced octahedral $\mathcal{W}'$. Equilibrium (for isotropic boundaries) is satisfied when the attached boundary has a constant mean curvature of zero.

A distorted, or "ruffled", boundary of average unit normal $\hat{\mathbf{n}}_{\mathrm{B}}^{avg}$ will have more area than its projection onto a plane defined by $\hat{\mathbf{n}}_{\mathrm{B}}^{avg}$. For boundary particle stability, the energy created by ruffling must be less than or equal to that removed by the attached particle. Because an anisotropic boundary particle typically creates, as well as removes, boundary, the displacement of particle Wulff shapes along $\hat{\mathbf{n}}_{\mathrm{B}}^{avg}$ (step three in Ch. 5.3.1) is typically less than the magnitude of the boundary free energy because the displacement must account for any additional boundary energy created.

The shapes of the deformable boundary and the boundary particle are interdependent. The displacement in the construction giving an equilibrium configuration relies on a minimization of the the total interfacial free energy. Because one does not generally know the amount of boundary energy created when a particle attaches to a boundary, one does not generally know the equilibrium displacement *a priori*. Consequently, there is no known geometric construction giving an equilibrium boundary particle configuration in $\mathbf{R^3}$. The absence of a known solution was recently recognized in a study [87] using statistical mechanics for particles in four-phase systems.

5.4.1 Calculated Examples

General Case of Ruffled Boundaries

Calculations in this thesis minimize the total interfacial free energy for a fixed volume of particle attached to a boundary in a system of constant T, p, and $\vec{\mu}$.

Typical results show that, under conditions of partial wetting, anisotropic boundary particles produce ruffles in planar boundaries. All calculations take the crystal axes of the grain or phase labeled C_1 as the reference axes.

Figure 5.7 shows results of two calculations yielding ruffled boundaries and one yielding a flat boundary. The flat boundary shown in Fig. 5.7(c) is discussed in Ch. 5.4.1. The result in Fig. 5.7(a) incorporates a pure 45° twist grain boundary, where $\vec{\mathbf{R}}_\Phi = 45^\circ\langle 001\rangle$ and $\hat{\mathbf{n}}_{\mathrm{GB}}^{avg} = \langle 001\rangle$. The Wulff shape of the particle is an octahedron described by an interfacial free energy density of γ_{111}, and the free energy of the isotropic grain boundary is less than that of the particle facets, $\gamma_{\mathrm{GB}} = 0.75\gamma_{111}$. (Throughout this thesis, the general notation γ_{hkl} describes interface of orientation (hkl) reported relative to the local embedding grain.) Pure twist boundary configurations are discussed further in Ch. 11.2.1.

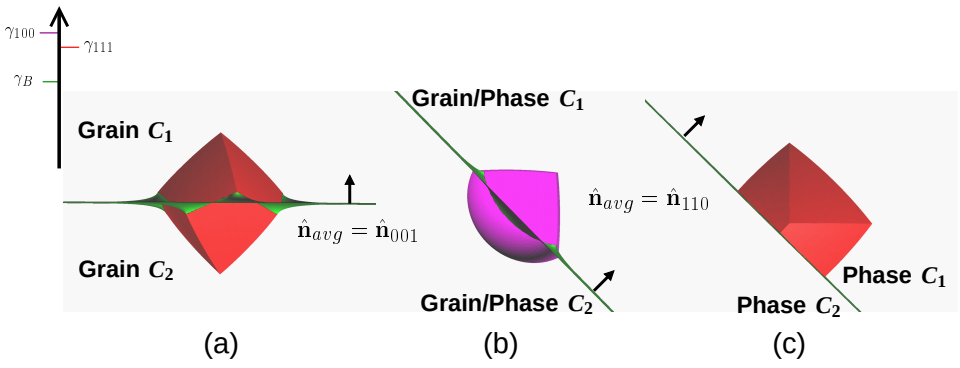

Figure 5.7: Numerical results for boundary particles attached to an isotropic boundary of energy γ_{B} in $\mathbf{R}^3$: (a) a particle for which $\mathcal{W}$ is an octahedron attached to a pure 45° twist grain boundary, where $\gamma_{\mathrm{B}} = 0.75\gamma_{111}$, and γ_{111} describes the interfacial free energy of the particle facets; (b) a particle for which $\mathcal{W}$ is a cube in C_1 and a sphere in C_2, where $1.15\gamma_{\mathrm{B}} = 0.75\gamma_{100}$ and $\gamma_{\mathrm{B}} = 0.5\gamma$, with γ_{100} and γ describing the interfacial free energy densities of the $\{100\}$ and $\{111\}$ particle orientations, respectively; (c) a particle attached to a phase boundary for which $\mathcal{W}_1$ is an octahedron and $\mathcal{W}_2$ is a cube, with $1.15\gamma_{\mathrm{B}} = 0.75\gamma_{100}$ and $\gamma_{100}/\gamma_{111} = 1.15$. Boundary ruffling is apparent in (a) and (b) and depends on the boundary particle shape as well as the relative boundary free energy density. The boundary in (c) remains flat.

Figure 5.7(b) is the result of a calculation for a particle where $\mathcal{W}_1'$ is a cube and $\mathcal{W}_2'$ is a sphere. This thesis does not report $\vec{\mathbf{R}}_\Phi$ when particle interfacial free energy is isotropic in one grain and γ_B is isotropic in $\hat{\mathbf{n}}_B$ and $\vec{\mathbf{R}}_\Phi$. The boundary normal in Fig. 5.7(b) is $\hat{\mathbf{n}}_B = \langle 110 \rangle$, $1.15\gamma_{GB} = 0.75\gamma_{100}$, and $\gamma_{GB} = 0.5\gamma$, where γ_{100} and γ are the free energy densities of the equilibrium (cube) particle interface in C_1 and the isotropic (spherical cap) interface C_2, respectively.

The configuration in Fig. 5.7(b) could represent a particle attached to a phase *or* grain boundary: the Wulff shape of a particle (or its volume in $\mathbf{R}^\gamma$) may differ in different phases; on the other hand, single crystal grain boundary particles are frequently observed to form facets in one grain but an isotropic cap in the other [10]. The Wulff shape is a function of the misorientation between the crystal axes of a crystalline particle and the crystal axes of an embedding grain. If possible, a crystalline particle will align to form the $\mathcal{W}$ that, relative to the $\mathcal{W}$ forming at other particle-grain misorientations, produces the least interfacial free energy. Generally, a single crystalline grain boundary particle can align to form this minimal $\mathcal{W}$ in one grain only, leaving the interface in the second grain to form a portion of a $\mathcal{W}$ dependent on the particle-grain misorientation in that grain. Experimentally, this second $\mathcal{W}$ is often found to be approximately spherical.

Special Case of a Flat Boundary

Figure 5.7(c) shows the equilibrium configuration of a phase boundary particle. For this case, $\mathcal{W}_1'$ is an octahedron described by facets of γ_{111}, and $\mathcal{W}_2'$ is a cube described by facets of γ_{100}, where $\gamma_{100}/\gamma_{111} = 1.15$, and $\gamma_B = 0.75\gamma_{111}$, giving the same interfacial free energy relationship as in Figs. 5.7(a)–(b). In Fig. 5.7(c), the boundary orientation is $\hat{\mathbf{n}}_B = \langle 110 \rangle$, and $\vec{\mathbf{R}}_\Phi = 45^\circ\langle 001 \rangle$.

Fig. 5.7(c) is an example of an anisotropic particle shape that does not ruffle an isotropic boundary. In this case, one face of $\mathcal{W}_2'$ is parallel to the boundary, and because the interfacial free energy densities describing $\mathcal{W}_2'$ orientations are larger than those describing $\mathcal{W}_1'$ orientations (*i.e.*, $\gamma_{100} > \gamma_{111}$), the particle reduces energy by creating only one orientation of $\mathcal{W}_2'$ and keeping the boundary flat.

Conditions for Equilibrium

Figure 5.7 shows approximations to equilibrium. The boundaries have a constant mean curvature (κ) of approximately zero, meaning that displacing any element of boundary normal to itself to sweep out a volume δV gives no change in area. That is, there is no driving force for boundary motion because $\kappa = \delta A/\delta V$ is zero. Likewise, the boundary particles have constant weighted mean curvatures, meaning that displacing a particle facet normal to itself gives a change in interfacial free energy that is independent of which facet is displaced. There is, therefore, no driving force to change shape because $\kappa_\gamma = \delta(\int \gamma dA)/\delta V$ is a constant for each particle facet [29].

Because the boundaries in Figs. 5.7(a) and (b) are ruffled minimal ($\kappa = 0$) surfaces and particles contain a limited number of facets, each having a fixed orientation, particle facet-boundary dihedral angles vary with position. This result supports that of King [95], which shows that, at equilibrium, an isotropic interface can join to an anisotropic interface over a range of dihedral angles.

Chapter 6

Methods of Calculation

6.1 The Isotropic-Anisotropic Continuum: A Numerical Trick

It is difficult to calculate equilibrium shapes of fixed volume described by anisotropic interfacial free energies because interface may locally reorient to reduce interfacial free energy and, in this way, produce shapes that are metastable because they are non-convex. For example, consider the metastable shapes shown in Fig. 6.1. In each case, non-convex features—steps and kinks—are apparent.

Each shape in Fig. 6.1 was calculated by minimizing interfacial free energy for a fixed volume. Figure 6.1(a) was calculated by applying an interfacial free energy density with equivalent minima in $\{111\}$ orientations to a cube, which is a shape that is often used as input to an energy minimization because it is simple to generate. Figure 6.1(b) was calculated by applying the same $\gamma(\hat{\mathbf{n}})$ to a sphere, which can be calculated from a given input shape by minimizing area for the volume. Figure 6.1(c) was calculated by applying the same $\gamma(\hat{\mathbf{n}})$ to an isotropic lens attached to a 15° twist boundary.

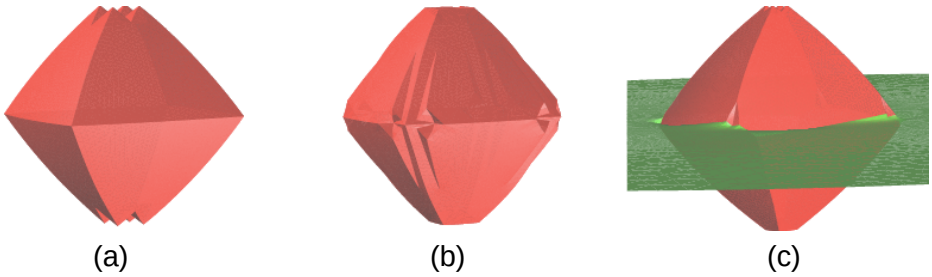

Figure 6.1: Examples of metastable shapes that result when anisotropy is applied directly to a starting configuration. Shapes generated by the application of an interfacial free energy density $\gamma(\hat{\mathbf{n}})$ with equivalent minima in $\{111\}$ orientations to (a) a cube, (b) a sphere, and (c) an isotropic lens attached to a 15° twist boundary.

To avoid metastable equilibria, anisotropy was gradually introduced into a boundary particle configuration. That is, a continuous set of interfacial free energy functions parameterized by the depth of specified minima was applied to particle interface. This numerical trick allowed the particle to gradually increase the area of those orientations appearing on the final anisotropic shape and thereby avoid forming non-convexities.

An example using the trick is given in Fig. 6.3 for the calculation of an octahedron from the $\gamma(\hat{\mathbf{n}})$ that produced the metastable shapes in Fig. 6.1. Figure 6.3 shows the shape of the particle for different depths, $\Delta\gamma_{B-P}$, of the interfacial free energy minima, where $\Delta\gamma_{B-P} = \gamma(\mathcal{W}^{\text{sphere}}) - \gamma_{111}$ describes minima of interfacial free energy density of γ_{111} produced from an isotropic reference density of $\gamma(\mathcal{W}^{\text{sphere}})$.

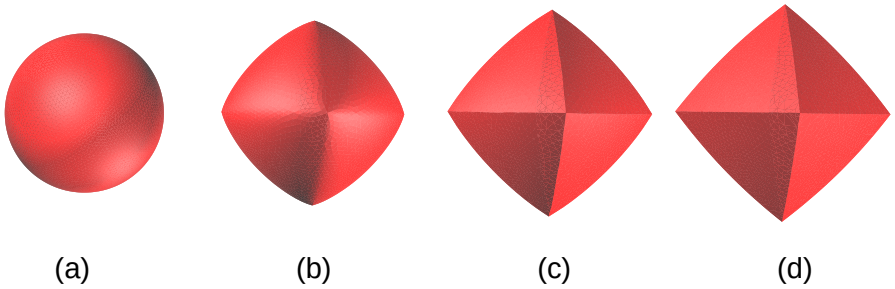

Figure 6.2: A continuous set of $\gamma(\hat{\mathbf{n}})$ that gradually increased the depth of minima in $\{111\}$ orientations was applied to create an octahedron. The minima are of (a) $\Delta\gamma_{B-P} = 0$, (b) $\Delta\gamma_{B-P} = 0.2\gamma(\mathcal{W}^{\text{sphere}})$, (c) $\Delta\gamma_{B-P} = 0.47\gamma(\mathcal{W}^{\text{sphere}})$, and (d) $\Delta\gamma_{B-P} = 0.33\gamma(\mathcal{W}^{\text{sphere}})$.

The set of interfacial free energy functions applied to particle interface parameterize a continuous family of shapes connecting an isotropic $\mathcal{W}$ to an anisotropic one. The symmetric difference between two shapes,

$$\mathcal{W}(\alpha_i) \,\Delta\, \mathcal{W}(\alpha_{i-1}) \tag{6.1}$$

is a method of measuring how similar they are. Equation (6.1) is the union of the portion of $\mathcal{W}(\alpha_i)$ that lies outside of $\mathcal{W}(\alpha_{i-1})$ with the portion of $\mathcal{W}(\alpha_{i-1})$ that lies outside of $\mathcal{W}(\alpha_i)$. It is equivalent to evaluating the distance between two surfaces in a volume integral,

$$\mathcal{W}(\alpha_i) \,\Delta\, \mathcal{W}(\alpha_1) = \iint \sqrt{\left(f(\hat{\mathbf{n}}, \alpha_i) - f(\hat{\mathbf{n}}, \alpha_{i-1})\right)^2}\, dA \tag{6.2}$$

where $f(\hat{\mathbf{n}}, \alpha)$ is the equation of the surface of $\mathcal{W}(\alpha)$, dA is a differential of surface area, and the integral is taken over the surfaces of the two shapes. In Eqs. (6.1)–(6.2), α_i and α_{i-1} are successive values of α, which was used to control $\Delta\gamma_{\mathrm{B-P}}$ during a calculation.

The set represented by Eq. (6.1) decreases as the shapes converge and gives a null set when the shapes are identical [96]. For calculations approximating continuum linking an isotropic solution to a faceted one, decrements in α (increments to the depth of a minimum) were reduced at least three times during a given minimization to visibly reduce the symmetric difference between calculated shapes.

The numerical trick introduced above has been applied elsewhere [89] to produce faceted equilibria, and it was used for all $\mathbf{R^3}$ boundary particle calculations in this thesis. A description of the method applying a formulation for $\gamma(\hat{\mathbf{n}})$ that produces $\mathcal{W}$ with cubic symmetry is given in Ch. 6.3.2. Results for $\mathcal{W}$ of general symmetry, presented in Ch. 7, differ from the description for cubic shapes only in the $\gamma(\hat{\mathbf{n}})$ that is applied.

6.2 The *Surface Evolver* Background

The *Surface Evolver* [97], or *Evolver*, is a program that, among other things, numerically finds the energy-minimizing shapes of surfaces under various con-

straints. A tool for problems involving material interfaces [98], *Evolver* is used in this thesis to calculate the equilibrium configurations of anisotropic particles of fixed volume attached to deformable boundaries in $\mathbf{R^3}$, *e.g.*, the results in Fig. 5.7.

Evolver represents a surface as a finite set of points (vertices) connected with edges to form flat triangular elements. Surfaces are modeled as mathematically sharp entities, and a discretized surface approximates a continuum as the number of vertices is increased. The default surface energy density is isotropic and equal to unity, meaning that the energy of each element is equivalent to its area. Calculations as in this study necessitate distinct methods for applying anisotropic interfacial free energies.

As outlined in [97], *Evolver* triangulates a user-defined approximation to the geometry of interest. Any element of the triangular mesh can be refined during an "evolution". An evolution can be deterministic—*e.g.*, using the gradient descent method for energy minimization, the equilibrium form of a surface is determined by displacing each vertex from its *current* position by a vector proportional to the force (negative of the gradient in total energy) at the vertex position. Vertices subject to particular constraints are displaced while attempting to satisfy those constraints. For example, the calculations in this work are for surfaces embedded in $\mathbf{R^3}$ subject to the constraints of fixed crystallographic misorientation, boundary orientation, and particle volume. In practice, this means that the configurations have degrees of freedom equal to (the total number of vertices multiplied by three orthogonal translations) less (the number of vertices terminating the boundary far from the particle) less (one for the volume constraint).

Evolver has a number of advanced features and routines that are useful for particular problems. Chapter 6.3 shows how crystallography is introduced for this work by building on the basic description of *Evolver* presented here.

6.3 Using Energetic Constraints to Specify Geometry

6.3.1 Boundaries

Boundaries Maintain a Fixed $\hat{\mathbf{n}}_{\mathrm{B}}^{avg}$

To determine equilibrium particle shapes attached to boundaries that can locally

reorient, boundaries are constrained to maintain a prescribed average unit normal, $\hat{\mathbf{n}}_{\mathrm{B}}^{avg}$. The implementation of this constraint is equivalent to the following: the boundary particle is placed inside a cylinder that has an axis parallel to $\hat{\mathbf{n}}_{\mathrm{B}}^{avg}$, and the boundary attaches to the cylinder walls with a 90° contact angle. There is a global constraint preventing changes to $\hat{\mathbf{n}}_{\mathrm{B}}^{avg}$ but not displacements along $\hat{\mathbf{n}}_{\mathrm{B}}^{avg}$.

Boundaries Appear Infinite in Extent

In this work, "infinite" boundaries are large enough that particle-induced ruffling decays before reaching the boundary perimeter. Because boundaries are isotropic, they are minimal surfaces at equilibrium, meaning that the mean curvature is zero at very point on the boundary. For this reason, the Gaussian curvature, $\mathcal{K}$, which quantifies the "spread" of unit normal directions per unit area [72, page 215], is used as a local measure of boundary ruffling.

Appendix A demonstrates how $\mathcal{K}$ was determined at a boundary point. Calculations of $\mathcal{K}$ show that boundary ruffling is largest in the immediate vicinity of the particle—particularly at points where particle edges meet the triple junction—and ruffling diminishes with radial distance (along the average boundary plane) from the center of the particle.

Distance from the particle to a point on the boundary where $\mathcal{K} \approx 0$ is found to be dependent on particle shape, boundary orientation, and the value of γ_{B} relative to the particle interfacial free energy densities [99]. The decay distance, Λ, increases with both the volume of the particle and $1/\gamma_{\mathrm{B}}$ according to

$$\Lambda \propto \left(\frac{\Delta E}{\gamma_{\mathrm{GB}}} \right)^{\frac{1}{2}}$$

where ΔE is the change in interfacial free energy that occurs when a volume, V, of boundary particle is formed. In all cases considered, $\mathcal{K} \approx 0$ at $\Lambda < 3V^{1/3}$, and the cylinder radius employed in the calculations, $r = 8V^{1/3}$, was more than adequate to model "infinite" boundaries.

6.3.2 Boundary Particles

Boundary Particles Enclose a Fixed Volume

If the volume of a particle is not fixed during an energy minimization under conditions of partial wetting, the particle interface would shrink out of existence to leave a system that contains only the boundary. Eq. (2.2) is minimized when calculating a particle shape of fixed volume, and *Evolver* ascribes a pressure—the Lagrange multiplier for the volume constraint—to the particle.

In the calculations, abutting grains exert no pressure along a boundary. Thus, the pressure of the boundary particle is equivalent to the change in pressure across particle interface. This change in pressure balances the surface divergence of the $\vec{\xi}$ describing the particle [78], a quantity defined as the weighted mean curvature [3, 29] in Ch. 4.1.2 and 5.4.1.

Anisotropic Interfacial Free Energies Maintain a Fixed $\vec{\mathbf{R}}_\Phi$

Many material systems show second-phase particles to topotactically align in an embedding grain [100]. This observation, discussed further in Ch. 8, is applied here: boundary particle facets are used to specify the orientation of each crystal abutting at a boundary—*i.e.*, $\vec{\mathbf{R}}_\Phi$. For instance, a particle completely defined by $\{111\}$ facets will have $\{111\}$ facets in C_1 parallel to the $\{111\}$ planes of C_1 and $\{111\}$ facets in C_2 parallel to the $\{111\}$ planes of C_2. The misorientation between the $\{111\}$ facets in C_1 and those in C_2 is $\vec{\mathbf{R}}_\Phi$. Consequently, in this work $\vec{\mathbf{R}}_\Phi$ is meaningless for boundary particles that are isotropic in one grain and attached to boundaries that are isotropic in misorientation (Ch. 5.4).

By default, *Evolver* gives each element M of a discretized interface an energy of $\|\vec{\mathbf{A}}_M\|\gamma$, where $\|\vec{\mathbf{A}}_M\|$ is the area vector of element M and γ is the unit interface tension. The components of the area vector are $\vec{\mathbf{A}} = \langle A_1, A_2, A_3\rangle = \|\vec{\mathbf{A}}\|\langle n_1, n_2, n_3\rangle$. Anisotropic particles of fixed volume can be calculated by defining an orientation-dependent $\gamma(\hat{\mathbf{n}})$ to describe each element of particle interface. The total interfacial free energy for a configuration is a summation over all elements, $\sum_M \|\vec{\mathbf{A}}_M\|\gamma(\hat{\mathbf{n}}_M) = \sum_M \gamma(\vec{\mathbf{A}}_M)$.

The following HD1 function was used in *Evolver* to form shapes of cubic

symmetry,

$$\gamma(\hat{\mathbf{n}}) = \frac{(w_S S(\hat{\mathbf{n}}) + w_P P(\hat{\mathbf{n}}))}{(n_1^2 + n_2^2 + n_3^2)^{3/2}} \gamma Q \tag{6.3}$$

where

$$S(\hat{\mathbf{n}}) = n_1^4 + n_2^4 + n_3^4 \tag{6.4}$$

$$P(\hat{\mathbf{n}}) = (n_1 n_2)^2 + (n_3 n_2)^2 + (n_3 n_1)^2 \tag{6.5}$$

where w_S, w_P, and Q are each non-negative. Equation (6.4) is a fourth order polynomial that is applied in this thesis to create interfacial free energy minima in $\{100\}$ and $\{111\}$ orientations. As described below, the anisotropy factor, α, is used with variables w_S, w_P, and Q to create anisotropic particle shapes.

Equation (6.3) allows the depth of γ–minima in $\{100\}$ orientations to be specified independently from those in $\{111\}$ orientations. Specification of γ–minima gives a result with cubic symmetry—*i.e.*, the $(\bar{1}00)$ orientation will have the same interfacial free energy density as that of (001).

The anisotropy factor, α, is used to control the relative depth of $\gamma(\hat{\mathbf{n}})$–minima and thus parameterize the continuum of $\gamma(\hat{\mathbf{n}})$ connecting an isotropic $\mathcal{W}$ to the desired anisotropic result. The anisotropy factor takes values of $0 \leq \alpha \leq 1$, producing nearly crystalline shapes with facet free energies of $\gamma Q/3$ for $\alpha = 0$. All shapes calculated in this thesis are *nearly* crystalline because α has been limited to produce $\gamma(\hat{\mathbf{n}})$ with minima that are shallow to give a finite range of stable orientations. To facilitate ensuing discussions, nearly crystalline shapes will be called faceted.

Examples of faceted shapes are shown in Figs. 6.2(d) and 6.4(d). For a fixed volume described by Eq. (6.3), a sphere minimizes interfacial free energy when $2w_S = w_P$, a cube is the minimum energy shape when $w_S = 1/3$ and $w_S = 2$, and an octahedron is the minimum energy shape when $w_S = 1$ and $w_S = 0$. The relationship between w_S, w_P, equilibrium shape, and the $\gamma(\hat{\mathbf{n}})$ of orientations appearing on the equilibrium shape is summarized in Table 6.3.2.

Calculations using Eq. 6.3 give minima in $\{100\}$ and $\{111\}$ orientations. Although calculations take the C_1 crystal axes as a reference, $\{100\}$ and $\{111\}$ refer to local orientations (as mentioned above) so that,*e.g.*, a discussion of $\{100\}$ par-

		$\alpha = 1$		$\alpha = 0$	
w_S	w_P	**shape**	**energy density**	**shape**	**energy density**
2	1	sphere	$\gamma\mathcal{Q}$	sphere	$\gamma\mathcal{Q}$
$\frac{1+2\alpha}{3}$	2	sphere	$\gamma\mathcal{Q}$	cube	$\frac{\gamma\mathcal{Q}}{3}$
1	2α	sphere	$\gamma\mathcal{Q}$	octahedron	$\frac{\gamma\mathcal{Q}}{3}$

Table 6.1: Relationship between w_S, w_P, equilibrium shape, and the $\gamma(\hat{\mathbf{n}})$ of orientations that appear on the equilibrium shape with α, as described by Eq. (6.3). Variables $\mathcal{Q}$ are used to define relative free energies of appearing orientations—for instance, a boundary particle shape that is a portion of a cube in C_1 and a portion of an octahedron in C_2 could have $\mathcal{Q} = 1.15$ in C_1 and $\mathcal{Q} = 1$ in C_2 to give $\gamma_{100}/\gamma_{111} = 1.15$, where γ_{100} describes the free energy of cube facets, and γ_{111} describes the free energy of octahedral facets. Here, γ refers to *Evolver*'s default surface tension.

ticle facets refers both to those abutting C_1 that are parallel to $\{100\}$ planes of C_1 *and* facets abutting C_2 that are parallel to $\{100\}$ planes of C_2.

To illustrate the application of Eq. (6.3) for a shape containing both $\{100\}$ and $\{111\}$ orientations, consider a phase boundary particle formed by portions of two different $\mathcal{W}$. Let the $\mathcal{W}$ in phase C_1 be a cube described by an interface of energy density γ_{100}, and the $\mathcal{W}$ in phase C_2 be an octahedron described by an interface of energy density γ_{111}. To apply relative the interfacial free energies obtained from observations of Pb single crystals in Al [10], again let $\gamma_{100} = 1.15\gamma_{111}$.

The energy-minimizing particle shape for this example is obtained by applying Eq. (6.3) to each element of particle interface: Values of w_S and w_P producing a cube at $\alpha = 0$ (Table 6.3.2) are used with $\mathcal{Q} = 1.15/(1 + 0.15\alpha)$ for interface in C_1, and values of w_S and w_P producing a octahedron at $\alpha = 0$ are used with $\mathcal{Q} = 1$ for interface in C_2. For $\alpha = 0$, these values give minima of $\gamma(\vec{\mathbf{A}}_M) = 1.15\gamma\|\vec{\mathbf{A}}_M\|/3$ for each element of interface with $\hat{\mathbf{n}} = \langle 100\rangle = \hat{\mathbf{n}}_{100}$ in phase C_1, and $\gamma(\vec{\mathbf{A}}_M) = \gamma\|\vec{\mathbf{A}}_M\|/3$ for each element with $\hat{\mathbf{n}} = \langle 111\rangle = \hat{\mathbf{n}}_{111}$ in phase C_2. The unit normal notation is defined in Ch. 5.1.

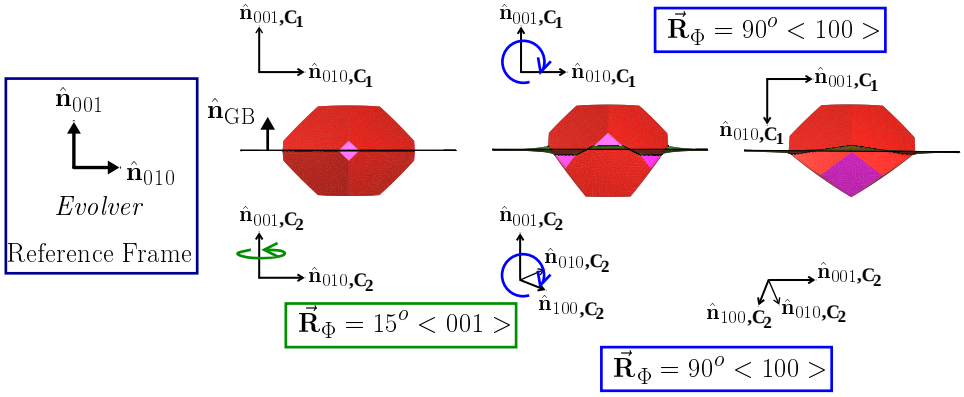

Figure 6.3: To determine the shape of a particle attached to a specified boundary, boundary position was fixed relative to *Evolver*'s reference frame, the portion of the particle in C_1 was rotated relative to that in C_2 to define the crystallographic misorientation (relative to C_1), and both portions of the particle were then rotated relative to the boundary to define the average boundary orientation (relative to C_1).

Because Eq. (6.3) produces shapes with equilibrium orientations defined relative to *Evolver*'s reference frame, direct application of Eq. (6.3) gives boundaries of zero misorientation—*e.g.*, configurations where the $\{100\}$ orientations of C_1 and C_2 are parallel. Crystallographic misorientation was specified by rotating the normal components n_1, n_2, n_3 for the energy density of each element (Eq. (6.3)) in one phase (or grain) relative to those of the other by $\vec{\mathbf{R}}_\Phi$, a Rodrigues rotation matrix. The orientation of the two phases (or grains) relative to the boundary was then specified by a second rotation of normal components—this time the rotation was applied to the normal components of Eq. (6.3) describing interface in both phases (or grains). Figure 6.3 uses a grain boundary particle formed by two $\mathcal{W}$ that are identical truncated octahedra to demonstrate the successive rotations. Details are given in Appendix B.

6.4 An Energy-Minimizing Sequence

6.4.1 Introducing Anisotropy into an Isotropic Boundary Particle Shape

This thesis uses the following four steps to evolve the equilibrium shape of an anisotropic boundary particle attached to an isotropic boundary:

1. Replace *Evolver*'s default tension with γ_B for elements of boundary and forms of Eq. (6.3) for elements of particle interface using the $\{w_S, w_P, Q\}$ combination that gives the desired set of relative interfacial free energies on each side of the boundary.
2. Set $\alpha = 1$ to create the shape of an isotropic boundary particle (a lens).
3. Decrement α in small steps, re-calculating the equilibrium shape after each decrement, until $\alpha = 0$.
4. Repeat steps 2–3 for a total of three times, perturbing the surface between the repeats.

Fig. 6.4 shows images taken during an evolution for a particle of truncated octahedral $\mathcal{W}$ attached to a pure 15° twist isotropic grain boundary, where $\hat{\mathbf{n}}_{\mathrm{GB}}^{avg} =$

$\langle 001 \rangle$ with respect to grain C_1. The boundary tension is the same for all images, $0.75\,\gamma_{GB} = \gamma_{111}$, where γ_{111} refers to the $\{111\}$ facets that result for $\alpha = 0$.

Fig. 6.4(a) shows the coarse approximation to the boundary particle shape (a cube) given as input to *Evolver*. Fig. 6.4(b) shows the lenticular boundary particle of fixed volume calculated for $\alpha = 1$ (dihedral angle, $2\theta = 166^\circ$). Fig. 6.4(c) shows the $\alpha = 0.7$ shape, where the particle has not quite formed broad $\{100\}$ and $\{111\}$ orientations but still produces boundary ruffles where orientations sufficiently distanced on a unit sphere (*i.e.*, interfacial orientations that are not neighbors on a unit sphere) meet at the boundary. Fig. 6.4(d) shows the $\alpha = 0$ shape, where the particle is faceted and the facet energy densities are given in Table 6.3.2.

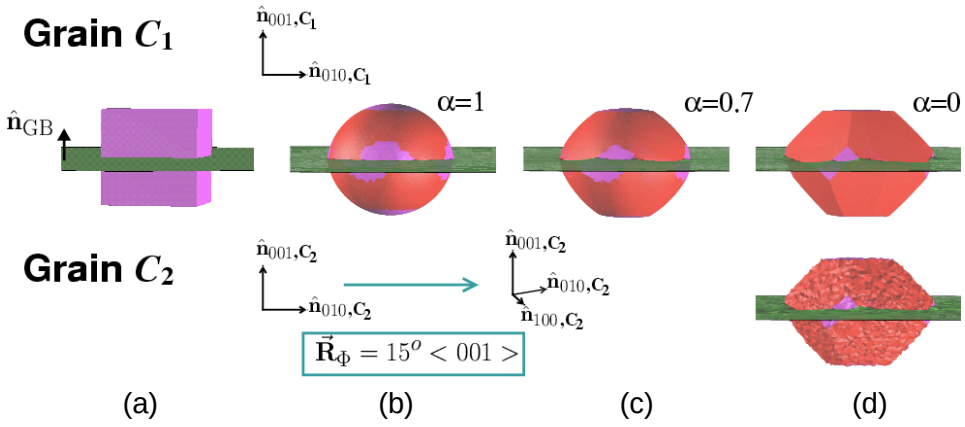

Figure 6.4: A typical evolution in *Evolver*, shown here for a truncated octahedron attached to a pure 15° twist boundary. Briefly: (a) the initial approximation to the equilibrium boundary particle configuration; (b) the isotropic shape evolved from (a); (c) the anisotropic shape resulting from $\alpha = 0.7$; (d) top, the anisotropic shape at $\alpha = 0$, and bottom, a "jiggled" shape that was used to test stability.

A "jiggled" shape, defined in Ch. 6.4.4, is shown below the faceted form in Fig. 6.4(d). Shapes calculated for successive α (neighboring shapes) are addressed in Ch. 6.4.3. Brief details of the calculation are given in Ch. 6.4.2.

6.4.2 Initial Iterations and Surface Operations

In this thesis, a "good" mesh is defined as one that does not produce configurations that are "stuck" due to, for instance, regions of crowded vertices. A good triangulated mesh is often formed of equiangular elements, and the input surface (Fig. 6.4(a)) was constructed so that when *Evolver* triangulates the surface, a nearly equiangular mesh results.

During calculations, a number of *Evolver* techniques were used to promote mesh uniformity. Vertex spacing was checked by *vertex averaging*, which weights centroids of facets meeting at a vertex by facet area to give a new vertex position, and *equiangulation*, which takes the polygon defined by two adjacent elements and switches the diagonal defined by the edge connecting them if a more equiangulated configuration would result. In addition, maximum and minimum areas and edge lengths were defined so as to *weed* (delete) tiny triangles and edges in addition to refining larger ones.

The dimensions of the particle in the input configuration were established to satisfy the volume constraint (Ch. 6.3.2) to avoid necessary adjustments prior to an energy minimization. The gradient descent method, briefly described in Ch. 6.2, was used to calculate a lenticular particle (Fig. 6.4(b)) for each of the three times $\alpha = 1$ in an evolution. The gradient descent method was used at these times because the $\alpha = 1$ solution is calculated from an input (Fig. 6.4(a)) or jiggled (bottom of Fig. 6.4(d)) configuration that is far from equilibrium, and other minimization methods, discussed in Ch. 6.4.3, are not suited to highly non-equilibrium states.

6.4.3 Convergence

Because the equilibrium configuration is generally not known *a priori*, there is currently no method to determine whether a configuration is converged. There are examples [97] of catenoid surfaces that appear converged but are in fact slowly approaching an energetic minimum, or even a saddle point in energy, that is several

iterations away.

To speed the approach to a minimum, the *conjugate gradient method* was used with a moderately refined mesh. Use of the method requires that the energy change continuously during a minimization, and because the it can be ineffective when a configuration is far from equilibrium, it was not used for input or jiggled configurations as in Fig. 6.4. The conjugate gradient method converges more quickly because, rather than taking orthogonal steps along an energy surface (gradient descent method), it takes steps that are "conjugate" to one another. In *Evolver*, the method builds a "history" vector that reduces the need to retrace steps along the energy surface [97].

The conjugate gradient method was used for the calculation of configurations with $\alpha < 1$. Because changes to properties of a configuration may change the energy surface, previously traced directions may need to be retraced. For this reason, the history vector was erased on each α decrement by toggling the conjugate gradient method off and then on again.

6.4.4 Stability

It is possible for an *Evolver* calculation to produce a configuration that is only in a local equilibrium. Generally, there is no guarantee that a global minimum is calculated. "Jiggling" (Fig. 6.4) is an *Evolver* technique that randomly displaces non-fixed vertices by amounts no greater than a user-defined maximum (given as a multiple of the mean edge length). Jiggling is useful for testing the relative stability of a configuration because it perturbs the surface from its current state.

To be effective, the amplitude of the perturbations should remove a configuration from its current equilibrium without changing the topology of (destroying) the surface. For this work, edge length was made a monotonically increasing function of distance from the particle, and a maximum of 5–6% the mean edge length was a sufficient amplitude. Configurations were converged, jiggled, and re-converged three times to ensure that *Evolver* produced the same equilibrium configuration from random starting points. Jiggling a converged shape with smaller perturbations (2-3% the mean edge length) was another method used to check the stability of a configuration. An example is shown in Fig. 6.4(d). In this case, the energy

of a jiggled shape was minimized without changing α, and the minimization reconverged to the original anisotropic shape.

The *Hessian*, the symmetric matrix of second derivatives of the energy, was another useful tool for testing stability. When a configuration is not at a saddle point and there are barriers to all energetic minima nearby, the Hessian is positive definite. Because equilibrium requires that perturbations to an interface increase the interfacial free energy under a given set of constraints, a Hessian that is not positive definite indicates that equilibrium has not been attained because there is no barrier to changes in configuration that decrease energy.

All positive eigenvalues indicate a positive definite Hessian. Eigenvalues that become negative indicate the appearance of modes of instability. Eigenvalues were therefore checked during an evolution to test the stability of a configuration.

The Hessian was also used in conjunction with the conjugate gradient method to speed convergence. To decrease the error in an approximation to a real configuration, interfaces were refined further in the final stages of an evolution. Because a good triangular mesh was kept throughout an evolution, perturbations during Hessian minimizations were restricted to lie normal to an interface at a vertex to reduce unnecessary searches for reductions in energy.

Chapter 7

Generalizations

The methods in Ch. 6.3 rely on algebraic expressions for $\gamma(\hat{\mathbf{n}})$ that have limited utility because they can only produce anisotropic shapes with cubic symmetry can be produced. This chapter gives a general method for defining a $\gamma(\hat{\mathbf{n}})$ that can be used to describe a $\mathcal{W}$ of any symmetry.

7.1 The Convex Surface Tension and its Relation to its $\mathcal{W}$

Every $\gamma(\hat{\mathbf{n}})$ has a unique $\mathcal{W}$, but a single $\mathcal{W}$ can be derived from an infinite number of $\gamma(\hat{\mathbf{n}})$. Physical equilibria depend only on $\mathcal{W}$. This result follows from the surface tension function that can be derived directly from $\mathcal{W}$ by equating the energy per unit projected area of any orientation that does not appear on $\mathcal{W}$ with the sum of the energy contributions of facets that join at a corner or edge which can be combined to give the same average orientation.

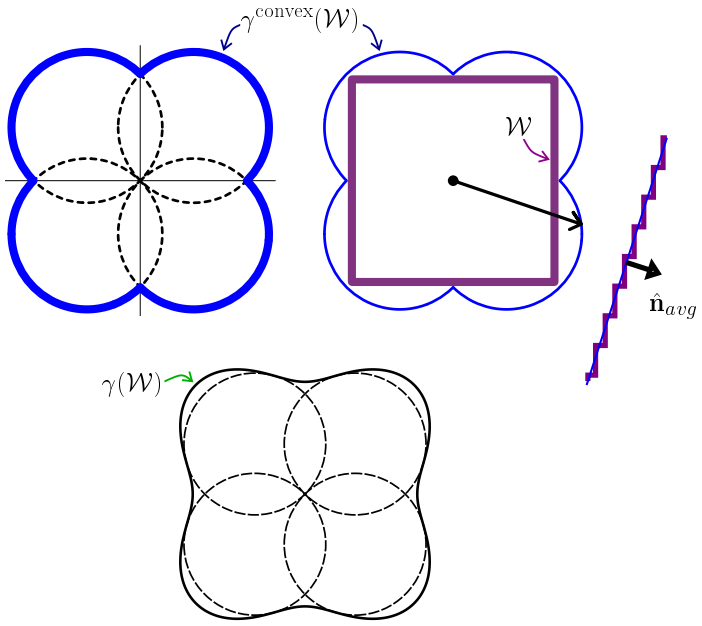

Figure 7.1: The convex surface tension construction builds $\gamma^{\text{convex}}(\mathcal{W})$ from $\mathcal{W}$ by intersecting spheres with the $\gamma(\hat{\mathbf{n}})$ origin and points corresponding to the energy of facets that meet along a corner. The outer envelope of the spheres gives $\gamma^{\text{convex}}(\mathcal{W})$ (top left), which is the lower bound of all $\gamma(\mathcal{W})$ giving $\mathcal{W}$ (top right). For interface described by $\gamma^{\text{convex}}(\mathcal{W})$, the energy density of an orientation absent from $\mathcal{W}$ cannot be reduced by the local formtion of steps from adjacent equilibrium orientations with dimensions equal to the projection of interfacial area onto the adjacent $\mathcal{W}$ interface. Considering only interfacial free energies, one member of an infinite set of stepped structures is shown in the figure for the fixed average orientation indicated.

This convex surface tension function (Fig. 7.1) puts the energy density of any (non-appearing) orientation on a sphere that has one point at the origin and is tangent to $\gamma(\hat{\mathbf{n}})$ at any facet orientation, reproducing the *Tangent Sphere* construction of Herring [24]. The minimal interfacial free energy density is thus defined for any polyhedral $\mathcal{W}$ by the outer envelope of spheres sharing the $\gamma(\hat{\mathbf{n}})$ origin and meeting at cusps defined by the intersections of two (orthogonal to $\mathcal{W}$ edges) or more (at $\mathcal{W}$ facets) spheres.

The minimal surface energy density is *convex* in the sense that the energy of any orientation cannot be further reduced by replacement with any other orientations which, when combined, preserve the original orientation. Interfaces that attain their convex energy with fixed $\hat{\mathbf{n}}_{\mathrm{B}}^{avg}$ as the only constraint will have no driving force to change morphology. Fig. 7.1 shows one member of an infinite set of stepped structures that are energetically equivalent to a boundary of $\hat{\mathbf{n}}_{\mathrm{B}}^{avg}$. If the average orientation constraint is relaxed, driving forces to rotate the interface into minimum energy orientations, *torques*, can exist. For interface enclosing a fixed (isolated) volume, the Wulff shape results because $\mathcal{W}$ gives the smallest interfacial free energy to volume ratio.

For demonstrations in this chapter, let the convex energy functions (representing the minimum energy density functions) be called $\gamma^{\mathrm{convex}}(\mathcal{W})$. Different $\gamma(\hat{\mathbf{n}})$ that have the same $\mathcal{W}$ will be called *equivalent* or *in the equivalence class* $\gamma(\mathcal{W})$ and denoted $\gamma(\mathcal{W})$ or $\gamma^{\mathcal{W}}(\hat{\mathbf{n}})$. All equivalent $\gamma(\mathcal{W})$ must lie outside $\gamma^{\mathrm{convex}}(\mathcal{W})$ except at facet orientations where they must coincide. It is necessary that any $\gamma(\mathcal{W})$ have cusps at least as "sharp" as those of $\gamma^{\mathrm{convex}}(\mathcal{W})$.

For numerical equilibrium calculations as in Ch. 6.2–6.4, any member of a $\mathcal{W}$'s equivalence class should give an identical result because the numerical method automatically "convexifies" $\gamma(\mathcal{W})$—for an interface that does not enclose a fixed volume, the method creates any $\hat{\mathbf{n}}_{\mathrm{B}}^{avg}$ from nearby orientations of $\mathcal{W}$ in proportions that map the resultant energy to the convexified surface tension, $\gamma^{\mathrm{convex}}(\mathcal{W})|_{\hat{\mathbf{n}}_{\mathrm{B}}^{avg}}$.

7.2 Algebraic Formulations for an Instance of $\gamma(\mathcal{W})$

To produce energetically favorable orientations, $\gamma^{\mathcal{W}}(\hat{\mathbf{n}})$ are constructed from functions that have minima at specified $\hat{\mathbf{n}}$. The precise shape of a $\gamma^{\mathcal{W}}(\hat{\mathbf{n}})$ depends

on how the "distance" between $\hat{\mathbf{n}}$ and an energy minimum orientation is quantified. Generally, reconstructions of observed crystalline $\mathcal{W}$ do not require the detailed knowledge of the shapes of plots of the interfacial free energy density. However, exact $\gamma^{\mathcal{W}}(\hat{\mathbf{n}})$, or portions of them, are necessary for $\mathcal{W}$ that contain contiguous orientations of interface and for changes to $\mathcal{W}$ with an intensive variable.

The general method of forming a $\gamma^{\mathcal{W}}(\hat{\mathbf{n}})$ that takes distance from specified minima as a parameter is given here:

1. Choose the orientations of $\gamma^{\mathcal{W}}(\hat{\mathbf{n}})$ minima.
2. Choose a metric to describe $\chi(\hat{\mathbf{n}})$, the distance between the orientations of these minima and an arbitrary orientation.
3. Use $\chi(\hat{\mathbf{n}})$ with $\gamma(\mathcal{W}^{\text{sphere}})$, the isotropic surface tension that results in the absence of minima, to define a $\gamma^{\mathcal{W}}(\hat{\mathbf{n}})$ that is HD1.

A $\gamma^{\mathcal{W}}(\hat{\mathbf{n}})$ is formulated by considering, for every orientation $\hat{\mathbf{n}}$, the distance between $\hat{\mathbf{n}}$ and each minima weighted by the depth of the minima relative to an isotropic reference of radius $\gamma(\mathcal{W}^{\text{sphere}})$. When there is only one minimum, located at $\hat{\mathbf{n}}^{\text{fixed}}$, the formulations can take the following form,

$$\gamma(\vec{\mathbf{A}},\eta) = A\gamma(\mathcal{W}^{\text{sphere}})\left[1-\eta\left(\frac{t_{max}-\chi(\hat{\mathbf{n}})}{t_{max}-t_{min}}\right)\right] = A\gamma(\mathcal{W}^{\text{sphere}})\left[1-\eta T(\hat{\mathbf{n}})\right] \tag{7.1}$$

where η determines the depth of the minimum relative to $\gamma(\mathcal{W}^{\text{sphere}})$, and $\chi(\hat{\mathbf{n}})$ is the distance (taken according to an as of yet unspecified metric) between a point $\gamma(\mathcal{W}^{\text{sphere}})\hat{\mathbf{n}}$ on $\mathcal{W}^{\text{sphere}}$ and $\gamma(\mathcal{W}^{\text{sphere}})\hat{\mathbf{n}}^{\text{fixed}}$. Variables t_{max} and t_{min} are the maximum and minimum possible $\chi(\hat{\mathbf{n}})$ values, giving $T(\hat{\mathbf{n}}) = 1$ when $\hat{\mathbf{n}}$ points directly toward the minimum and $T(\hat{\mathbf{n}}) = 0$ when $\hat{\mathbf{n}}$ points directly opposite the minimum.

Equation (7.1) is generally an approximation to a single-facet $\mathcal{W}$, and the convexified $\gamma^{\mathcal{W}}(\hat{\mathbf{n}})$ is defined by the outer envelope of spheres passing through the origin and adjacent minima. For the non-polyhedral $\mathcal{W}$ above, one minimum generates a broad facet and a nearby continuous set of minima generates the smoothly curved portion of $\mathcal{W}$. Equation (7.1) is an approximation if the $\gamma(\hat{\mathbf{n}})$ do not match, exactly, the set of minima producing the curved portion of $\mathcal{W}$.

When $\gamma(\hat{\mathbf{n}}, \eta)$ contains multiple minima, the a factor that specifies the reduction in energy must account for the proximity and depth of neighboring minima. In this case, the single distance must be replaced with a summation over all minima weighted by a factor that yields the desired reduction in energy for a fixed η

$$\gamma(\vec{\mathbf{A}}, \eta) = A\gamma(\mathcal{W}^{\text{sphere}}) \left(1 - \eta \sum_{i=1}^{m} \omega_i T_i(\hat{\mathbf{n}})\right) \tag{7.2}$$

where m is the total number of minima, ω_i shifts minimum i to the desired depth, $T_i(\hat{n})$ denotes $(t_{max} - t_i(\hat{\mathbf{n}}))/(t_{max} - t_{min})$, and $t_i(\hat{\mathbf{n}})$ is the distance between $\hat{\mathbf{n}}$ and the orientation of minimum i.

For a set of symmetry-related minima—*i.e.*, minima of equal depth with identical arrangements of neighboring minima—ω_i is a constant, and the following example in $\mathbf{R^2}$ demonstrates the utility of Eu. (7.2). Let Eq. 7.2 converge to the equivalence class of a square $\mathcal{W}$ with $\{10\}$ facets ($m = 4$) at $\eta = 0$ Let $t_i(\hat{\mathbf{n}})$ for this example be taken with the Euclidean metric, given as the length of the chord connecting general points $\gamma(\mathcal{W}^{\text{sphere}})\hat{\mathbf{n}}$ to orientations on $\gamma(\mathcal{W}^{\text{sphere}})$. For the $\hat{\mathbf{n}}$ that point along the a $\{10\}$ minima orientation,

$$\gamma(\vec{A}, \eta)|_{\hat{\mathbf{n}}=\langle 10\rangle} = \gamma(\mathcal{W}^{\text{sphere}})A \left[1 - \eta\omega \left(1 + \frac{2-\sqrt{2}}{2} + \frac{2-\sqrt{2}}{2} + 0\right)\right] \tag{7.3}$$

The *anisotropic limit*, defined as $\eta = 1$, can be specified with ω. (In terms of the anisotropy factor in Ch. 6.1 and 6.4, $\eta = 1 - \alpha$.) Equation (7.3) shows that if, for instance, $\hat{\mathbf{n}}$ points toward the (10) minimum, the interfacial free energy at that minimum is not influenced by the minimum at $(\bar{1}0)$ but is slightly influenced by the (01) and $(0\bar{1})$ minima.

For two distinct minima occurring along $\hat{\mathbf{n}}_1$ and $\hat{\mathbf{n}}_2$, the expression relating ω_2 to ω_1 can be determined from

$$R_{12} = \frac{\gamma(\hat{\mathbf{n}}_1, \eta)}{\gamma(\hat{\mathbf{n}}_2, \eta)} \qquad (\eta = \text{ fixed}) \tag{7.4}$$

where R_{12} is the magnitude of $\gamma(\hat{\mathbf{n}}_1, \eta)$ relative to $\gamma(\hat{\mathbf{n}}_2, \eta)$. Solving for ω_2,

$$\omega_2 = \frac{\omega_1 \left[1 - R_{12} T_2(\hat{n}_1)\right] + \frac{1}{\eta}\left[R_{12}(1-q_2) - (1-q_1)\right]}{\left[R_{12} - T_2(\hat{n}_1)\right]} \tag{7.5}$$

The q_1 and q_2 are positive constants corresponding to the remainder of the summations in $\gamma(\hat{\mathbf{n}}_1,\ \eta)$ and $\gamma(\hat{\mathbf{n}}_2,\ \eta)$. This expression shows that it becomes increasingly difficult (ω_2 must be very large) to satisfy Eq. (7.4) both in the *isotropic limit* ($\eta = 0$) and as the distance between the minima of $\hat{\mathbf{n}}_1$ and $\hat{\mathbf{n}}_2$ approaches R_{12}. The expression also shows that the value of ω_2 reflects the effect of neighboring minima. If $\gamma(\hat{\mathbf{n}}_1, \eta) > \gamma(\hat{\mathbf{n}}_2, \eta)$, a smaller ω_2 is needed when q_2 is large because this implies that $\hat{\mathbf{n}}_2$ is close to very deep or several minima that reduce $\gamma(\hat{\mathbf{n}}_2, \eta)$. Direct control over multiple distinct sets of minima may require an iterative solution to a set of equations resulting from Eq. (7.2) because adjusting ω_i for one set of minima can affect the relative depth of all minima.

7.3 An Example: Straight-Line Distance Between Points on the Unit Sphere

Consider two orientations $\hat{\mathbf{n}}$ and $\hat{\mathbf{n}}^{\text{fixed}}$, where $\hat{\mathbf{n}}^{\text{fixed}}$ denotes the orientation of a $\gamma^{\mathcal{W}}(\hat{\mathbf{n}})$ minimum. The distance between these orientations could be taken as, for instance, the geodesic, chord, or a projection of the chord that connects them.

Not all measures of distance work correctly. Projections of chords along, for instance, the diameter of $\gamma(\mathcal{W}^{\text{sphere}})$ yield spherical $\mathcal{W}$—*i.e.*, the set of $\vec{\xi}$ that results from taking the gradient of $\gamma^{\mathcal{W}}(\vec{\mathbf{A}})$ with respect to $\vec{\mathbf{A}}$ is not useful for anisotropic shapes because it always traces a sphere that is displaced along $-\hat{\mathbf{n}}^{\text{fixed}}$. The measures of distance that do work do not generally give the exact same results—although different quantifications of $\chi(\hat{\mathbf{n}})$ can produce γ–minima of specified depths in specified orientations, the shape of the minima, and thus the number and relative amounts of low energy orientations on $\mathcal{W}$, can differ.

Only results from using the chord distance will be shown here because calculations using the formulations developed with geodesics and angular distances are more computationally intensive. Details of formulations using these other metrics

are reported elsewhere [101].

When quantified as the magnitude of a chord, $\chi(\hat{\mathbf{n}})$ uses the Euclidean metric, where $\chi(\hat{\mathbf{n}}) = \|\hat{\mathbf{n}}^{\text{fixed}} - \hat{\mathbf{n}}\|$. Consider the following example in $\mathbf{R^2}$. This $\chi(\hat{\mathbf{n}})$ gives

$$\gamma^{\mathcal{W}}(\vec{\mathbf{A}}, \eta) = Au\gamma\left[1 - \eta\left(1 - \tfrac{v}{2}\right)\right] \qquad u = \sqrt{n_1^2 + n_2^2} \qquad v = \sqrt{2 - \tfrac{2n_1}{u}} \tag{7.6}$$

for $\hat{\mathbf{n}}^{\text{fixed}} = \langle 10 \rangle$. The corresponding $\vec{\xi}$ is

$$\vec{\xi}^{\mathcal{W}}(\hat{\mathbf{n}}, \eta) = \left\langle \frac{-n_2^2\eta}{2u^2v} + \left(1 + \eta\left(\frac{v}{2} - 1\right)\right)\frac{n_1}{u},\ \ \frac{n_1 n_2 \eta}{2u^2v} + \left(1 + \eta\left(\frac{v}{2} - 1\right)\right)\frac{n_2}{u} \right\rangle \tag{7.7}$$

Equation (7.6) calculates a shape in $\mathbf{R^2}$ with a single facet. Although $\mathcal{W}$ with a single facet connected by a point (an edge in $\mathbf{R^3}$) to a smoothly curved (*i.e.*, rough) portion of interface is artificial, it is used for the example because it is a useful test case.

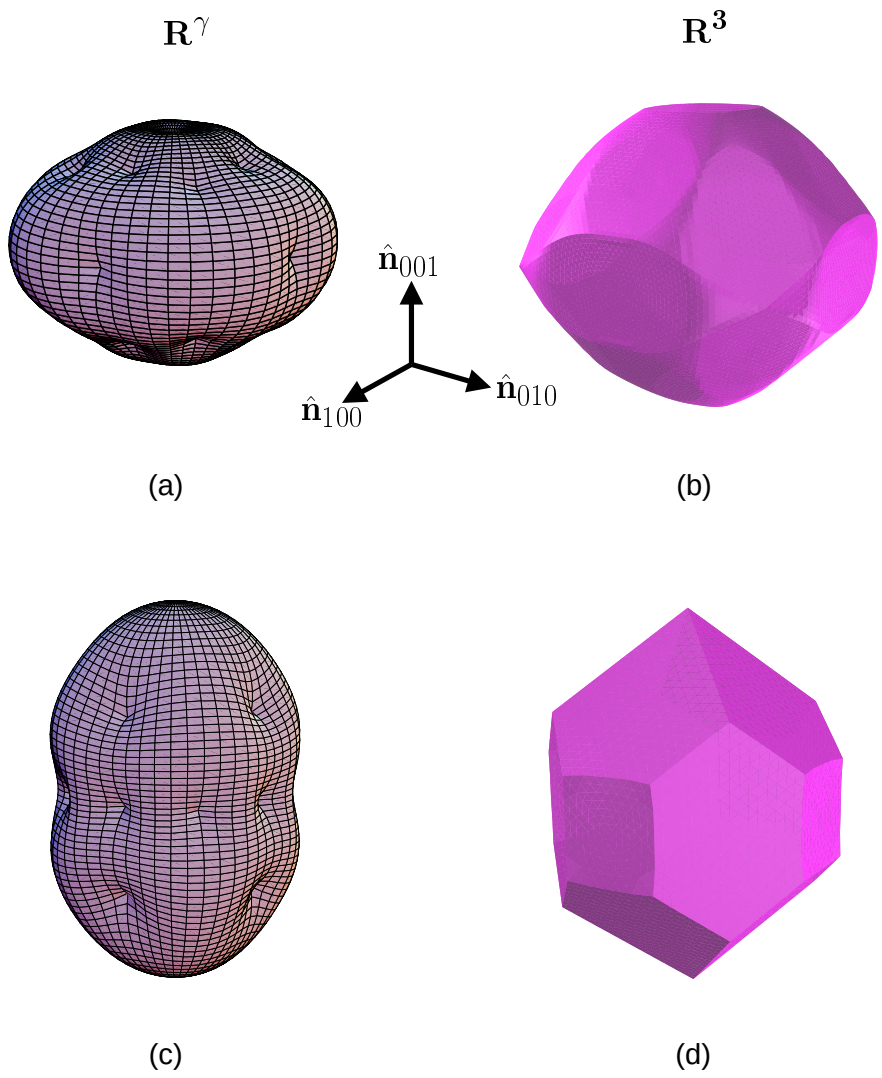

Figure 7.2: Plots of $\gamma(\mathcal{W})$ and $\vec{\xi}(\mathcal{W})$ calculated using $\chi(\hat{\mathbf{n}})$ defined as a chord between an arbitrary orientation and orientations of $\gamma(\mathcal{W})$–minima: (a) $\gamma^{\mathcal{W}}(\hat{\mathbf{n}})$–plot with minima in $\langle 100\rangle$, $\langle 111\rangle$, $[101]$, $[\bar{1}01]$, $[\bar{1}0\bar{1}]$, $[10\bar{1}]$, $[011]$, $[0\bar{1}1]$, $[0\bar{1}\bar{1}]$, and $[01\bar{1}]$ directions, (b) the particle $\mathcal{W}$ calculated from (a), (c) $\gamma^{\mathcal{W}}(\hat{\mathbf{n}})$–plot with minima in $\langle 110\rangle$, $[100]$, $[\bar{1}00]$, $[010]$, and $[0\bar{1}0]$ directions, (d) the particle $\mathcal{W}$ calculated from (c).

Figure 7.2 illustrates the utility of the $\chi(\hat{\mathbf{n}})$ based on a chord for calculations of $\mathcal{W}$ in $\mathbf{R^3}$. The figure gives two examples of $\gamma^{\mathcal{W}}(\hat{\mathbf{n}})$ that, when applied using the *Evolver* methods in Ch. 6.1–6.4, calculate $\mathcal{W}$ with various symmetry. The first example is given in Fig. 7.2(a)-(b) and shows a shape with facets in $\{110\}$, (100), $(\bar{1}00)$, (010), and $(0\bar{1}0)$ orientations; the second is given in Fig. 7.2(c)-(d) and shows a shape with facets in $\{100\}$, $\{111\}$, and (101), $(\bar{1}01)$, $(\bar{1}0\bar{1})$, $(10\bar{1})$, (011), $(0\bar{1}1)$, $(0\bar{1}\bar{1})$, and $(01\bar{1})$ orientations. Both cases produce shapes with $4/m\,2/m\,2/m$ point group symmetry.

Part III

Calculated Results and Their Implications

Chapter 8

Boundary Particle Shapes in Dilute Pb-Al Systems

This chapter is a motivation for Chs. 9–11, which give numerical results similar to boundary particle shapes observed through transmission electron microscopy (TEM) in dilute lead-aluminum alloys [50, 100]. Consider the micrograph in Fig. 8.1(a), which is a planar projection of a Pb boundary particle attached to an Al grain boundary that rumples around the particle. It is not clear that boundary distortion is due entirely to the particle shape, but the numerical result in Fig. 8.1(b) that approximates the configuration shows the particle to rumple the boundary. Nearly all boundary particles in the Pb-Al system are observed as in the figure—single crystals that are fully faceted to one side of the boundary but curved (rough) to the other.

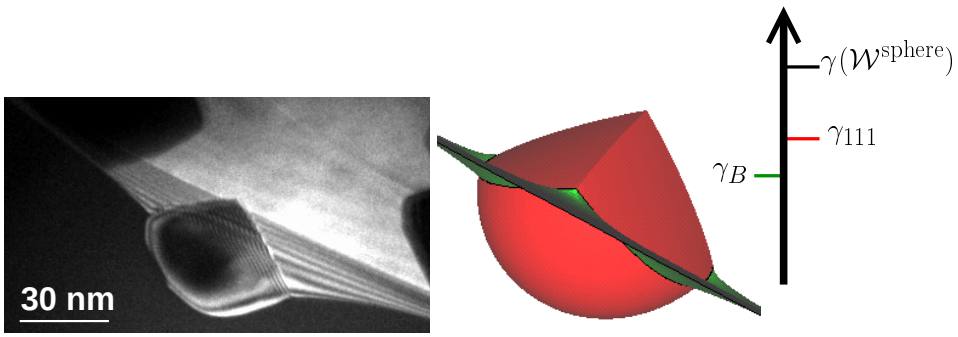

Figure 8.1: (a) A TEM micrograph of a Pb grain boundary particle in Al. The particle is a single crystal and forms $\{111\}$ facets in the top grain and a spherical cap in the bottom grain. Thickness fringes mark variations to the inclination of boundary and thus characterize the boundary distortion. *(Courtesy of Tamara Radetic, NCEM, LBNL.)* (b) A calculated particle that forms $\{111\}$ facets in C_1 and a spherical cap in C_2. The relative interfacial free energies for the calculation are $\gamma_B = 0.5\gamma(\mathcal{W}^{\mathrm{sphere}})$ and $\gamma_B = 0.75\gamma_{111}$. Both (a) and (b) show the boundary to rumple around the particle.

Boundary particle calculations apply to a number of material systems [47, 100, 102]. The Pb-Al system is particularly well-suited for comparison with equilibrium calculations for the following reasons [100]:

1. Both Pb and Al have face-centered cubic crystal structures, and the Pb particles topotactically align so that $\{111\}$ particle and matrix orientations are parallel, giving nearly atomically smooth interfaces.
2. At room temperature, Al vacancies are sufficient in number and mobility to give "strain-free" configurations for small Pb particles, despite the incoherency that results from a lattice parameter mismatch of $\sim$22%.
3. The system has been studied extensively and is well-characterized.

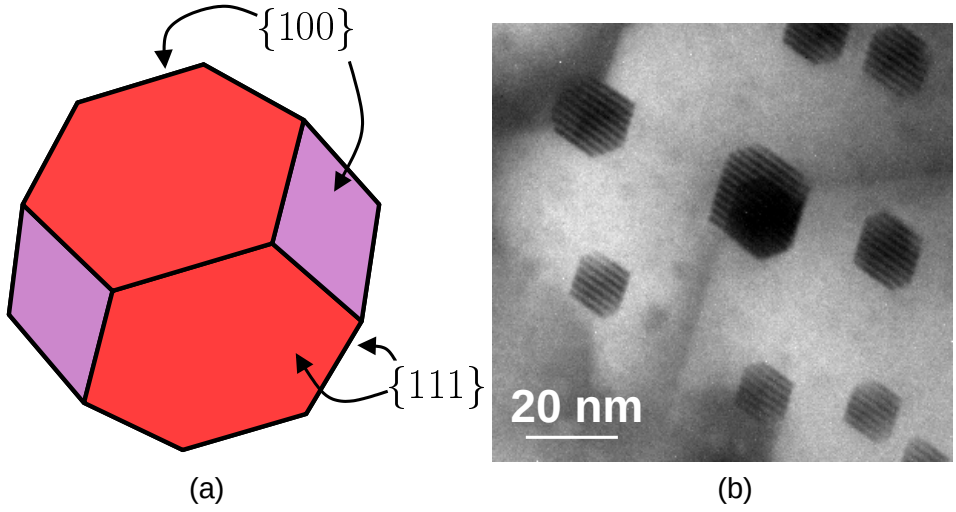

Figure 8.2: (a) The truncated octahedron calculated with Wulffman [103] that results for an aspect ratio of 1.15. The shape is oriented to show the $\{100\}$ and $\{111\}$ facet positions when viewed near a $\langle 110 \rangle$ axis. (b) Observations of Pb nanoparticles embedded within a single grain of Al imaged along a $\langle 110 \rangle$ zone axis indicate that $\gamma_{100}/\gamma_{111} \approx 1.15$. *(Courtesy of Lihua Zhang, NCEM, LBNL.)*

The Wulff shape of a single crystal of Pb embedded in Al is a truncated octahedron, which has cubic symmetry and is defined by eight $\{111\}$ and six $\{100\}$ facets (Fig. 8.2(a)). Because the time necessary for reaching an equilibrium shape increases rapidly with particle size [104], small ($10 - -30$ nm) particles are typically used for interfacial free energy measurements. The relative heterophase interfacial free energies taken from Pb particles in Al with shapes attributed to a minimum in interfacial free energy are reported [50] as $\gamma_{100}/\gamma_{111} \approx 1.15$.

The Pb particle in Fig. 8.2(a) is imaged close to a $\langle 110 \rangle$ axis. As shown in Fig. 8.2(a), the perimeter of the faceted portion of the particle is then defined by (100) facets (seen nearly edge-on) and edges of (111) facets. (The particles are not typically imaged directly along $\langle 110 \rangle$ in order to diminish the influence of the Al matrix [100].)

The following chapters demonstrate the influence of interfacial free energy and geometry on heterogeneous nucleation, microstructural torques, and the spatial distribution of anisotropic boundary particles—results that can be compared directly to Pb boundary particles in Al and boundary particles in other systems where a minimization of interfacial free energy determines particle shape (*e.g.*, for small particle volumes that produce little, if any, strain energy).

Chapter 9

Equilibrium Configurations for Heterogeneous Nucleation

9.1 Brief Review of Heterogeneous Nucleation

Simple models of homogeneous nucleation at constant T take the reduction in chemical free energy accompanying the formation of a volume of new phase as the only driving force and the creation of new interface as the only restraint. The nucleation barrier that results, ΔG^*, holds under the assumption that other contributions to the energy, *e.g.*, those from elastic strains, are negligible.

A probability factor exponentially dependent on the barrier, $\exp(-\Delta G^*/kT)$, governs the nucleation rate and the induction time for establishing steady-state nucleation at small undercoolings [60]. Microstructural features such as grain size and particle distribution, which influence the properties (*e.g.*, mechanical and electrical) and thus performance of a material in applications, are often dependent on the nucleation rate.

Generally, ΔG^* is reduced through heterogeneous nucleation, which occurs when nuclei remove free energy due to existing defects. For instance, the nucleation barrier for an isotropic grain boundary particle (consisting of identical portions of spheres) is a fraction, $f(\theta)$, of that for its homogeneous analogue (a sphere embedded within a single grain) for an equivalent driving force and equivalent interfacial free energies. The fraction is $f(\theta) = \frac{1}{2}(1-\cos\theta)^2(2+\cos\theta)$, which is

dependent on the decrease in boundary energy relative to the increase in particle interfacial energy through 2θ, the dihedral angle.

Chapters 9.2–9.5 examine the effect of anisotropic interfacial free energy on the heterogeneous nucleation barrier for particles attached to grain boundaries, heterophase interfaces, and interface junctions. Results in these sections hold for small particles that nucleate incoherently (*i.e.*, particles that do not modify elastic energy) when thermal fluctuations are negligible and boundary energy is isotropic in both $\hat{\mathbf{n}}_{\mathrm{B}}$ and $\vec{\mathbf{R}}_{\Phi}$. These assumptions are, in most cases, not realistic, but they allow the isolation of the effect of particle anisotropy on the nucleation barrier.

9.2 Effect of Particle Anisotropy on Nucleation Barriers

Many examples show the nucleation barrier to be influenced by the *shape* a particle takes as well as *where* it nucleates [53, 54]. The *homogeneous* nucleation barrier, $\Delta G^{*}_{\mathrm{HOM}}$, is minimized when a particle assumes its Wulff shape.

Members of continuous families of $\mathcal{W}$ can give different $\Delta G^{*}_{\mathrm{HOM}}$ and, as a result, different nucleation kinetics. For example, a study [53] following observations [105] of zinc alloys showed the steady-state nucleation rate to increase by a factor of $\sim 10^{25}$ relative to an isotropic particle for ellipsoidal $\mathcal{W}$ of increasing eccentricity. This study used the interfacial free energy density of the isotropic particle as the maximum in the ellipsoidal $\gamma(\hat{\mathbf{n}})$–plots.

Figure 7 from [67] considers flat grain boundaries to show that the *heterogeneous* nucleation barrier, $\Delta G^{*}_{\mathrm{HET}}$, of an isotropic particle decreases from replacing a grain boundary to a grain edge formed by three boundaries to a grain corner formed by four boundaries, for identical grain boundary free energies that are not large enough to produce perfect wetting. A portion of the plot is reproduced in Fig. 9.1 for an isotropic grain boundary particle formed by portions of $\mathcal{W}^{\mathrm{sphere}}$ and demonstrates that, for this particle, $\Delta G^{*}_{\mathrm{HET}} \to \Delta G^{*}_{\mathrm{HOM}}$ as $\gamma_{\mathrm{GB}} \to 0$ and $\Delta G^{*}_{\mathrm{HET}} \to 0$ as $\gamma_{\mathrm{GB}} \to 2\gamma(\mathcal{W}^{\mathrm{sphere}})$.

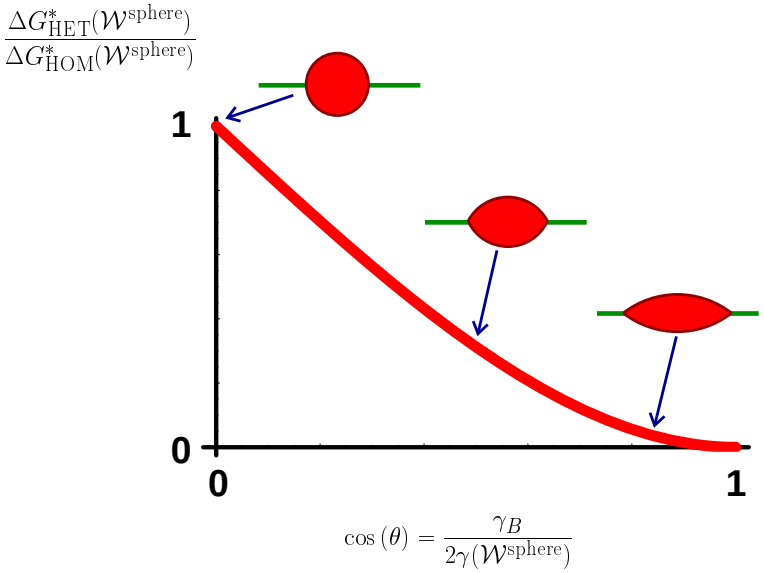

Figure 9.1: Reduction in the nucleation barrier for an isotropic particle at a flat boundary relative to the nucleation barrier for the particle within a single grain as the condition for perfect wetting is approached, *i.e.*, as $\gamma_B/2\gamma(\mathcal{W}^{\mathrm{sphere}}) \rightarrow 1$, after [67]

It is instructive to rebuild Fig. 9.1 to consider the effect of anisotropy. Here, the nucleation of a faceted boundary particle is compared to the homogeneous nucleation of a sphere. To facilitate later discussions involving changes in shape for a fixed boundary energy, a third axis is added to the plot to allow variations in the Wulff shape of the particle (*i.e.*, the shape the particle would take if it were removed from the boundary and located within a single grain).

Consider a particle that nucleates homogeneously in grains C_1 and C_2 as a parallelepiped with two square facets of $\gamma^{\mathrm{SQ}}(\mathcal{W}^{\mathrm{plpd}})$ and four rectangular facets of $\gamma^{\mathrm{RC}}(\mathcal{W}^{\mathrm{plpd}})$, where $\gamma^{\mathrm{SQ}}(\mathcal{W}^{\mathrm{plpd}}) \leq \gamma^{\mathrm{RC}}(\mathcal{W}^{\mathrm{plpd}})$. Examples of the shape are shown in Fig. 9.2. The distance between the square facets is proportional to $\gamma^{\mathrm{SQ}}(\mathcal{W}^{\mathrm{plpd}})$, and $\mathcal{W}^{\mathrm{plpd}}$ describes a family of shapes bounded by a cube and a square plate of infinitesimal thickness.

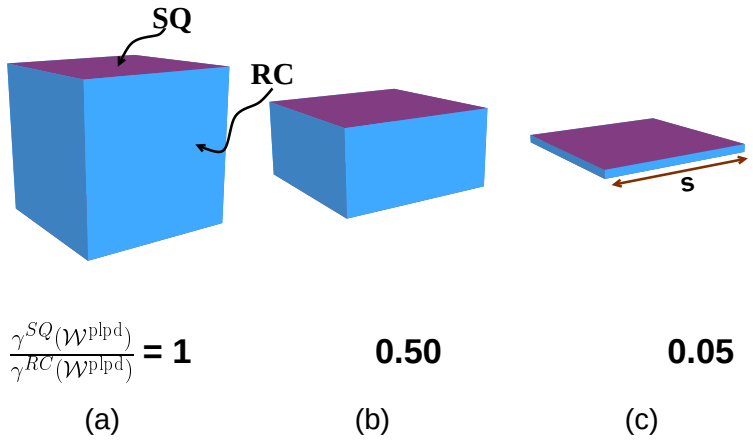

Figure 9.2: Variation in $\mathcal{W}^{\mathrm{plpd}}$ for different values of $1 \geq \frac{\gamma^{\mathrm{SQ}}(\mathcal{W}^{\mathrm{plpd}})}{\gamma^{\mathrm{RC}}(\mathcal{W}^{\mathrm{plpd}})} \geq 0$, calculated with Wulffman [103]. The square (SQ) facets are magenta and the rectangular ones (RC) are cyan. (a) $\gamma^{\mathrm{SQ}}(\mathcal{W}^{\mathrm{plpd}}) = \gamma^{\mathrm{RC}}(\mathcal{W}^{\mathrm{plpd}})$ produces a cube, (b) $\gamma^{\mathrm{SQ}}(\mathcal{W}^{\mathrm{plpd}}) = 0.50\gamma^{\mathrm{RC}}(\mathcal{W}^{\mathrm{plpd}})$ produces a shape with four rectangular facets having dimensions of $s \times 0.50s$, and (c) $\gamma^{\mathrm{SQ}}(\mathcal{W}^{\mathrm{plpd}}) = 0.05\gamma^{\mathrm{RC}}(\mathcal{W}^{\mathrm{plpd}})$ produces a shape with four rectangular facets having dimensions of $s \times 0.05s$.

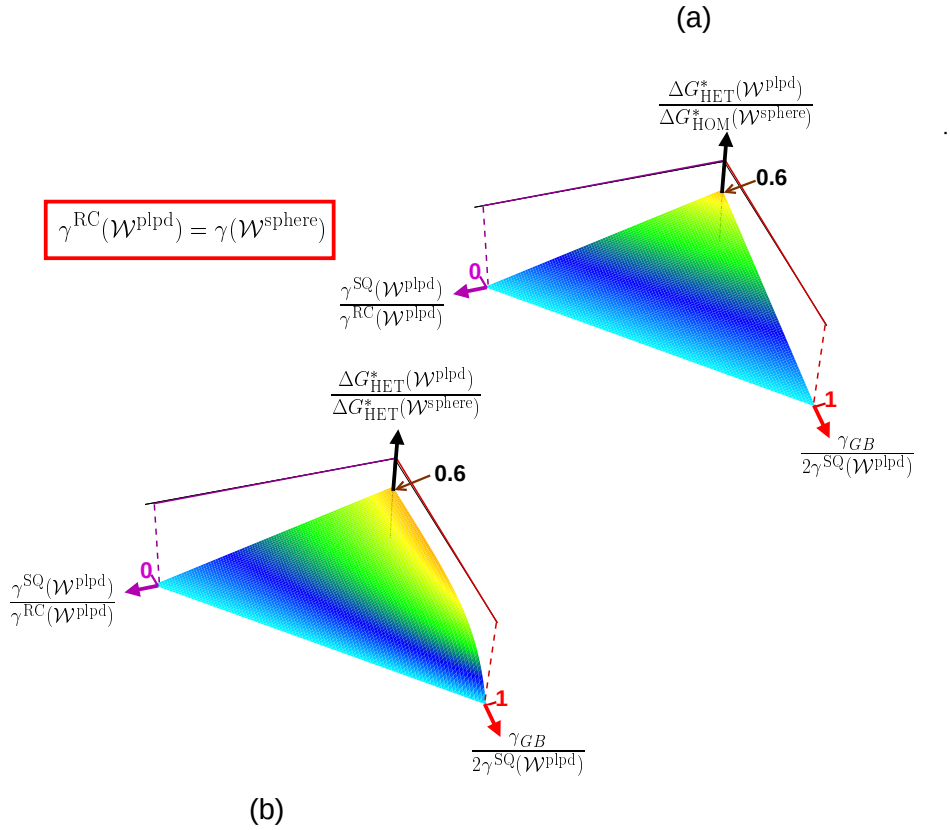

Figure 9.3: Heterogeneous nucleation barrier for a particle with a parallelepiped $\mathcal{W}$ with two square facets at a boundary relative to: (a) the homogeneous nucleation of a sphere and (b) the heterogeneous nucleation of a lens (isotropic particle) at the same boundary. In both cases, the isotropic interfacial free energy is $\gamma^{\rm RC}(\mathcal{W}^{\rm plpd}) = 0.7\gamma(\mathcal{W}^{\rm sphere})$, and the boundary acts as a mirror plane oriented parallel to the square facets.

Attach this particle to a grain boundary oriented parallel to the low energy square facets of $\mathcal{W}^{\rm plpd}$. Let the boundary act as a mirror plane, so that the *grain boundary* particle shape is a cube in the limit of $\gamma_{\rm GB} \to 0$ but a slab with one set of parallel square facets for $0 < \gamma_{\rm GB} < 2\gamma^{\rm SQ}(\mathcal{W}^{\rm plpd})$. Fig. 9.3 shows two plots: one gives $\Delta G^*_{\rm HET}$ for $\mathcal{W}^{\rm plpd}$ relative to $\Delta G^*_{\rm HOM}$ for an isotropic particle (a sphere described by $\mathcal{W}^{\rm sphere}$ and nucleating in a single grain), and the other gives $\Delta G^*_{\rm HET}$ for $\mathcal{W}^{\rm plpd}$ relative to $\Delta G^*_{\rm HET}$ for an isotropic particle (a lens nucleating at the same

boundary as the parallelepiped particle). In both plots, the isotropic interfacial free energy density is $0.7\gamma(\mathcal{W}^{\text{sphere}}) = \gamma^{\text{RC}}(\mathcal{W}^{\text{plpd}})$. The first plot is an anisotropic analogue to the portion in Fig. 7 of [67] describing boundary replacement. The second plot is of interest for this thesis.

Because ΔG^* is dependent on the Wulff shape, it is a function of $\mathcal{W}$. This is illustrated in Fig. 9.3(a), where variations in $\Delta G^*_{\text{HET}}(\mathcal{W}^{\text{plpd}})/\Delta G^*_{\text{HOM}}(\mathcal{W}^{\text{sphere}})$ with $\gamma_{\text{GB}}/2\gamma^{\text{SQ}}(\mathcal{W}^{\text{plpd}})$ are shown for each member of $\mathcal{W}^{\text{plpd}}$. In the figure, the homogeneous nucleation barrier for parallelepipeds relative to that of a sphere is described along $\gamma_{\text{GB}} = 0$. The homogeneous ($\gamma_{\text{GB}} = 0$) case has been studied [54] for applications in nickel-aluminum and copper-cobalt alloys, although the normalizations in those studies were reported relative to the homogeneous nucleation barrier for a cube of $\gamma^{\text{RC}}(\mathcal{W}^{\text{plpd}})$ rather than a sphere. The heterogeneous nucleation barrier for the a particle formed by portions of cubes is described along $\gamma^{\text{SQ}}(\mathcal{W}^{\text{plpd}}) = \gamma^{\text{RC}}(\mathcal{W}^{\text{plpd}})$. Other points on the surface in the plot correspond to the heterogeneous nucleation of a parallelepiped relative to the homogeneous nucleation of a sphere. In all cases, $\Delta G^*_{\text{HET}}(\mathcal{W}^{\text{plpd}}) < \Delta G^*_{\text{HOM}}(\mathcal{W}^{\text{sphere}})$, meaning that the faceted boundary particles nucleate more easily in this example.

It is convenient to consider normalizations to a heterogeneous nucleation reference to determine the effect of $\mathcal{W}$ on the reduction in the nucleation barrier at a fixed γ_{GB}. That is, it is convenient to consider $\Delta G^*_{\text{HET}}(\mathcal{W}^{\text{plpd}})/\Delta G^*_{\text{HET}}(\mathcal{W}^{\text{sphere}})$ rather than $\Delta G^*_{\text{HET}}(\mathcal{W}^{\text{plpd}})/\Delta G^*_{\text{HOM}}(\mathcal{W}^{\text{sphere}})$. Figure 9.3(b) uses this normalization and thus differs from Fig. 9.3(a) in that the heterogeneous nucleation barrier at a given γ_{GB} is normalized to the heterogeneous nucleation barrier of a sphere at that γ_{GB}. The plot shows that the faceted boundary particles nucleate more easily than the isotropic ones, the relative heterogeneous nucleation barrier is more strongly dependent on $\gamma^{\text{SQ}}(\mathcal{W}^{\text{plpd}})/\gamma^{\text{RC}}(\mathcal{W}^{\text{plpd}})$ than γ_{GB} for $\gamma_{\text{GB}} < 1.76\gamma^{\text{SQ}}(\mathcal{W}^{\text{plpd}})$. The strong dependence on $\gamma^{\text{SQ}}(\mathcal{W}^{\text{plpd}})$ occurs because the boundary is replaced with *two* interfaces of $\gamma^{\text{SQ}}(\mathcal{W}^{\text{plpd}})$. Heterogeneous normalizations relative to isotropic boundary particles are applied again in the following sections.

9.3 Previous Work

Aaronson and Aaron [106] have shown that: (1) the heterogeneous nucleation

barrier for boundary particles with equilibrium shapes that are spherical caps containing one low energy facet that does not intersect the boundary is less than that for those that are fully isotropic, and (2) the reduction in the barrier is invariant to which orientation (that does not produce a facet-boundary intersection) the facet takes. They concluded the same for particles with one set of parallel facets.

Their work followed detailed observations [51] of cellular precipitation for boundary tin particles in lead and was one of the first attempts to quantify effects of boundary particle anisotropy on nucleation. Later numerical investigations of Lee and Aaronson [56, 57] concluded that, for these cases, the maximum reduction in the heterogeneous nucleation barrier occurs when facets do not intersect the boundary.

The observations [51] indicated that, when facet-boundary intersections occur, the boundary distorts to accommodate them. Lee and Aaronson [57] applied finite difference methods to calculate boundary particle configurations, with patches of catenoid (zero mean curvature) surface approximating the "Tu-Turnbull 'puckering' " required for a critical nucleus with known oriented $\mathcal{W}$s. For each case, the boundary was assumed isotropic in $\hat{\mathbf{n}}_{\mathrm{B}}$.

Lee and Aaronson obtained their results by adapting configurations found to minimize energy for boundary particles of fixed volume attached to a boundary with fixed endpoints embedded in $\mathbf{R^2}$ [56] as input for calculations in $\mathbf{R^3}$ [57]. Variational calculus was applied to the integral of the sum of (the change in chemical free energy) and (the change in interfacial free energy) over a region bounded by the closed curve defining the particle/boundary junction to find the energy-minimizing particle shape. The additional boundary area required to accommodate the particle shape was determined by minimizing an integral representing boundary area with the equation of a catenoid over the region extending from the particle/boundary junction to the curve defining the locus of points where catenoid surface met the original boundary plane tangentially. This outer curve was defined so as to build the boundary with those catenoid surfaces adding the minimum area [57].

The configurations calculated by Lee and Aaronson show that the heterogeneous nucleation barrier for a particle with a single facet ($\Delta G^*_{\mathrm{HET}}(\mathcal{W}^{1-\mathrm{facet}})$) can exceed that of an unfaceted nucleus ($\Delta G^*_{\mathrm{HET}}(\mathcal{W}^{\mathrm{sphere}})$) under identical conditions

when the curved portions of the nuclei are, in each case, described by the same isotropic interfacial free energy density.

In Ch. 9.4, an analysis using numerical methods developed in Ch. 6.1–6.4 that approximate an equilibrium solution by stepping through solutions for lesser anisotropy (where the symmetric difference between solutions can be considered negligible) agree that for cases where the difference between the interfacial free energy densities of the isotropic particle interface and the facet is small, the lenticular particles have the smaller nucleation barrier, $\Delta G^{*}_{\mathrm{HET}}(\mathcal{W}^{1-\mathrm{facet}}) > \Delta G^{*}_{\mathrm{HET}}(\mathcal{W}^{\mathrm{sphere}})$. Thus, results show that, although the interfacial free energy density of a facet orientation may be less than $\gamma(\mathcal{W}^{\mathrm{sphere}})$, faceting may be suppressed (lenticular particles form) if the necessary boundary distortion produces a relatively large amount of boundary energy.

9.4 Extension of Previous Work

9.4.1 Nucleation Barrier Contour Maps

The results from this work plotted in Fig. 9.4 apply to the heterogeneous nucleation of particles with a single facet at a boundary that is isotropic in $\hat{\mathbf{n}}_{\mathrm{B}}$. The *y*–axis of the plot gives the ratio $\Delta G_{\mathrm{HET}}(\mathcal{W}^{1-\mathrm{facet}})/\Delta G_{\mathrm{HET}}(\mathcal{W}^{\mathrm{sphere}})$ that compares the change in free energy on forming a volume of faceted nucleus relative to that of an isotropic nucleus of fixed dihedral angle at the same boundary.

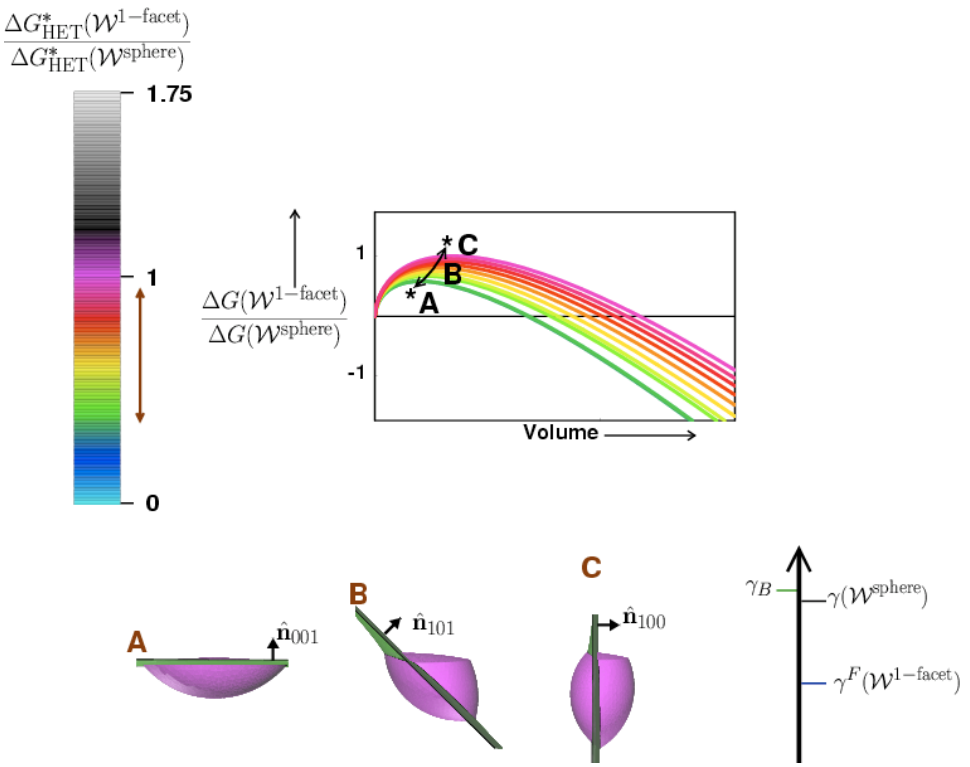

Figure 9.4: Changes in free energy for the nucleation of a particle with a single facet relative to a lens of dihedral angle $2\theta = 115.32°$. The facet free energy is $\gamma^F(\mathcal{W}^{1-\mathrm{facet}}) = 0.5\gamma(\mathcal{W}^{\mathrm{sphere}})$, where $\gamma(\mathcal{W}^{\mathrm{sphere}})$ describes the isotropic curved particle interface, and the boundary free energy is $\gamma_B = 1.07\gamma(\mathcal{W}^{\mathrm{sphere}})$. The trajectory of nucleation barriers is traced in the plot. Color is applied according to the color bar shown at right to indicate the relative heterogeneous nucleation barrier. Calculated configurations giving barriers of A, B, and C are shown below the plot. The barrier decreases as $\|\hat{\mathbf{n}}_B \cdot \hat{\mathbf{n}}_{\mathrm{facet}}\| \to 1$.

The chemical driving force, ΔG_V, and interfacial free energy densities retain the same value between curves. Appendix C.1 shows that, when ΔG_V is the same for all shapes, the free energy ratio (the *y*–axis of the plot) is independent of ΔG_V at the critical nucleus volume. The boundary and facet are described by $\gamma_{\mathrm{B}} = 1.07\gamma(\mathcal{W}^{\mathrm{sphere}})$ and $\gamma^F(\mathcal{W}^{1-\mathrm{facet}}) = 0.5\gamma(\mathcal{W}^{\mathrm{sphere}})$, respectively, meaning that the change in free energy for forming a faceted particle is reported relative to that on forming the lens of dihedral angle $2\theta = 115.32^\circ$ that follows from $\gamma_{\mathrm{B}}/\gamma(\mathcal{W}^{\mathrm{sphere}}) = 1.07$. These relative interfacial values were used in Lee and Aaronsan's study [57] and are used here for a comparison with their results.

The curves in the figure are parameterized by the orientation of $\hat{\mathbf{n}}_{\mathrm{B}}$ relative to the particle facet orientation ($\hat{\mathbf{n}}_{\mathrm{facet}}$), which is fixed at $\langle 001 \rangle$ with respect to the C_1 crystal axes. The change in free energy with the nucleation of a faceted particle varies with $\hat{\mathbf{n}}_{\mathrm{B}}$ because, in general, the proportion of each type of interface created is dependent on geometrical constraints imposed by the boundary orientation.

A particle nucleating at $\hat{\mathbf{n}}_{\mathrm{B}}$ must overcome a heterogeneous nucleation barrier to grow. In Fig. 9.4,

$$\Delta G^*_{\mathrm{HET}}(\mathcal{W}^{1-\mathrm{facet}}/\mathcal{W}^{\mathrm{sphere}}) = \Delta G^*_{\mathrm{HET}}(\mathcal{W}^{1-\mathrm{facet}})/\Delta G^*_{\mathrm{HET}}(\mathcal{W}^{\mathrm{sphere}})$$

which denotes the heterogeneous nucleation barrier of the faceted particle relative to a lens with a dihedral angle of 115.32° is traced with an arrow. Barrier height decreases with the smallest angle between $\hat{\mathbf{n}}_{\mathrm{B}}$ and $\hat{\mathbf{n}}_{\mathrm{facet}}$. The trace shows that the critical volume (*x*–axis) decreases with relative barrier height. This is expected because critical volume scales with the interfacial free energy density (see Appendix C.2) that describes the total change in interfacial free energy for the total change in area. Here, this effective density accounts for changes to boundary shape and increases with boundary rumpling for a fixed γ_{B} and $\gamma^F(\mathcal{W}^{1-\mathrm{facet}})$.

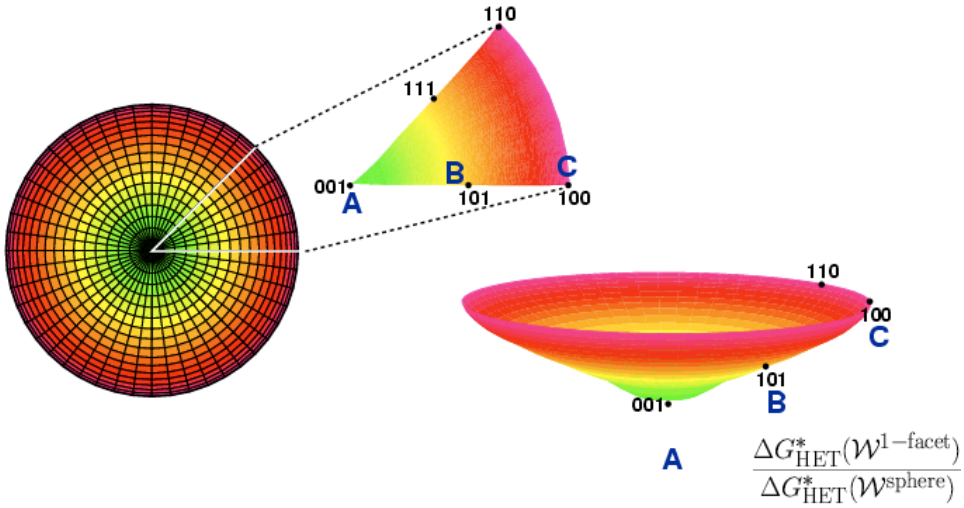

Figure 9.5: Stereographic projections of the relative heterogeneous nucleation barrier with $\hat{\mathbf{n}}_{\mathrm{B}}$ for the boundary particle in Fig. 9.4. (a) The center of the projection corresponds to the configuration where $\hat{\mathbf{n}}_{\mathrm{B}} \parallel \hat{\mathbf{n}}_{\mathrm{facet}}$ (configuration A in Fig. 9.4), and the perimeter corresponds to $\hat{\mathbf{n}}_{\mathrm{B}} \perp \hat{\mathbf{n}}_{\mathrm{facet}}$ (configuration C). The projections use the color bar in Fig. 9.4 to indicate the relative barrier at a given $\hat{\mathbf{n}}_{\mathrm{B}}$. (b) For convenience, the projection is given depth so that its height at any boundary orientation is proportional to $\Delta G^*_{\mathrm{HET}}(\mathcal{W}^{1-\mathrm{facet}})$. The facet orientation is fixed at $\hat{\mathbf{n}}_{\mathrm{facet}} = \langle 001 \rangle$. If a $(00\bar{1})$ particle facet forms when the sense of $\hat{\mathbf{n}}_{\mathrm{B}}$ is reversed, $(hk0)$ is a mirror plane.

When all orientations necessary for constructing an equilibrium particle shape are known and fixed relative to grain C_1, the effect of boundary orientation on barrier height can be mapped with a stereographic projection. The projections in Fig. 9.5 use color and depth to indicate the relative barrier height. Unless stated otherwise, stereographic projections that represent the value of a function parameterized by boundary orientation take the C_1 (001) orientation as the origin.

9.4.2 Particles with a Single Facet

For boundary particles with a single facet, the stereographic projection of the relative heterogeneous nucleation barrier is symmetric about the origin when $\hat{\mathbf{n}}_{\text{facet}}$ is fixed parallel to the $\langle 001 \rangle$ axis of C_1. This is demonstrated with the projection in Fig. 9.5, where $\hat{\mathbf{n}}_{\text{facet}} = \langle 001 \rangle$. The full plot is drawn to show the symmetry.

The stereographic projection in Fig. 9.5 is symmetric about the origin because $\Delta G^*_{\text{HET}}(\mathcal{W}^{1-\text{facet}}/\mathcal{W}^{\text{sphere}})$ is a function of one variable—the angle between $\hat{\mathbf{n}}_{\text{B}}$ and $\hat{\mathbf{n}}_{\text{facet}}$. The equator of the projection in Fig. 9.5 is defined by the locus of $\hat{\mathbf{n}}_{\text{B}}$ orthogonal to $\hat{\mathbf{n}}_{\text{facet}}$, and the center corresponds to $\hat{\mathbf{n}}_{\text{B}}$ parallel to $\hat{\mathbf{n}}_{\text{facet}}$. Points between the origin and perimeter correspond to boundary orientations between (001) correspond to boundary orientations between (001) and the $(hk0)$–type orientations. Barrier height increases as $\hat{\mathbf{n}}_{\text{B}}$ is rotated from the center to equator because facet-boundary intersections: (1) reduce the amount of low energy facet that a boundary particle contains, and (2) increase the amount of boundary ruffling. Meridians (paths along the diameter) correspond to gradients in barrier height with respect to $\hat{\mathbf{n}}_{\text{B}}$.

Figure 9.5 shows that the greatest reduction in the barrier occurs when $\hat{\mathbf{n}}_{\text{B}} \parallel \hat{\mathbf{n}}_{\text{facet}}$, supporting the results of [57]. The range of barrier heights calculated in this thesis is approximately $0.33 \leq \Delta G^*_{\text{HET}}(\mathcal{W}^{1-\text{facet}}/\mathcal{W}^{\text{sphere}}) \leq 0.95$. This range is close to that of [57], which gave a minimum of (roughly) 0.44 and a maximum > 1 for this example.

9.4.3 Boundary Particles that are Faceted in One Grain

When the interfacial particle is completely faceted to one side of the boundary, the projection is no longer symmetric about the origin but follows the point group

symmetry of the faceted portion of the particle.

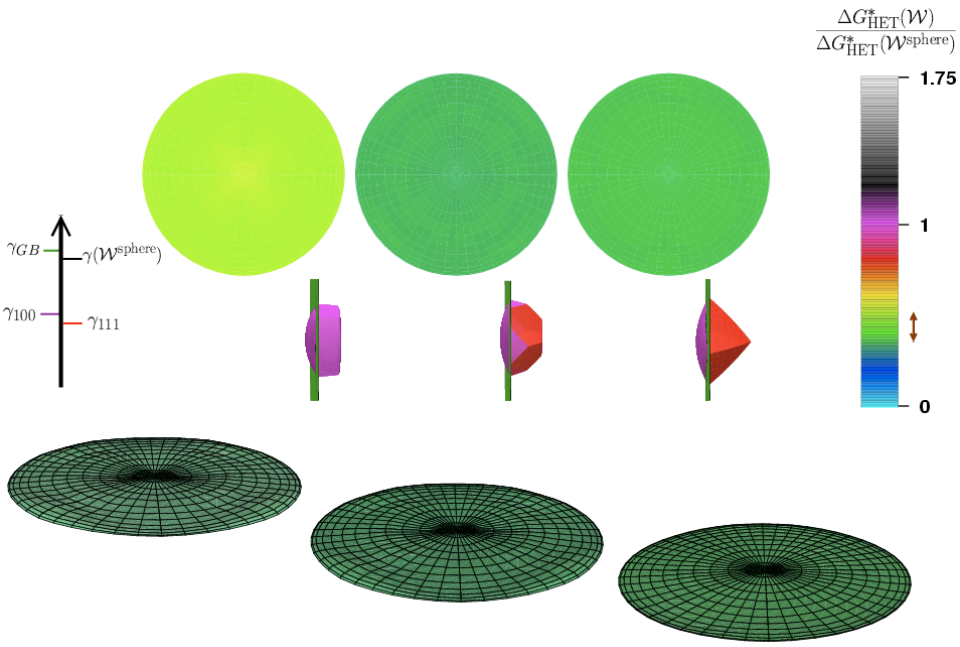

Figure 9.6: Stereographic projections of the nucleation barrier of a particle that is faceted to one side of the a boundary relative to an unfaceted particle attached to the same boundary. Points on the projections correspond to different inclinations of $\hat{\mathbf{n}}_{\mathrm{B}}$ relative to the $\langle 001 \rangle$ direction of the C_1 crystal axes, where $\hat{\mathbf{n}}_{\mathrm{B}} \parallel \langle 001 \rangle$ at the centers and $\hat{\mathbf{n}}_{\mathrm{B}} \perp \langle 001 \rangle$ along the perimeters. Although only $1/24$ of each plot is necessary, full plots are shown to reveal the 4–fold rotational symmetry about (001) boundary orientations. The plots show that heterogeneous nucleation of $\mathcal{W}^{\mathrm{cube}}_{\mathrm{sphere}}$ is smallest when particle interface is parallel to the boundary. The nucleation barrier is lower for $\mathcal{W}^{\mathrm{Toct}}_{\mathrm{sphere}}$ and $\mathcal{W}^{\mathrm{oct}}_{\mathrm{sphere}}$ for all boundary orientations. In all three cases, the barrier is greatly reduced from that of a fully lenticular particle.

Examples shown in this section are faceted on one side of the boundary and isotropic on the other. They are formed by the abutment of a polyhedral $\mathcal{W}$ to a $\mathcal{W}^{\text{sphere}}$ displaced as in Ch. 5.3–5.4 but by an amount determined numerically that accounts for the boundary energy due to rumpling. The Wulff polyhedra in the examples correspond to a cube ($\mathcal{W}^{\text{cube}}$), an octahedron ($\mathcal{W}^{\text{oct}}$), and a truncated octahedron ($\mathcal{W}^{\text{Toct}}$), giving stereographic projections of cubic symmetry. These polyhedral $\mathcal{W}$ were chosen because they are simple structures that are frequently observed [11, 34, 36, 39, 44, 49, 50, 91, 105]. For each of the examples, the polyhedral $\mathcal{W}$ are oriented so as to align one four-fold rotation axis with (001). As a result, the stereographic projections have four-fold rotational symmetry.

Distortions to the boundary can increase with the number of particle facets and edges intersecting the boundary and are dependent on the geometry of the intersection. Nevertheless, shapes constructed using the polyhedral $\mathcal{W}$ above can reduce the nucleation barrier relative to particles with a single facet. This is demonstrated in Chs. 9.4.3–9.4.5, where $\gamma^F(\mathcal{W}^{1-\text{facet}})$ describing the single facet (of the single-faceted particle) has the same value as γ_{111} describing the $\{111\}$ orientations that appear on $\mathcal{W}^{\text{oct}}$ and $\mathcal{W}^{\text{Toct}}$. The reduction occurs because the complete replacement of curved particle interface (described by the same constant $\gamma(\mathcal{W}^{\text{sphere}})$) with low energy facets to one side of the boundary gives a negative change in free energy greater than the positive change accompanying boundary distortion.

Relative facet free energy densities were chosen so that $\gamma_{100} = 1.15\gamma_{111}$, giving the truncated octahedral particle an aspect ratio of 1.15 to predict the behavior of boundary particles in dilute Pb–Al systems (Ch. 8). The value of $\gamma(\mathcal{W}^{\text{sphere}})$ was chosen to allow a comparison with results in Ch. 9.4.2, which applied the relative interfacial free energy densities used by Lee and Aaronson [56]. Faceting does not reduce the nucleation barrier relative to isotropic boundary particles described by $\gamma(\mathcal{W}^{\text{sphere}})$ that are sufficiently low—*i.e.*, $\Delta G_{\text{HET}}(\mathcal{W})/\Delta G_{\text{HET}}(\mathcal{W}^{\text{sphere}}) < 1$ only for isotropic boundary particles with dihedral angles of $2\theta > 2\theta_L$, where $2\theta_L$ denotes a lower bound. The examples in this thesis give results for specific $\gamma(\mathcal{W}^{\text{sphere}})$, and it is noted that reductions in interfacial free energy that accompany faceting do not occur relative to those isotropic particles of dihedral angles $2\theta < 2\theta_L$.

The projections in Fig. 9.5–9.6 show the relative barrier at $\hat{\mathbf{n}}_{\text{B}} \parallel \langle 001 \rangle$ to vary

(on average) as

$$\Delta G^*_{\rm HET}(\mathcal{W}^{\rm oct}_{\rm sphere}) \sim \Delta G^*_{\rm HET}(\mathcal{W}^{\rm Toct}_{\rm sphere}) < \Delta G^*_{\rm HET}(\mathcal{W}^{\rm cube}_{\rm sphere}) < \Delta G^*_{\rm HET}(\mathcal{W}^{\rm 1-facet}_{\rm sphere})$$

where the subscript denotes the $\mathcal{W}$ shape in C_2 and the superscript denotes that in C_1. For all $\hat{\mathbf{n}}_{\rm B}$, the polyhedral $\mathcal{W}$ produce $\Delta G^*_{\rm HET}(\mathcal{W}/\mathcal{W}^{\rm sphere}) \leq 0.53$. The $\mathcal{W}^{\rm oct}_{\rm sphere}$ and $\mathcal{W}^{\rm Toct}_{\rm sphere}$ boundary shapes give similar barrier reductions at an arbitrary $\hat{\mathbf{n}}_{\rm B}$ and are more easily nucleated than shapes with a single facet (Ch. 9.4.2) at all boundary orientations. Conversely, single-faceted shapes are more easily nucleated than $\mathcal{W}^{\rm cube}_{\rm sphere}$ at orientations within an arc distance of $\sim 20^\circ$ of the (001) boundary orientation.

Boundary orientations giving extrema in the relative heterogeneous nucleation barrier can differ for different $\mathcal{W}$. Orientations giving the lowest $\Delta G^*_{\rm HET}(\mathcal{W}^{\rm oct}_{\rm sphere})$ are nearly coincident with those that give the largest for $\Delta G^*_{\rm HET}(\mathcal{W}^{\rm cube}_{\rm sphere})$, and vice-versa. There is less of a dependence of $\Delta G^*_{\rm HET}(\mathcal{W}^{\rm Toct}_{\rm sphere})$ on $\hat{\mathbf{n}}_{\rm B}$ because: (1) $\mathcal{W}^{\rm Toct}_{\rm sphere}$ is effectively a combination of $\mathcal{W}^{\rm cube}_{\rm sphere}$ and $\mathcal{W}^{\rm oct}_{\rm sphere}$, which give low energy configurations at different orientations, and (2) the truncated octahedral $\mathcal{W}$ creates the least total interfacial free energy for a fixed volume (Appendix E).

9.4.4 Boundary Particles that are Faceted in Two Grains

When a boundary particle is faceted on both sides of a boundary, the variation in barrier height is again anisotropic in $\hat{\mathbf{n}}_{\rm B}$. For this example, the boundary is a *grain boundary* with a fixed crystallographic misorientation of $\vec{\mathbf{R}}_\Phi = 45^\circ\langle 001\rangle$. Hence, $\mathcal{W}^{\rm cube}_{\rm cube}$ is constructed by the abutment of two identical $\mathcal{W}^{\rm cube}$ misoriented from one another by 45° about $\langle 001\rangle$.

Because the boundary is isotropic in $\hat{\mathbf{n}}_{\rm B}$ and joins $\mathcal{W}$ with four-fold rotation axes parallel to $\langle 001\rangle$, this particular $\vec{\mathbf{R}}_\Phi$ yields stereographic projections with eight-fold rotation axes along (001), a result that is expected from rigorous arguments in [107]. If this example were realized as a spherical grain of fixed volume—large enough that the boundary is flat in the proximity of an attached particle—embedded in another grain of the same phase, equivalent nucleation sites would be separated by $\pi/4$ along any arc of boundary orientations a fixed distance from (001). For instance, interfacial particles at (100) boundaries imaged along

$[100]$ are identical to those at (110) imaged along $[\overline{1}10]$.

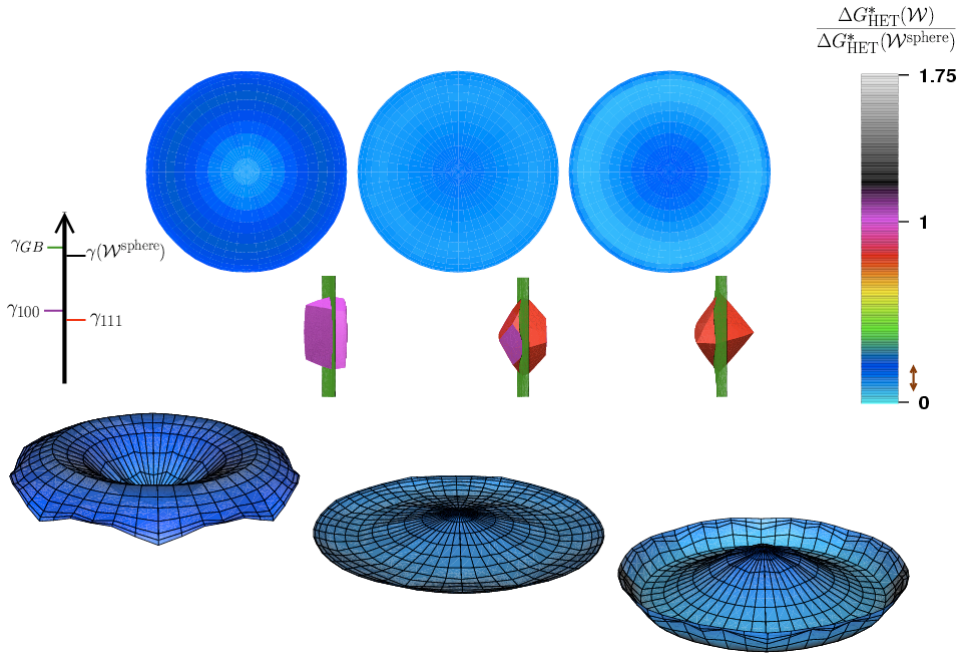

Figure 9.7: Due to the eight-fold rotational symmetry about (001) that results for the fully faceted particles attached to pure 45° twist boundaries, only $1/16$ of the projections are necessary. However, the full plots are shown to reveal the symmetry. As before, reductions in $\Delta G^*_{\mathrm{HET}}$ are largest for particles derived from $\mathcal{W}^{\mathrm{Toct}}$ and $\mathcal{W}^{\mathrm{oct}}$.

The lowest nucleation barrier for particles formed by $\mathcal{W}^{\text{cube}}_{\text{cube}}$ occurs at the pure 45° twist boundary ($\hat{\mathbf{n}}_{\text{GB}} \parallel [001]$ or $[00\bar{1}]$) because, as discussed in Ch. 11.2.1, $\mathcal{W}^{\text{cube}}_{\text{cube}}$ takes a Winterbottom shape. The twist boundary gives the largest nucleation barrier for particles formed by $\mathcal{W}^{\text{oct}}_{\text{oct}}$ and $\mathcal{W}^{\text{Toct}}_{\text{Toct}}$ because these boundary particles necessitate large boundary distortions and have larger (surface area)/(volume) ratios at the twist boundary than at other $\hat{\mathbf{n}}_{\text{B}}$. For the $\mathcal{W}^{\text{oct}}_{\text{oct}}$ and $\mathcal{W}^{\text{Toct}}_{\text{Toct}}$ particles, the nucleation barrier is minimized at boundaries of mixed character where one octahedral face is approximately parallel to the boundary ($\hat{\mathbf{n}}_{\text{GB}} \parallel \langle 111 \rangle$).

To illustrate the significance of these results, consider $\mathcal{W}^{\text{oct}}_{\text{oct}}$. The reduction in energy on nucleating $\mathcal{W}^{\text{oct}}_{\text{oct}}$ at $\hat{\mathbf{n}}_{\text{GB}} \parallel \langle 111 \rangle$ could effectively stabilize $\{111\}$ boundary orientations: If all boundary orientations of the embedded spherical grain were available as nucleation sites, the nuclei would accumulate at $\{111\}$ boundary orientations and act as pinning centers limiting changes to boundary position and orientation that could occur if one grain were to coarsen. If all boundary orientations of the spherical grain were uniformly decorated with $\mathcal{W}^{\text{oct}}_{\text{oct}}$, $\{111\}$ boundary orientations would have a lower total interfacial free energy, suggesting that the spherical grain would tend to increase $\{111\}$ boundary (*e.g.*, through grain boundary diffusion) to achieve an octahedral "decorated" grain boundary $\mathcal{W}$. This idea is further discussed in Ch. 11.2.2.

Each orientation on the stereographic projection maps to a particle that is completely defined with facet energy densities slightly greater than $0.5\gamma_{\text{GB}}$ (Ch. 9.4.1). As a result, $\Delta G^{*}_{\text{HET}}(\mathcal{W}/\mathcal{W}^{\text{sphere}})$ at a given boundary orientation is reduced from particles that are faceted within one grain only (Ch. 9.4.3), even though boundary particles are faceted to both sides of the boundary may require greater boundary rumpling. The maximum barrier for the fully faceted particles occurs for $\Delta G^{*}_{\text{HET}}(\mathcal{W}^{\text{cube}}_{\text{cube}}/\mathcal{W}^{\text{sphere}}) = 0.24$ and the minimum for $\Delta G^{*}_{\text{HET}}(\mathcal{W}^{\text{Toct}}_{\text{Toct}}/\mathcal{W}^{\text{sphere}}) = 0.07$. The relative barrier heights are shown in Fig. 9.7.

9.4.5 Effect of Relative Interfacial Free Energies

Unfaceted shapes may nucleate more easily than faceted ones if the reduction in energy on forming facets does not compensate for the increase in energy that occurs when facets rumple the boundary. To illustrate, this section considers relative facet

free energies that are larger than those in Ch. 9.4.1–9.4.4: $\gamma_{111} = 0.7\gamma(\mathcal{W}^{\text{sphere}})$ for fixed $\gamma_{100}/\gamma_{111} = 1.15$ and $\gamma_{\text{B}} = 1.07\gamma(\mathcal{W}^{\text{sphere}})$. Hence, the difference between the interfacial free energy of the isotropic particle interface and the lowest energy facets, $\Delta\gamma_{\text{B}-\text{P}}$, is reduced.

The stereographic projection of relative barrier heights that results for the original single-facet case at this larger facet energy density is shown in Fig. 9.8. As in Ch. 9.4.2, the barrier increases as $\hat{\mathbf{n}}_{\text{facet}} \cdot \hat{\mathbf{n}}_{\text{B}} \rightarrow 0$. An expected result from the intersected $\mathcal{W}$ geometry (Ch. 5.3), faceting produces a constant barrier reduction (*i.e.*, no boundary-facet intersection) for $\|\hat{\mathbf{n}}_{\text{facet}} \cdot \hat{\mathbf{n}}_{\text{B}}\| \leq \cos(12^\circ)$.

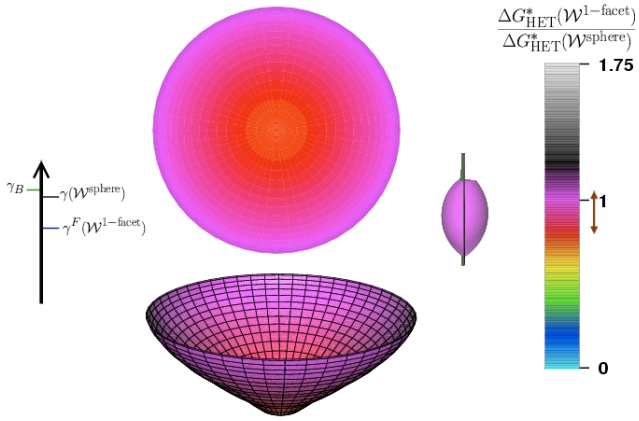

Figure 9.8: Results for a particle with a single facet (plotted as in Fig. 9.5) shows that boundary distortion can inhibit the nucleation of faceted particles at boundary orientations of $70^\circ < \cos^{-1}(\hat{\mathbf{n}}_{\text{facet}} \cdot \hat{\mathbf{n}}_{\text{B}}) \leq 90^\circ$ for larger facet free energy densities. The boundary particle configuration shown below the projection is metastable relative to a lenticular shape of $\gamma(\mathcal{W}^{\text{sphere}})$.

Calculated results indicate that, for this larger set of interfacial free energy densities, faceting becomes an ineffective means of reducing $\Delta G^*_{\mathrm{HET}}$ relative to the isotropic (lenticular) shape for $\gamma(\mathcal{W}^{\mathrm{sphere}})$ at $\|\hat{\mathbf{n}}_{\mathrm{facet}} \cdot \hat{\mathbf{n}}_{\mathrm{B}}\| \approx \cos(70^\circ)$. Hence, the lenticular shapes are predicted to nucleate more easily for a range of orientations extending to the equator of the stereographic projection. The range predicted here, $70^\circ < \cos^{-1}(\hat{\mathbf{n}}_{\mathrm{facet}} \cdot \hat{\mathbf{n}}_{\mathrm{B}}) \leq 90^\circ$ is slightly smaller than that from previous work [57], which calculates a lower limit of 65°. This discrepancy is due to an overestimation of the increase in boundary area with the geometric approximation of [57, 60].

For the shapes that are faceted to one side (or both sides) of the boundary, reducing $\Delta\gamma_{\mathrm{B-P}}$ increases both the values and spread in values of $\Delta G^*_{\mathrm{HET}}(\mathcal{W}/\mathcal{W}^{\mathrm{sphere}})$ for a given polyhedral $\mathcal{W}$. Because faceting becomes less favorable as $\Delta\gamma_{\mathrm{B-P}}$ is reduced the calculated geometries tend to produce shapes that (1) have a smaller (surface area)/(volume) ratio and (2) do not replace as much boundary, reducing the total boundary rumpling by decreasing the triple junction line length. Lenticular boundary particle shapes of $2\theta = 115.32^\circ$ are again preferred to $\mathcal{W}^{\mathrm{cube}}_{\mathrm{sphere}}$ for orientations near $\{001\}$.

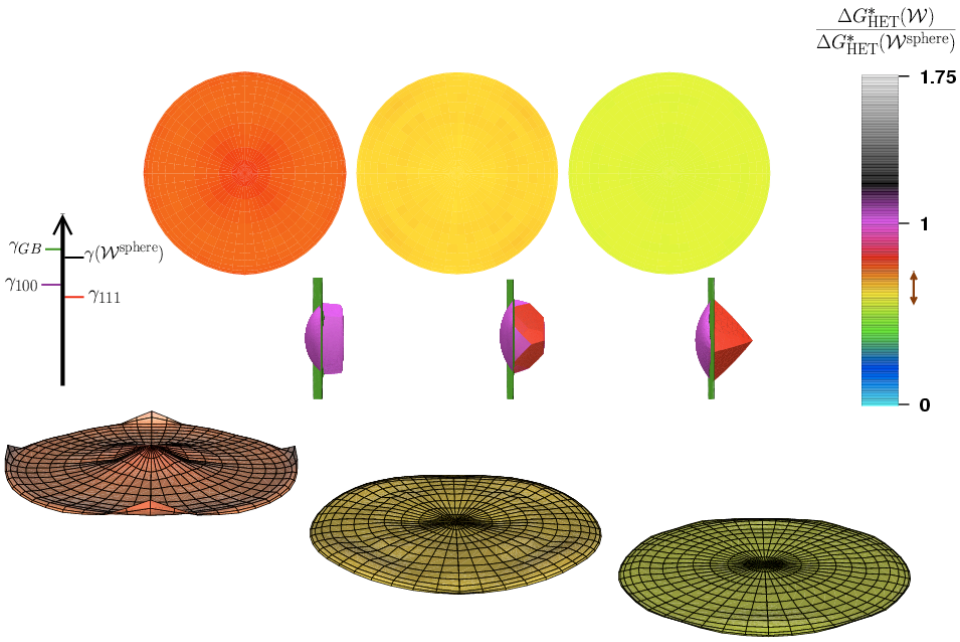

Figure 9.9: As in Fig. 9.8, faceting produces less of a reduction in ΔG^* at larger facet energy densities. In this case, however, the lenticular particles are not favored over the shapes that are fully faceted in one grain at any boundary orientation.

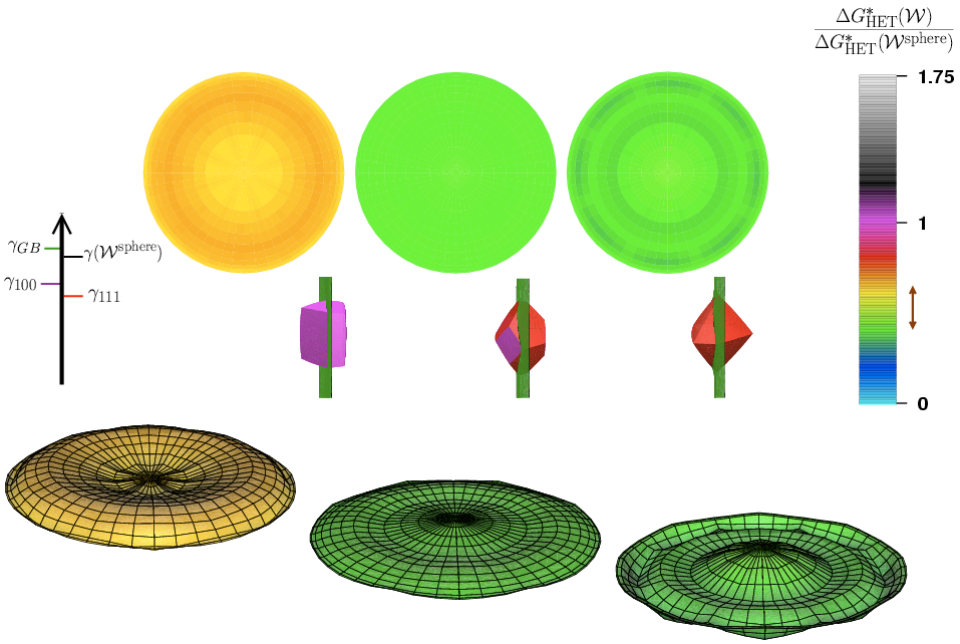

Figure 9.10: As in Fig. 9.9 but for fully faceted particles.

The the spread in $\Delta G^*_{\text{HET}}(\mathcal{W}/\mathcal{W}^{\text{sphere}})$ values indicates the nucleation barrier's dependence on $\hat{\mathbf{n}}_{\text{B}}$ and thus the spread in nuclei populations with boundary orientation. In this case, the largest spread occurs for particles formed with $\mathcal{W}^{\text{cube}}$, which have a lower ΔG^*_{HET} and will thus be more concentrated at orientations where boundary particles derived from $\mathcal{W}^{\text{oct}}$ and $\mathcal{W}^{\text{Toct}}$ are more difficult to nucleate.

Because boundary particles derived from $\mathcal{W}^{\text{cube}}$ will be more concentrated at particular boundary orientations, they may have a more significant impact on the stability of a given boundary orientation than the particles containing $\{111\}$ facet orientations, which give the smallest spread in $\Delta G^*_{\text{HET}}(\mathcal{W}/\mathcal{W}^{\text{sphere}})$ at all boundary orientations and for both $\Delta\gamma_{\text{B-P}}$. Here, it is speculated that if the aspect ratio of a truncated octahedral particle, $\gamma_{100}/\gamma_{111}$, were larger, changes to particle-mediated boundary stability would be largest for particles formed by portions of $\mathcal{W}^{\text{cube}}_{\text{cube}}$ but relatively unchanged for those formed by portions of $\mathcal{W}^{\text{Toct}}_{\text{Toct}}$ because the size of the $\{100\}$ orientations would be reduced in proportion to the relative increase in γ_{100} for truncated octahedra.

9.4.6 Triple Junction Particles that are Faceted in One Grain

Calculated results are shown in Fig. 9.11 for the nucleation of a particle at a triple junction joining isotropic boundaries. The particle is described by $\gamma(\mathcal{W}^{\text{cube}})$ in grain C_1 and $\gamma(\mathcal{W}^{\text{sphere}})$ in the other two grains. The stereographic projection gives the nucleation barrier of the faceted particle at the triple junction relative to $\Delta G^*_{\text{HET}}(\mathcal{W}^{\text{sphere}})$, which describes the nucleation barrier for a lenticular particle with a dihedral angle of 115.32° attached to the triple junction. The projection is parameterized by the orientation of the grain embedding the polyhedral portion of the particle relative to the average boundary orientations, which are fixed by a global constraint.

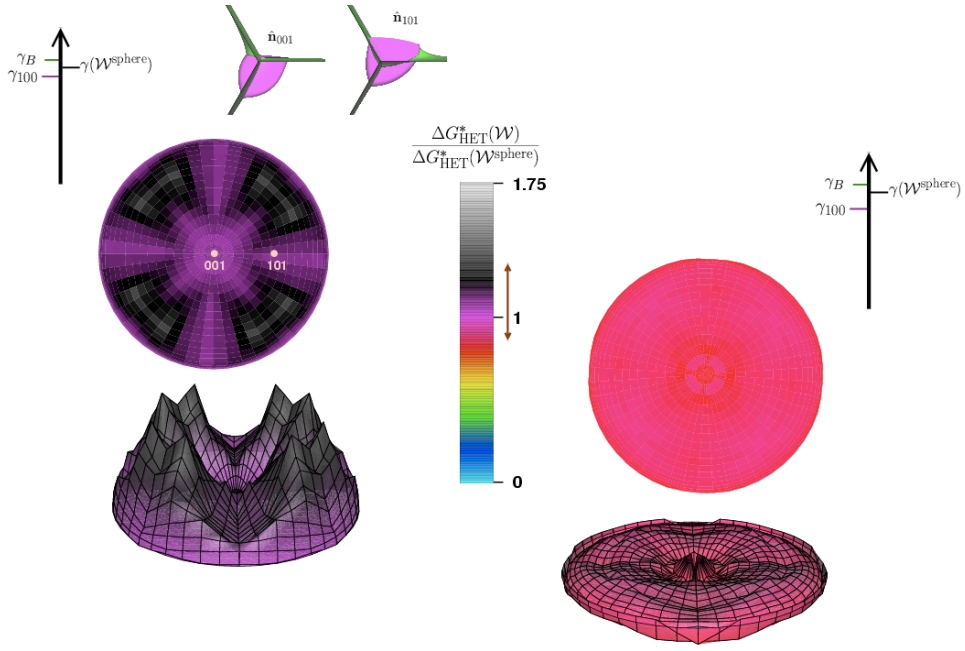

(a) (b)

Figure 9.11: Stereographic projections of the heterogeneous nucleation barrier of a particle that is attached to a triple junction joining three isotropic boundaries of equivalent energy. The triple junction particle forms a portion of a cube in one grain and portions of spheres in the other. Points on the projection correspond to orientations of the normal to one of the particle facets. As shown, the nucleation of an isotropic triple junction particle of $\gamma(\mathcal{W}^{\text{sphere}})$ is favored at larger facet energies.

For this example, the fixed average boundary normals fix the average triple junction line vector with respect to the crystal axes of a grain adjoining C_1, which is free to rotate. For simplicity, the orientations of C_1 are limited to $\vec{\mathbf{R}}_\Phi = \Phi\langle uv0\rangle$, constraining the rotation axis to lie in a single plane that coincides with the average orientation of one boundary terminating grain C_1. The stereographic projection of $\Delta G^*_{\mathrm{HET}}(\mathcal{W}^{\mathrm{cube}}_{\mathrm{sphere}}/\mathcal{W}^{\mathrm{sphere}})$ in Fig. 9.11 is thus a function of the orientation of one cube facet normal. The relative interfacial free energies generating the plot are $\gamma_{\mathrm{B}} = 1.07\gamma(\mathcal{W}^{\mathrm{sphere}})$ and $\gamma_{100} = 0.7\gamma(\mathcal{W}^{\mathrm{sphere}})$ in Fig. 9.11(a) and $\gamma_{100} = 0.9\gamma(\mathcal{W}^{\mathrm{sphere}})$ in Fig. 9.11(b). These values are similar to those used for boundary particles in Chs. 9.4.3–9.4.5, and $\Delta\gamma_{\mathrm{B-P}}$ was kept relatively small to avoid conditions of perfect wetting.

The stereographic projections of barrier heights that results for the triple junction particles share the four-fold rotational symmetry of the attached $\mathcal{W}^{\mathrm{cube}}$. Figure 9.11(b) shows boundary orientations to produce anisotropic boundary particle shapes giving $1.09 \leq \Delta G^*_{\mathrm{HET}}(\mathcal{W}^{\mathrm{cube}}_{\mathrm{sphere}}/\mathcal{W}^{\mathrm{sphere}}) \leq 1.36$—shapes unfavorable to the lenticular particle. Thus, if the grain embedding $\mathcal{W}^{\mathrm{cube}}$ were free to rotate about an axis in the plane defined by the (average) normal to one of its boundaries, without disrupting other elements of the triple junction geometry, no rotations could transform the triple junction into a site where this type of faceted nuclei would form in preference to the isotropic boundary particle. However, for smaller facet free energies (Fig. 9.11(a)), the isotropic boundary particles are less favorable to the faceted shapes. In a real microstructure, triple junctions joining relatively high energy boundaries separating grains for which the curved particle interface has a free energy density comparable to the boundaries would thus be more likely to yield faceted particle shapes. Both projections show the faceted nuclei to form most readily at orientations for which a particle facet lies in the plane of one of the boundaries forming the junction.

Heterogeneous nucleation for more complicated systems, *e.g.*, fully faceted particles at triple junctions that define boundaries and grains that are free to any possible rotation and the more simple case of a particle at a quadruple point for which the only free variable is a set of grain boundary energies constrained to be identical and isotropic, can be modeled by the methods of Chs. 6.2–6.4 but are beyond the scope of this thesis.

9.4.7 Summary of Results

1. Consistent with Neumann's principle [108], variations in the relative heterogeneous nucleation barrier reflect the point group symmetry of the boundary particle shape when the boundary is isotropic.
2. Boundary particle shapes containing portions of $\mathcal{W}$ giving smaller (interfacial free energy)/(volume) ratios tend to give smaller barrier heights for identical facet free energy densities at smaller $\Delta\gamma_{\mathrm{B-P}}$.
3. For a fixed $\vec{\mathbf{R}}_{\Phi}$, $\mathcal{W}$ and $\Delta\gamma_{\mathrm{B-P}}$ tend to have a greater effect on the barrier than $\hat{\mathbf{n}}_{\mathrm{B}}$.
4. Boundary particle shapes derived from a given set of oriented $\mathcal{W}$ show that variations in the heterogeneous nucleation barrier with $\hat{\mathbf{n}}_{\mathrm{B}}$ increase with a reduction in $\Delta\gamma_{\mathrm{B-P}}$.
5. The reduction in the heterogeneous nucleation barrier occurs only relative to those isotropic particles with dihedral angles greater than $2\theta_L$.
6. As $\Delta\gamma_{\mathrm{B-P}}$ is reduced, $2\theta_L$ increases, meaning that the faceting becomes a less effective means of reducing $\Delta G^*_{\mathrm{HET}}(\mathcal{W}/\mathcal{W}^{\mathrm{sphere}})$.
7. There are cases where faceting produces boundary particle configurations for which $\Delta G^*_{\mathrm{HET}}(\mathcal{W}/\mathcal{W}^{\mathrm{sphere}}) > 1$. For those cases, the heterogeneous nucleation of isotropic particles is more favorable.

9.5 Nucleation Rate

Nucleation rate is exponentially dependent on ΔG^* and therefore sensitive to the interfacial free energy—and thus the shape—of a nucleating particle. The time-independent (steady-state) nucleation rate for boundary particles is [109]

$$J^*_s = Z\beta^* N_{\mathrm{HET}} \exp\left(\frac{-\Delta G^*_{\mathrm{HET}}}{kT}\right) \tag{9.1}$$

where Z is the Zeldovich non-equilibrium factor that accounts for the dissolution of post-critical nuclei, β^* is the rate atoms attach to the critical nucleus, N_{HET} is the number of boundary sites per unit volume, and kT accounts for the thermal energy that disrupts the formation of critical nuclei.

At fixed temperature and N_{HET}, all variables in Eq. (9.1) are shape dependent. For small undercoolings, $15kT \leq \Delta G^*_{\text{HET}} \leq 60kT$, nucleation rate is controlled by the nucleation barrier [60, 109], ΔG^*_{HET} determines which nucleation configurations occur with the greatest frequency, and the results of Ch. 9.4 can be used to predict changes to a microstructure during nucleation.

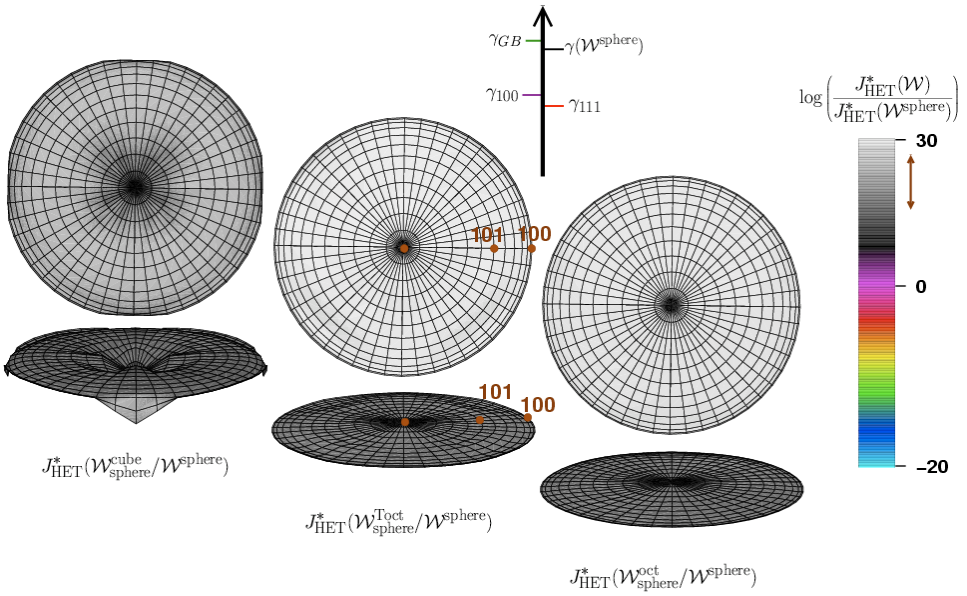

Figure 9.12: The stereographic projections showing relative values in the nucleation rate that apply to the particles faceted to one side of a boundary calculated in this section. As expected from the relative ΔG^*_{HET} trends of Chs. 9.4.3–9.4.4 for each shape, the nucleation rate varies most with $\hat{\mathbf{n}}_{\text{B}}$ and γ_{B} for the particle constructed from portions of $\mathcal{W}^{\text{cube}}$. The plot mesh is applied to render cases of large J^*_{HET} visible.

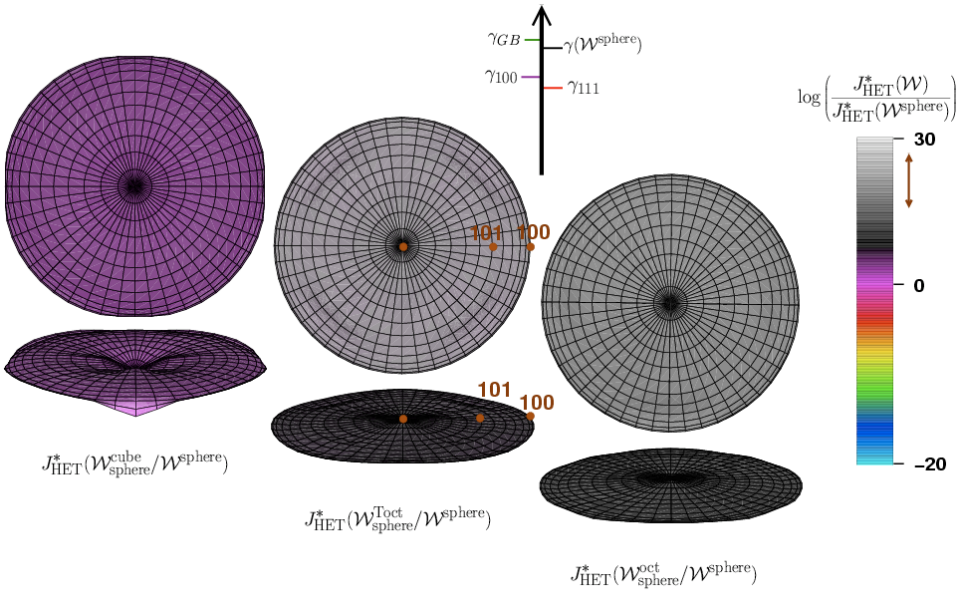

Figure 9.13: As in Fig. 9.12, but for smaller $\Delta\gamma_{\text{B}-\text{P}}$.

To illustrate the effect of particle faceting on nucleation rate, it is convenient to define $\Delta G^*_{\rm HET}(\mathcal{W}^{\rm sphere})$ in terms of kT. Following the example of [53] for homogeneous nucleation, $\Delta G^*_{\rm HET}(\mathcal{W}^{\rm sphere})$ is set to $60kT$, the largest barrier that can occur for T to be classified as a small undercooling [109] for lenticular shapes described by $\gamma(\mathcal{W}^{\rm sphere})$.

Shape	$J^*_{\rm HET}(\mathcal{W})/J^*_{\rm HET}(\mathcal{W}^{\rm sphere})$	
	$\gamma_{111}/\gamma(\mathcal{W}^{\rm sphere}) = 0.5$	$\gamma_{111}/\gamma(\mathcal{W}^{\rm sphere}) = 0.7$
$\mathcal{W}^{1-\rm facet}$	$10^2 - 10^{16}$	$10^{-1} - 10^6$
$\mathcal{W}^{\rm cube}_{\rm sphere}$	$10^{12} - 10^{14}$	$10^6 - 10^7$
$\mathcal{W}^{\rm oct}_{\rm sphere}$	10^{17}	10^{11}
$\mathcal{W}^{\rm Toct}_{\rm sphere}$	10^{17}	10^{10}
$\mathcal{W}^{\rm cube}_{\rm cube}$	$10^{20} - 10^{24}$	$10^9 - 10^{10}$
$\mathcal{W}^{\rm oct}_{\rm oct}$	$10^{22} - 10^{24}$	$10^{15} - 10^{16}$
$\mathcal{W}^{\rm Toct}_{\rm Toct}$	10^{23}	$10^{15} - 10^{16}$

Table 9.1: Variations in heterogeneous nucleation rate for particles defined by $\mathcal{W}$ relative to an isotropic particle when the homogeneous nucleation barrier for the isotropic particles is $60kT$. The relative nucleation rates depend strongly on the boundary particle shape, are largest for shapes formed with $\{111\}$ interface, and decrease as $\Delta\gamma_{\rm B-P}$ decreases, where $\Delta\gamma_{\rm B-P} = \gamma(\mathcal{W}^{\rm sphere}) - \gamma_{111}$, $\gamma_{100} = 1.15\gamma_{111}$, and $\gamma_{\rm B} = 1.07\gamma(\mathcal{W}^{\rm sphere})$.

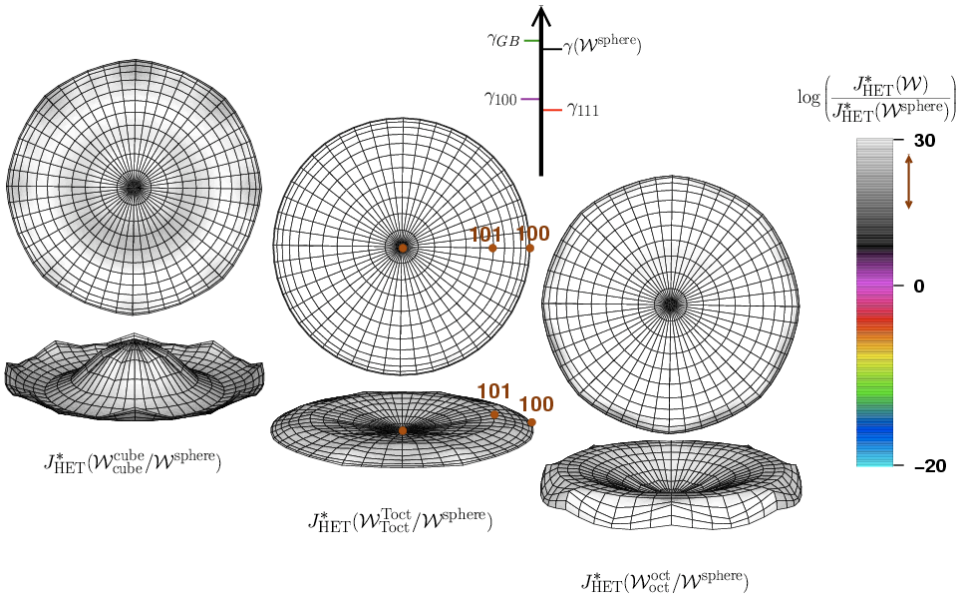

Figure 9.14: As in Fig. 9.14 but for particles faceted to both sides of a boundary.

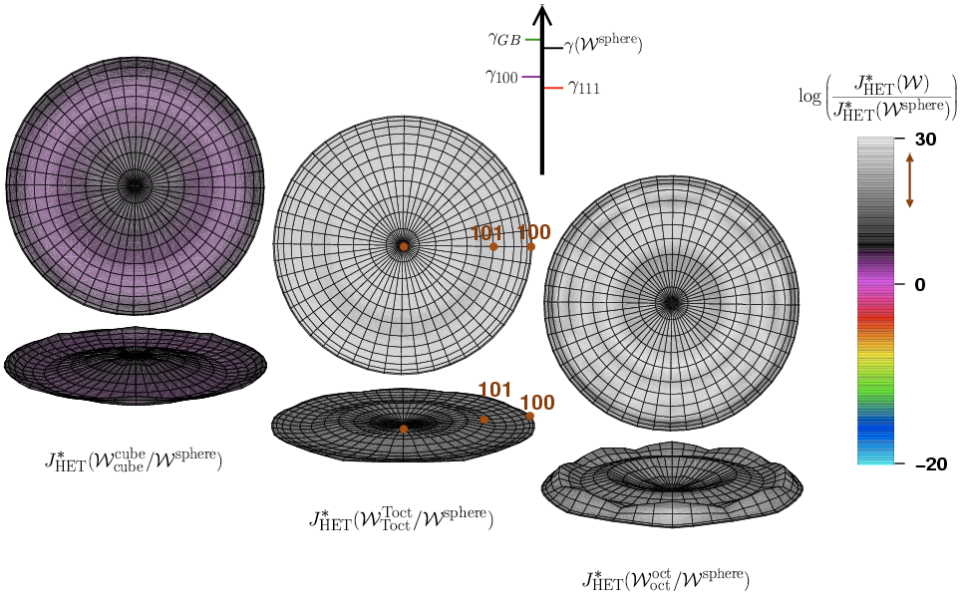

Figure 9.15: As in Fig. 9.15 but for particles faceted to both sides of a boundary.

Table 9.5 compares results from Ch. 9.4 for all $\hat{\mathbf{n}}_{\mathrm{B}}$ among the particles shown in Figs. 9.12–9.16. The results indicate that the nucleation rate is largest for particles where $\Delta\gamma_{\mathrm{B-P}}$ is larger (faceting is more favorable). The relative nucleation rate, $J^{*}_{\mathrm{HET}}(\mathcal{W}/\mathcal{W}^{\mathrm{sphere}})$, is nearly uniform with boundary orientation for boundary particle shapes formed from $\mathcal{W}^{\mathrm{oct}}$ and $\mathcal{W}^{\mathrm{Toct}}$. For boundary particles formed from $\mathcal{W}^{\mathrm{cube}}$, the dependence of $J^{*}_{\mathrm{HET}}(\mathcal{W}/\mathcal{W}^{\mathrm{sphere}})$ on $\hat{\mathbf{n}}_{\mathrm{B}}$ is more pronounced, a result expected from the more pronounced variation in $\Delta G^{*}_{\mathrm{HET}}(\mathcal{W}/\mathcal{W}^{\mathrm{sphere}})$ for $\mathcal{W}^{\mathrm{cube}}$ shown in Chs. 9.4.3–9.4.5.

Consider a system in which lenticular particles described by $\gamma(\mathcal{W}^{\mathrm{sphere}})$ are nucleating in addition to $\mathcal{W}^{\mathrm{cube}}_{\mathrm{cube}}$ and $\mathcal{W}^{\mathrm{cube}}_{\mathrm{sphere}}$ boundary particles. If every cubic centimeter of material nucleates one lenticular particle each second ($J^{*}_{\mathrm{HET}}(\mathcal{W}^{\mathrm{sphere}}) = 1$ nucleus$/cm^3 \cdot s$), it also nucleates $\sim 10^{20}$–10^{24} boundary particles that are fully faceted and $\sim 10^{12}$–10^{14} faceted boundary particles with spherical caps to one side of the boundary. An observation of one of these lenticular particles would be exceedingly rare in such a case.

Reducing $\Delta\gamma_{\mathrm{B-P}}$ decreases the relative nucleation rates of the faceted particles. For example, when $\gamma_{111} = 0.7\gamma(\mathcal{W}^{\mathrm{sphere}})$, J^{*}_{HET} drops several orders of magnitude for all anisotropic boundary particles. Decreasing $\Delta\gamma_{\mathrm{B-P}}$ has a larger impact on particles derived from $\mathcal{W}^{\mathrm{cube}}$ (Ch. 9.4.5) because $\gamma_{100} > \gamma_{111}$, the particles have larger (surface area)/(volume) ratios, and the particles cause a greater boundary distortion. For the example above, every cubic centimeter nucleates $\sim 10^{9} - 10^{10}$ boundary particles of $\mathcal{W}^{\mathrm{cube}}_{\mathrm{cube}}$ and $\sim 10^{6} - 10^{7}$ boundary particles of $\mathcal{W}^{\mathrm{cube}}_{\mathrm{sphere}}$ for each lenticular particle that nucleates. An observation of the lenticular particles would still be rare. As $\Delta\gamma_{\mathrm{B-P}}$ is further reduced, however, the lenticular particles would dominate during nucleation because the total interfacial free energy for a fixed volume would be minimized by a lenticular shape, which gives a smaller (surface area)/(volume) ratio than a particle with broad facets.

The effect of boundary orientation becomes more pronounced with an increase in $\Delta\gamma_{\mathrm{B-P}}$ for particles with a single facet. This result is in contrast with particles containing multiple facets. At the larger $\Delta\gamma_{\mathrm{B-P}}$, the relative nucleation rate for the single-facet particles decreases from $\sim 10^{16}$ to $\sim 10^{6}$ on rotating $\hat{\mathbf{n}}_{\mathrm{B}}$ away from the particle facet. On the other hand, at smaller $\Delta\gamma_{\mathrm{B-P}}$, the effect of $\hat{\mathbf{n}}_{\mathrm{B}}$ diminishes: for $\gamma_{111} = 0.7\gamma(\mathcal{W}^{\mathrm{sphere}})$, $J^{*}_{\mathrm{HET}}(\mathcal{W}/\mathcal{W}^{\mathrm{sphere}})$ decreases from $\sim 10^{2}$ to $\sim 10^{-1}$, and

approximately 10 lenticular particles nucleate for every particle with a (001) facet when $\hat{\mathbf{n}}_{\mathrm{GB}} \perp (001)$. However, at this smaller $\Delta\gamma_{\mathrm{B-P}}$, $\sim 10^6$ $\mathcal{W}^{\mathrm{cube}}_{\mathrm{sphere}}$ and $\sim 10^9$ $\mathcal{W}^{\mathrm{cube}}_{\mathrm{cube}}$ particles nucleate for every lenticular particle, and J^*_{HET} need not be controlled by the lenticular particles when the probability of single facet boundary particle nucleation is relatively low.

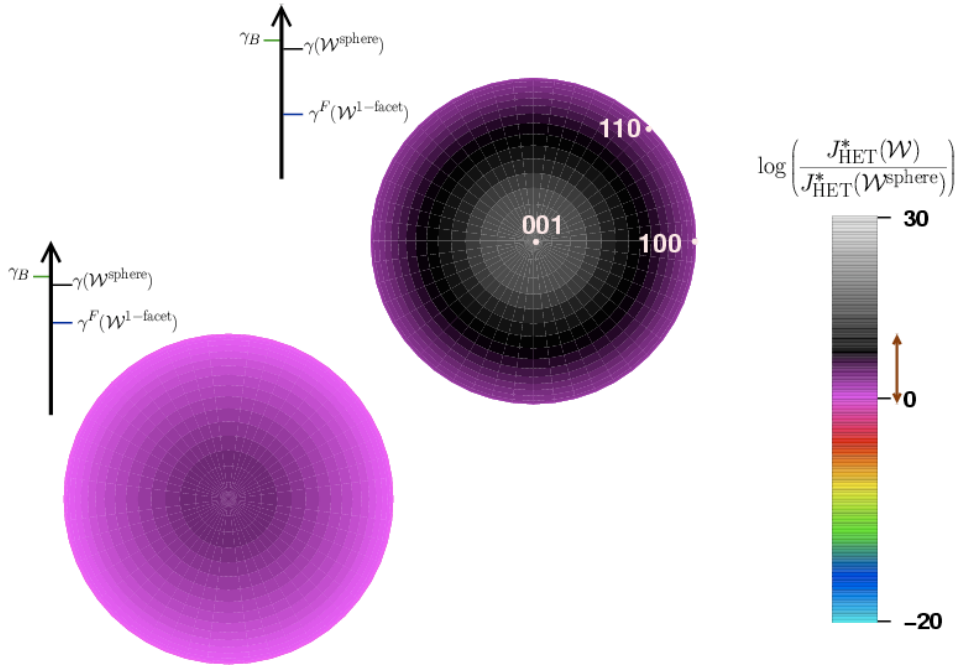

Figure 9.16: The relative nucleation rate for a boundary particle as a function of γ_{B} and $\hat{\mathbf{n}}_{\mathrm{B}}$. Although only a curve extending from (001) to, *e.g.*, (100) is necessary, one-eighth of the plot is shown. Orientations in the neighborhood of the perimeter of the plot give relatively low nucleation rates for the smaller $\Delta\gamma_{\mathrm{B-P}}$.

Results from this section show that the exponential dependence of nucleation rate on $\Delta G^{*}_{\mathrm{HET}}$ reflects the details of particle faceting. Nucleation rate is a strong function of both particle shape and the relative free energies of particle facets. Boundary orientation becomes increasingly important at larger facet free energies (smaller $\Delta\gamma_{\mathrm{B-P}}$) because the energy created on boundary rumpling is absorbed by the reduction in energy on forming broad facets of low energy. When $\Delta\gamma_{\mathrm{B-P}}$ is decreased, there is less of a driving force to produce particles with single facets at orientations giving the greatest boundary distortions because, for larger facet free energies, the shapes do not provide as much of an energy reduction as an isotropic (lenticular) shape. However, under such conditions, lenticular particles of fixed $\gamma(\mathcal{W}^{\mathrm{sphere}})$ can become metastable to boundary particles that retain multiple low energy facets.

Chapter 10

Anisotropic Grain Boundary Energies

Generally, grain boundary energy varies with the crystallographic misorientation across the boundary ($\vec{\mathbf{R}}_\Phi$) and the orientation of the boundary plane ($\hat{\mathbf{n}}_\mathrm{B}$) [13]. Specification of these variables at constant T and $\vec{\mu}$ determines the set of shapes a grain can take at equilibrium [26]. The following section briefly reviews the Read Shockley dislocation model for grain boundary energy that applies when $\Phi \leq 5-10^\circ$.

10.1 Brief Review of the Read Shockley Model for Low Angle Grain Boundary Energies

The Read Shockley model represents low angle grain boundaries as arrays of discrete, parallel, regularly-spaced dislocations. The model was introduced in a work [110] that combines observations for low angle tilt boundaries with calculations taking idealized dislocation geometry and measured material parameters to show its utility. Several studies have since demonstrated the model's applicability to a variety of low angle boundaries [111, 112].

The model gives the energy of a low angle tilt boundary for a primitive cubic

crystal structure with a misorientation $\vec{\mathbf{R}}_{\Phi} = \Phi\langle 001\rangle$ as

$$\gamma_{\mathrm{GB}}(\hat{\mathbf{n}}_{\mathrm{GB}}) = E_o(\hat{\mathbf{n}}_{\mathrm{GB}})\Phi\left[\, D(\hat{\mathbf{n}}_{\mathrm{GB}}) - \ln\Phi \,\right] \tag{10.1}$$

where $\hat{\mathbf{n}}_{\mathrm{GB}}$–dependent parameters $D(\hat{\mathbf{n}}_{\mathrm{GB}})$ and $E_o(\hat{\mathbf{n}}_{\mathrm{GB}})$ are, respectively, a constant dependent on the dislocation core energy and a constant dependent on the elastic properties of the material. Equation (10.1) models pure tilt boundaries as arrays of edge dislocations, pure twist boundaries as arrays of screw dislocations, and general boundaries as a combination of edge and screw dislocations.

Equation (10.1) is derived for strain energies calculated with linear isotropic elasticity theory. Dislocation cores are regions where the displacement between two atoms on adjacent sites (atomic deregistry) is too large for elasticity theory to approximate the correct strains. Equation (10.1) is not applicable to high angle boundaries ($\Phi \geq\ 5-10^{\circ}$) that would require ideally-spaced dislocations cores to overlap because, in that case, linear elasticity does not apply.

10.2 Application of the Read-Shockley Model to Create Anisotropic Grain Boundary Free Energies

He *et al.* [113] modified the derivation of Eq. (10.1) to obtain a $\gamma_{\mathrm{GB}}(\hat{\mathbf{n}}_{\mathrm{GB}})$ applicable to all low angle grain boundary orientations for primitive cubic crystal structures obeying isotropic elasticity. The modified form follows when the density of each set of dislocations in the boundary is determined (with Frank's formula [114]) for general $\hat{\mathbf{n}}_{\mathrm{GB}}$. The result,

$$\gamma_{\mathrm{GB}}(\hat{\mathbf{n}}_{\mathrm{GB}}) = \frac{Gb^2}{4\pi(1-\nu)}\Phi\left[\, L(\hat{\mathbf{n}}_{\mathrm{GB}}) - M(\hat{\mathbf{n}}_{\mathrm{GB}})\ln\Phi \,\right] \tag{10.2}$$

is used to produce anisotropic grain boundary energies for this study.

In Eq. (10.2), ν is Poisson's ratio, G is the shear modulus, and b is the magnitude of the Burger's vector. For a primitive cubic crystal structure, $b = a\langle 100\rangle$,

where a is the lattice constant. The parameters, $M(\hat{\mathbf{n}}_{\mathrm{GB}})$ and $L(\hat{\mathbf{n}}_{\mathrm{GB}})$ are

$$\begin{aligned} M(\hat{\mathbf{n}}_{\mathrm{GB}}) &= a_1 + a_2 - \nu n_{gb,3}^2 (1/a_1 + 1/a_2) \\ L(\hat{\mathbf{n}}_{\mathrm{GB}}) &= M(\hat{\mathbf{n}}_{\mathrm{GB}})(D_o - 1) + n_{gb,1}^2 a_1 + n_{gb,2}^2 a_2 - \\ &\qquad a_1 \ln a_1 - a_2 \ln a_2 + \nu n_{gb,3}^2 \left[(\ln a_1)/a_1 + (\ln a_2)/a_2 \right] \end{aligned} \tag{10.3}$$

where

$$\begin{aligned} a_1 &= \sqrt{n_{gb,1}^2 + n_{gb,3}^2} \qquad\qquad a_2 = \sqrt{n_{gb,2}^2 + n_{gb,3}^2} \\ \hat{\mathbf{n}}_{\mathrm{GB}} &= (n_{gb,1},\, n_{gb,2},\, n_{gb,3}) \end{aligned} \tag{10.4}$$

and the atomic deregistry of a dislocation core enters through D_o,

$$D_o = 1 + \ln\left(\frac{b}{2\pi r_o}\right) \tag{10.5}$$

for a dislocation core radius of r_o.

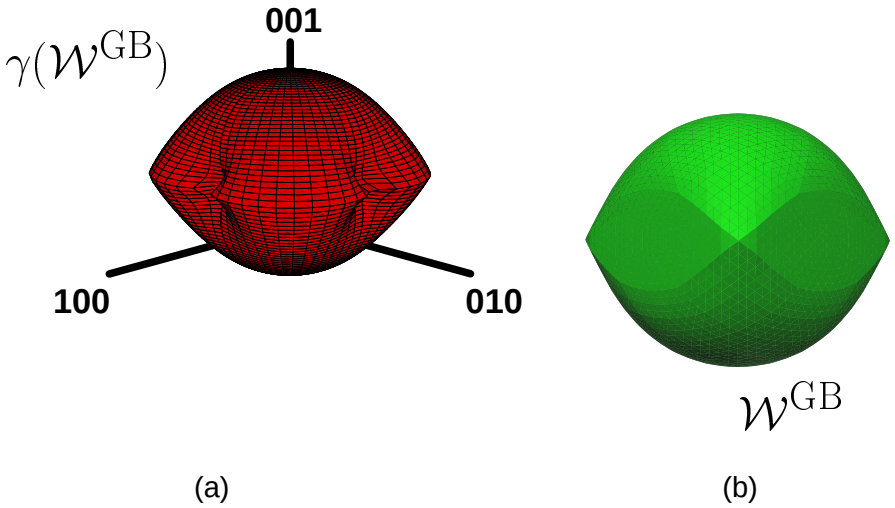

Figure 10.1: (a) A plot of the interfacial free energy density for a low angle $\vec{\mathbf{R}}_{\Phi} = 5^{\circ}\langle 001\rangle$ grain boundary derived from the Read Shockley model for a primitive cubic crystal structure. The calculations were performed using the methods in Ch. 6.1–subsec:MOCII-anisotropic with a derivation of He *et al.* [113]. (b) Cusps in (a) at (100)–type tilt orientations give facets at the pure tilt orientations on $\mathcal{W}_{\mathrm{GB}}$.

Figure 10.1(a) plots $\gamma_{\rm GB}(\hat{\mathbf{n}}_{\rm GB})$ for a $\vec{\mathbf{R}}_\Phi = 5^\circ\langle 001\rangle$ low angle boundary using the following parameters: $\nu = 1/3$, $G = 40$ GPa, $b = 1$ nm, $r_o = .1$ nm. (Parameters characteristic to Pb or Sn from [110] give only slight changes to the *shape* of the plot but give values of $\gamma_{\rm GB}(\hat{\mathbf{n}}_{\rm GB})$ that scale with G.) The results in the figure are consistent with those from He *et al.* [113]. There are four interfacial free energy minima, and they are located at (100), (010), $(\bar{1}00)$, and $(0\bar{1}0)$ on the great circle of tilt boundary orientations. The variation in $\gamma_{\rm GB}(\hat{\mathbf{n}}_{\rm GB})$ along the tilt boundary orientations is shown in Fig. 10.2(b). Tilt boundary orientations between the minima lie on a sharp edge that points out of the plot—for these $\hat{\mathbf{n}}_{\rm GB}$, boundary energy decreases sharply with an infinitesimal change in $\hat{\mathbf{n}}_{\rm GB}$ that produces components along the twist boundary.

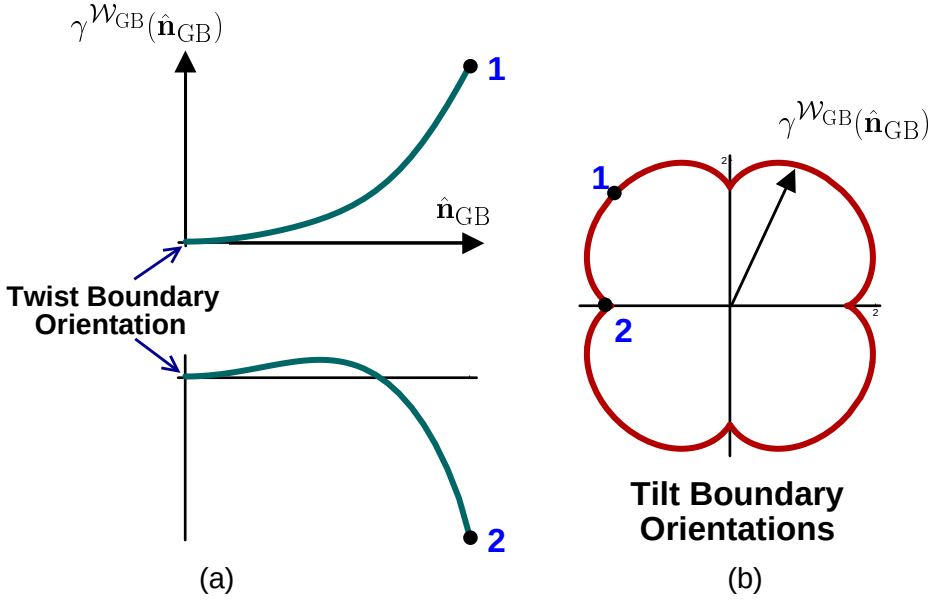

Figure 10.2: The variation in $\gamma(\mathcal{W}_{\rm GB})$ with $\hat{\mathbf{n}}_{\rm GB}$. (a) The energy density increases from the twist to tilt boundaries along a great circle with a $\langle 110\rangle$ zone axis (top) and, after passing through a local maximum, decreases along a great circle with a $\langle 100\rangle$ zone axis. (b) The variation in $\gamma(\mathcal{W}_{\rm GB})$ along the great circle of tilt orientations (the zone axis in this case is $[001]$, the twist boundary orientation).

Figure 10.1(b) gives the shape of a fixed volume—*i.e.*, $\mathcal{W}_{\rm GB}$—calculated from a modification to $\gamma_{\rm GB}(\hat{\mathbf{n}}_{\rm GB})$ making it HD1 in $\hat{\mathbf{n}}_{\rm GB}$. The equilibrium grain shape replaces tilt boundary energy minima with facets that meet at corners in the plot. Thus, the orientations that correspond to points along the outward edge of the $\gamma_{\rm GB}(\hat{\mathbf{n}}_{\rm GB})$–plot are replaced by a point on $\mathcal{W}_{\rm GB}$, indicating that these orientations are absent from an equilibrium shape and are thus unstable to reorientation to form components along $[001]$ and $[00\overline{1}]$ when $\hat{\mathbf{n}}_{\rm GB}^{avg}$ is fixed (the grain boundary of $\hat{\mathbf{n}}_{\rm GB}^{avg}$ is infinite in extent). The tilt boundary facets are separated from the twist boundaries by smoothly curved interface.

Materials rarely form primitive cubic crystal structures. However, qualitative results given by Eq. (10.2) are used to explain grain boundary roughening transitions in Cu [115] and perovskites [116], and the equation is sufficient for studying effects of grain boundary particles that replace anisotropic $\gamma_{\rm GB}(\hat{\mathbf{n}}_{\rm GB})$ derived from quantitative models. Extension of the Read Shockley model to other crystal structures is more complex because dislocation arrays that contribute to the boundary energy can react to form lower energy structures [114].

10.3 Anisotropic Grain Boundaries and Anisotropic Particles

Results for particles attached to boundaries described by the model $\gamma_{\rm GB}(\hat{\mathbf{n}}_{\rm GB})$ calculated in Fig. 10.1(a) are briefly described here. Although the model derives from dislocation theory, it is a macroscopic representation of a grain boundary and does not, therefore, give boundary particle shapes modified due to removal of individual dislocation line length. To allow comparisons with results in Ch. 9.4.4 for the heterogeneous nucleation of faceted particles at isotropic grain boundaries, $\gamma_{111} = 0.5\gamma(\mathcal{W}^{\rm sphere})$, $\gamma_{100}/\gamma_{111} = 1.15$, and the twist boundary energy density derived from the Read Shockley model is equated to the isotropic boundary energy used in Ch. 9.4.4, $\gamma_{\rm GB}(\hat{\mathbf{n}}_{001}) = 1.07\gamma(\mathcal{W}^{\rm sphere})$, where $\hat{\mathbf{n}}_{\rm GB} = \hat{\mathbf{n}}_{001}$ is a pure twist boundary.

Calculations show that boundaries of fixed average orientation with the $\mathcal{W}_{\rm GB}$ in Fig. 10.1(b) will facet for $\hat{\mathbf{n}}_{\rm GB}^{avg}$ in the neighborhood of tilt boundary orienta-

tions. This result is not surprising because $\mathcal{W}_{\mathrm{GB}}$ replaces tilt orientations with broad $\{100\}$ and $\{010\}$ facets, and, for this reason, formation of these facets is expected near the tilt boundaries [24].

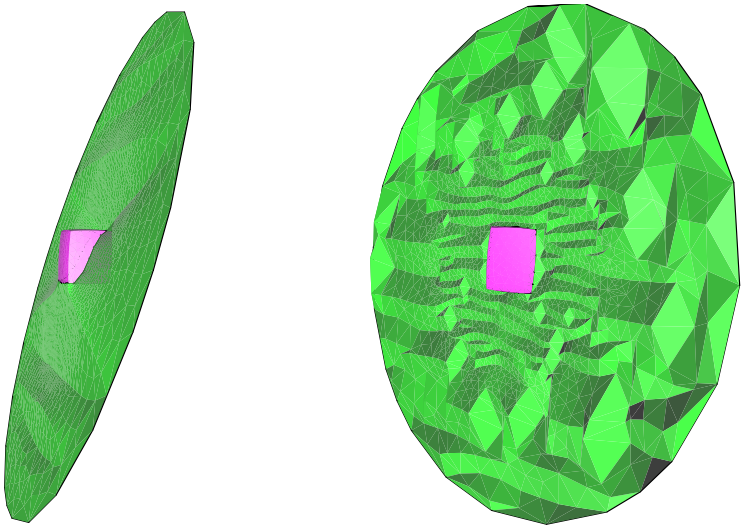

Figure 10.3: (a) Grain boundary facets and (b) anisotropic hills and valleys that result with a $\mathcal{W}_{\mathrm{cube}}^{\mathrm{cube}}$ boundary particle.

Boundary faceting off of the tilt boundaries produces $\{100\}$ and $\{010\}$ orientations in proportions that conserve $\hat{\mathbf{n}}_{\mathrm{GB}}^{avg}$. Fig. 10.3(a) is an example where $\hat{\mathbf{n}}_{\mathrm{GB}}^{avg}$ has no components along $\{010\}$, and $\hat{\mathbf{n}}_{\mathrm{GB}}^{avg}$ decomposes into (100) facets and lower energy orientations inclined toward the misorientation axis. Boundary faceting for orientations on the asymmetric tilt boundaries can produce, in addition to $\{100\}$ and $\{010\}$, equal proportions of the limiting orientations defining the $\mathcal{W}_{\mathrm{GB}}$ edge that lies at tilt boundary orientations and extends between facets. These limiting orientations have components along the twist boundary orientations.

Figure 10.3(b) gives an example of a hill-and-valley structure for the (110) tilt orientation—this orientation gives the smallest increase in interfacial free energy for the calculated boundary particles. The boundary facets become larger with distance from the particle—this is due to the details of the calculation, which uses a mesh size that increases with radial distance from the particle. The calculated results are not intended to predict the exact boundary shape, and in calculations that do not account for energies due to edges or corners, a single calculation gives one in an infinite set of possible solutions.

A result of interest in applications where grain boundary sliding must be limited, particle attachment can induce boundary faceting. Calculations of the boundary that appears in Fig. 10.3(a) show that it is flat in the absence of an attached particle and re-converges to a plane when subject to perturbations allowing it to sample the faceted orientations of $\mathcal{W}_{\mathrm{GB}}$. Distortions necessary to accommodate the boundary particle shape—*i.e.*, geometric constraints forcing the boundary to locally reorient—produce low energy features allowed by $\mathcal{W}_{\mathrm{GB}}$ for fixed $\hat{\mathbf{n}}_{\mathrm{GB}}^{avg}$ that are otherwise absent. These results provide energetic arguments supporting reports [22, 117, 118] of precipitate-induced boundary faceting.

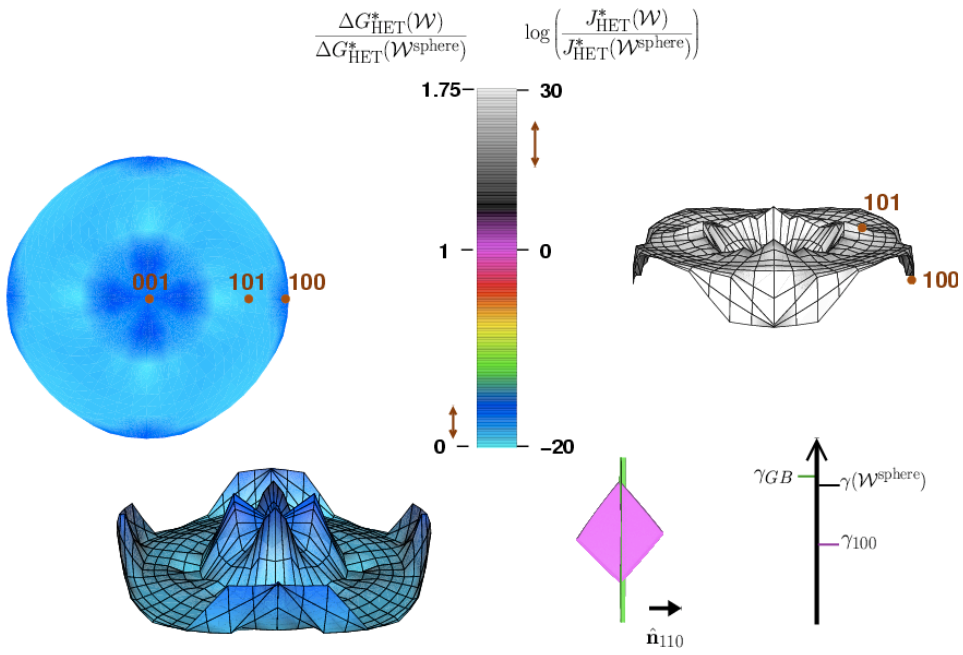

Figure 10.4: (a) Relative heterogeneous nucleation barrier and (b) nucleation rate for $\mathcal{W}^{\mathrm{cube}}_{\mathrm{cube}}$ boundary particles attached to an isotropic grain boundary, where $\vec{\mathbf{R}}_{\Phi} = 5^{\circ}\langle 001\rangle$. The inset shows the boundary particle configuration at a (110) boundary orientation.

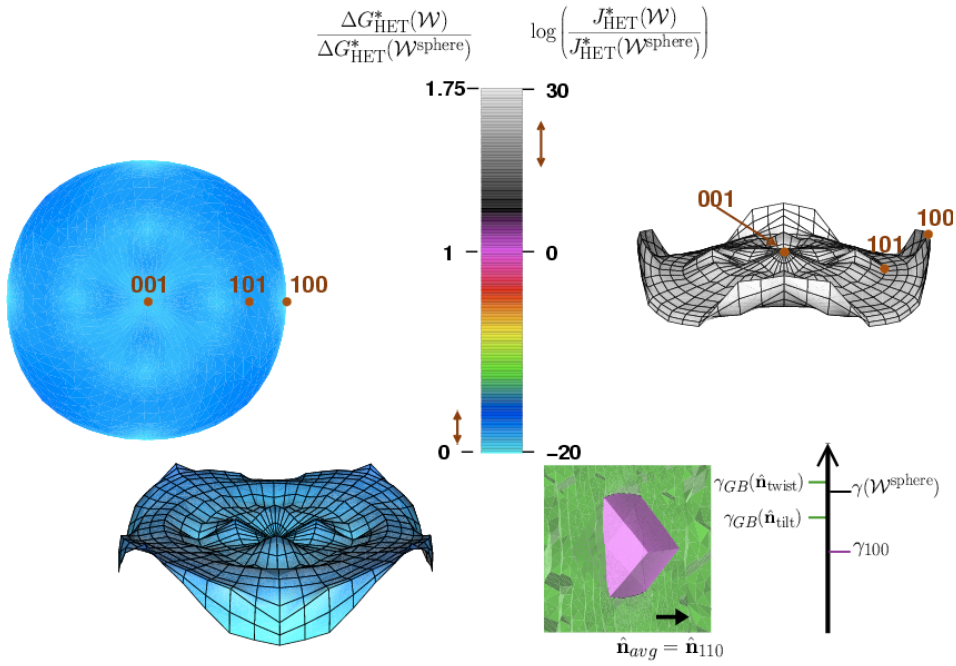

Figure 10.5: (a) Relative heterogeneous nucleation barrier and (b) nucleation rate for $\mathcal{W}^{\mathrm{cube}}_{\mathrm{cube}}$ boundary particles attached to the anisotropic boundary with the $\mathcal{W}_{\mathrm{GB}}$ of Fig. 10.1. The inset shows the boundary particle configuration at a (110) boundary orientation, and $\gamma(\hat{\mathbf{n}}_{\mathrm{tilt}}) = \gamma(\hat{\mathbf{n}}_{100})$.

Figure 10.4 plots $\Delta G^{*}_{\mathrm{HET}}(\mathcal{W}^{\mathrm{cube}}_{\mathrm{cube}}/\mathcal{W}^{\mathrm{sphere}})$ and $J^{*}_{\mathrm{HET}}(\mathcal{W}^{\mathrm{cube}}_{\mathrm{cube}}/\mathcal{W}^{\mathrm{sphere}})$ for an isotropic boundary of $\gamma_{\mathrm{GB}} = 1.07\gamma(\mathcal{W}^{\mathrm{sphere}})$ and characterized by a low misorientation $\vec{\mathbf{R}}_{\Phi} = 5^{\circ}\langle 001\rangle$. The values are normalized relative to the heterogeneous nucleation of an isotropic particle at the same boundary. The eight-fold rotational symmetry of solutions that occurred in Ch. 9.4.4 is replaced with four-fold symmetry because $\Phi = 5^{\circ}$ rather than 45°. Results for the anisotropic boundary are plotted in Fig. 10.5. In this case, values are normalized relative to the heterogeneous nucleation of an isotropic particle at the anisotropic boundary. Four-fold symmetry is present in the anisotropic case because the misorientation axis is parallel to the four-fold rotational axes of $\mathcal{W}_{\mathrm{GB}}$ as well as the $\mathcal{W}^{\mathrm{cube}}$ that define the boundary particle shapes.

For the isotropic boundary, a 5° misorientation about $\langle 001\rangle$ produces configurations of larger energy than $\vec{\mathbf{R}}_{\Phi} = 45^{\circ}\langle 001\rangle$ (Ch. 9.4.4) for all $\hat{\mathbf{n}}_{\mathrm{GB}}$ except for the twist and portions of the tilt boundaries. The negligible difference in free energy produced at twist boundaries is discussed in Ch. 11.2.1. Those tilt boundaries that yield a lower energy configuration for $\vec{\mathbf{R}}_{\Phi} = 5^{\circ}\langle 001\rangle$ typically have $\mathcal{W}^{\mathrm{cube}}_{\mathrm{cube}}$ shapes with fewer facets (than those giving a lower energy for $\vec{\mathbf{R}}_{\Phi} = 45^{\circ}\langle 001\rangle$).

Results indicate that the heterogeneous nucleation barrier at the anisotropic boundary changes in a manner similar to the boundary free energy density shown in Fig. 10.2(a). Boundary orientations that lie on a great circle with a zone axis parallel to either a (100) or (010) symmetric tilt orientation offer the most favorable nucleation sites when the distance from the 5° twist boundaries is fixed. Along these great circles, the barrier increases from shallow minima at the twist boundaries to a maximum and then decreases to a global minimum at the symmetric tilt boundaries. The maximum is actually a saddle point in the heterogeneous nucleation barrier because the barrier increases to a maximum 45° along the corresponding latitude. The great circles connecting this (latitudinal) maximum to the twist and tilt orientations have zone axes parallel to $\{110\}$ tilt orientations and give the locus of orientations that, for a fixed distance from the twist boundaries, give the largest nucleation barrier, with the barrier continuously increasing as the tilt boundary is approached. The (110) tilt boundary thus gives the largest nucleation barrier for $\mathcal{W}^{\mathrm{cube}}_{\mathrm{cube}}$ particles. However, the barrier is still reduced relative to that of isotropic particles with dihedral angles larger than $2\theta_L$; for $T = \Delta G^{*}_{\mathrm{HET}}(\mathcal{W}^{\mathrm{sphere}})/60k$, $\mathcal{W}^{\mathrm{cube}}_{\mathrm{cube}}$ par-

ticles would occur by a factor of $\sim 10^{21}$ more frequently than lenticular particles defined by $\gamma(\mathcal{W}^{\text{sphere}})$ at (110) anisotropic boundary orientations in a fixed volume of material.

10.4 Anisotropic Grain Boundaries and Isotropic Particles: Unexpected Results

Isotropic boundary particles may induce boundary reorientation in cases where the undecorated boundary remains flat. The smoothly curved particle shape allows the particle-boundary triple line to choose a path allowing the boundary to locally form low energy orientations that reduce the total interfacial free energy. This result is surprising because isotropic boundary particles are typically regarded as portions of spheres abutting at a flat boundary.

As an example, consider the orientation near (211) in Fig. 10.6. When the boundary is isotropic, it is distorted by a $\mathcal{W}^{\text{cube}}_{\text{cube}}$ particle, forming a minimal surface ($\kappa = 0$) that attaches to the triple line. When the boundary is anisotropic and described by the $\mathcal{W}_{\text{GB}}$ of Fig. 10.1(b), a $\mathcal{W}^{\text{cube}}_{\text{cube}}$ particle distorts the boundary, which forms a surface of zero constant weighted mean curvature ($\kappa_\gamma = 0$) with broad facets parallel to (100).

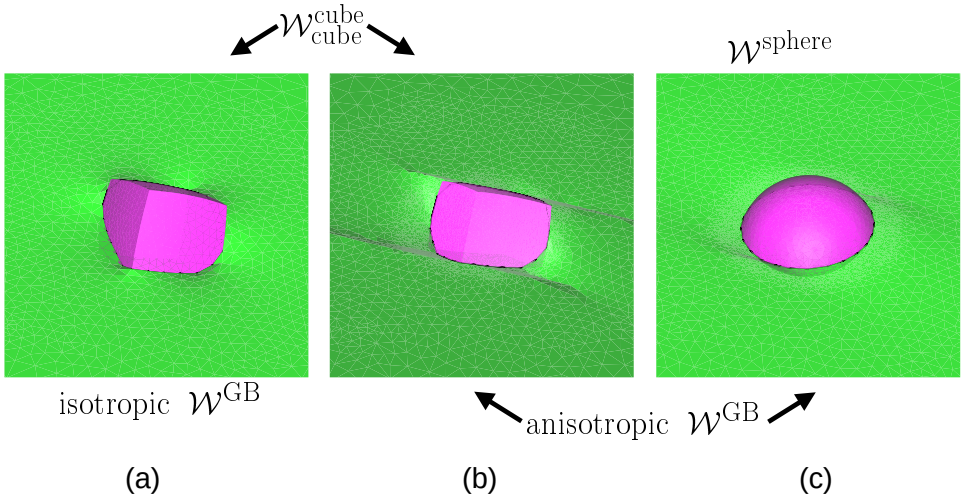

Figure 10.6: (a) A $\mathcal{W}^{\text{cube}}_{\text{cube}}$ attached to an isotropic boundary, (b) a $\mathcal{W}^{\text{cube}}_{\text{cube}}$ attached to an anisotropic boundary, and (c) an isotropic particle attached to an anisotropic boundary.

When an isotropic particle attaches to the anisotropic boundary, the triple line moves out of the plane defined by $\hat{\mathbf{n}}_{\mathrm{GB}}^{avg}$ near orientations for which the broad boundary facets formed around $\mathcal{W}_{\mathrm{cube}}^{\mathrm{cube}}$, tracing an ellipse that is rotated a few degrees about $\langle 110 \rangle$. The boundary is thus inclined to form (100) orientations and neighboring low energy interface. The total interfacial free energy of the lenticular particle attached to the same boundary but under the constraint that the boundary remain planar is larger than that of the deformable boundary shown in Fig. 10.6(c). This result shows that the local geometry of interfaces forming the triple junction can vary with position. As demonstrated by King [95], multiple equivalent geometries can define an equilibrium triple junction joining anisotropic and isotropic interfaces.

Chapter 11

Extensions

11.1 Utility of Calculations: Brief Examples

11.1.1 Coarsening and Anticoarsening Phenomena

Generally, a system that contains a fixed amount of particle volume can, for $\gamma_{GB} \sim \gamma_P$ (where p denotes particle interface), reduce its total interfacial free energy by combining the volume in a single particle.

Consider the construction of an interfacial particle from square Wulff shapes (called $\mathcal{W}^{\text{square}}$ here) in Ch. 5.3.1. By comparing the changes in free energy corresponding to each configuration, Appendix G shows that interfacial free energy is reduced when a single particle dissociates into two particles of equal volume if

$$\gamma_{GB}/\gamma(\mathcal{W}^{\text{square}}) > 2\sqrt{2}$$

Previous work has labeled such dissociation phenomena "anticoarsening" [48].

A calculation of octahedral particles attached to pure twist boundaries of $\vec{\mathbf{R}}_\Phi = 12^\circ\langle 001\rangle$—representative of the oxide precipitates fabricated in Si to study boundary particle shape and size [49]—shows that there are cases for which it is favorable for a single $\mathcal{W}^{\text{oct}}_{\text{oct}}$ boundary particle to divide into a larger, perhaps unbounded, number of equal volumes. If the additional boundary energy due to rumpling could

be neglected, a construction as in Appendix G shows that

$$\gamma_{GB}/\gamma(\mathcal{W}_{oct}^{oct}) > 3.46$$

would give be the condition for anticoarsening.

Fig. 11.1 shows the particles calculated for this example. The calculated results indicate that anticoarsening is expected for

$$\gamma_{GB}/\gamma(\mathcal{W}_{oct}^{oct}) \gtrsim 3.8$$

which is consistent with the modification to the construction in Appendix G that occurs for rumpled boundaries—because the amount of boundary energy removed by a particle in $\mathbf{R^3}$ is reduced when the boundary rumples, the displacement of $\mathcal{W}$ for a given boundary is smaller than the boundary $\vec{\vec{\xi}}_{GB}$, and larger boundary energies are needed to give a reduction in energy on boundary particle formation.

(a) (b)

Figure 11.1: (a) A $\mathcal{W}_{oct}^{oct}$ attached to a pure 12° twist boundary that has less energy than (b) the combined energy of two identical $\mathcal{W}_{oct}^{oct}$ that half the volume of the single particle and are attached to the same boundary.

11.1.2 Boundary Particle Faceting in One Grain: Choice of Grain

The high resolution TEM image shown in Fig. 11.2(a) shows that, to remain a single crystal, a boundary particle will facet in one grain and assume a spherical cap in the other. The image shows neighboring $\mathcal{W}^{\text{Toct}}_{\text{sphere}}$ to facet on opposite sides of the boundary. The boundary appears to change position from one side of the lower particle in the figure to the other, suggesting boundary rumpling in the vicinity of the second particle. These results are similar to observations of carbides at serrated boundaries in austenitic steels, where neighboring carbides along the same boundary will retain coherency with opposite grains to create a "zig-zag" faceting pattern [22].

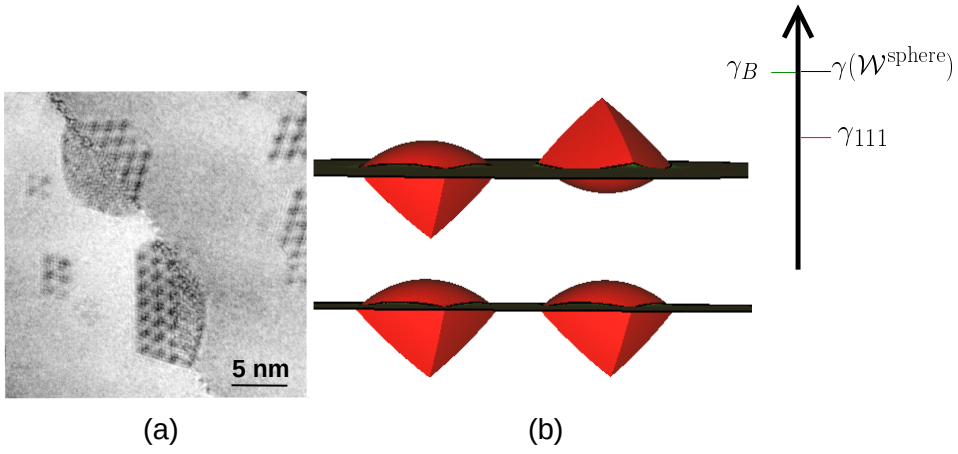

Figure 11.2: (a) A high resolution TEM micrograph of two single crystal Pb particles attached to the same Al grain boundary. In each case, the particle is a spherical cap in one grain and a truncated octahedron in the other. *(Courtesy of U. Dahmen, NCEM, LBNL.)* (b) Calculations of $\mathcal{W}^{\text{oct}}_{\text{sphere}}$ show that the energy is the same regardless of which side each particle facets in when the boundary distortion caused by each (for an isotropic boundary) do not overlap.

Calculations show that, when attached to a boundary of fixed $\hat{\mathbf{n}}_{\mathrm{B}}^{avg}$, similarly oriented non-interacting particles have the same interfacial free energy as particles forming a zig-zag faceting pattern. Calculations in the next section show that particles, zig-zagged or not, can arrange to give lower energy configurations when boundary distortion from one particle coincides with that of another so that the total distortion is less than what would occur if the particles were widely spaced.

From Ch. 9.4.3, Ch. 11.2.1, and [55], it is speculated in this thesis that one of the boundary particles in Fig. 11.2(a) is metastable relative to the other or that, if Fig. 11.2(a) gives boundary distortion which was not induced by boundary particles, the observed alternation in particle faceting could result because $\hat{\mathbf{n}}_{\mathrm{GB}}$ changes along the boundary. When $\vec{\mathbf{R}}_{\Phi}$ is fixed, the $\mathcal{W}_{\mathrm{sphere}}^{\mathrm{Toct}}$ boundary particle shape has one degree of freedom at a given $\hat{\mathbf{n}}_{\mathrm{GB}}$—to facet in grain C_1 or grain C_2. In this case, neighboring boundary particles could be attached to (locally) different $\hat{\mathbf{n}}_{\mathrm{GB}}$ along the same grain boundary. Because the facets of boundary particles are topotactically aligned with the matrix, faceting in grain C_1 at a general grain boundary will produce a different shape (and thus total interfacial free energy) than faceting in grain C_2. Hence, the choice of which grain a fixed volume of particle will facet in is, under equilibrium conditions, governed by a minimization in interfacial free energy that is dependent on $\hat{\mathbf{n}}_{\mathrm{GB}}$.

11.1.3 Spatial Arrangement of Boundary Particles

Boundary particles that distort a boundary can arrange so as to minimize the distorted boundary area. Such a case could occur if the particles did not coarsen—for instance, if γ_{GB} is much greater than the particle interface energy density as in Ch. 11.1.1.

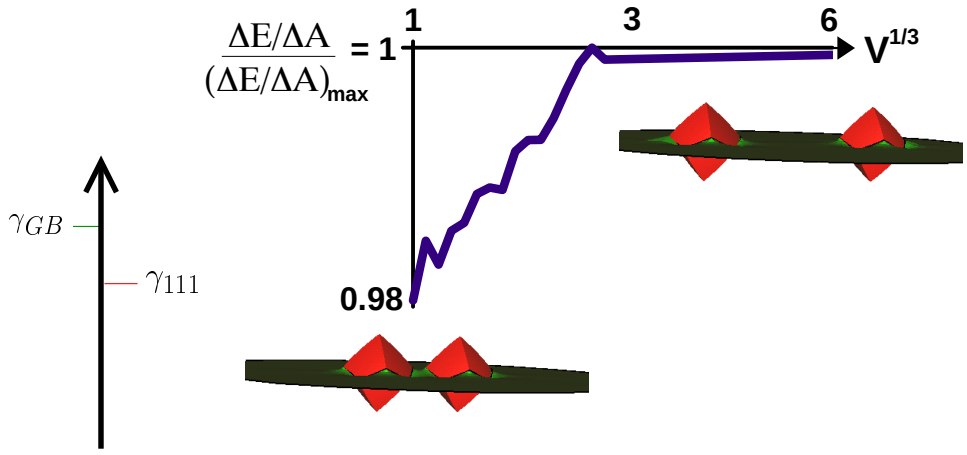

Figure 11.3: (Top) Neighboring $\mathcal{W}_{\text{oct}}^{\text{oct}}$ that are identical can lower interfacial free energy by locating close to one another to eliminate the total boundary distortion. (Bottom) A plot of the change in interfacial free energy per unit change in area on the formation of the boundary particles shows a plateau at a displacement of approximately $2.8V^{1/3}$, where V volume of each particle.

Figure 11.3 gives an example showing energy to increase as particles relocate. For the example, two $\mathcal{W}_{\text{oct}}^{\text{oct}}$ particles of equal size attached to a single boundary, the particles are constrained to lie along a line parallel to $\langle 100 \rangle$ (defined relative to C_1), and $0.75\gamma_{\text{GB}} = \gamma_{111}$. The lowest energy configuration calculated occurs when the particles are close so that boundary distortions occurring between particles then coincide to produce one distortion that contributes less interfacial free energy than the two separated distortions.

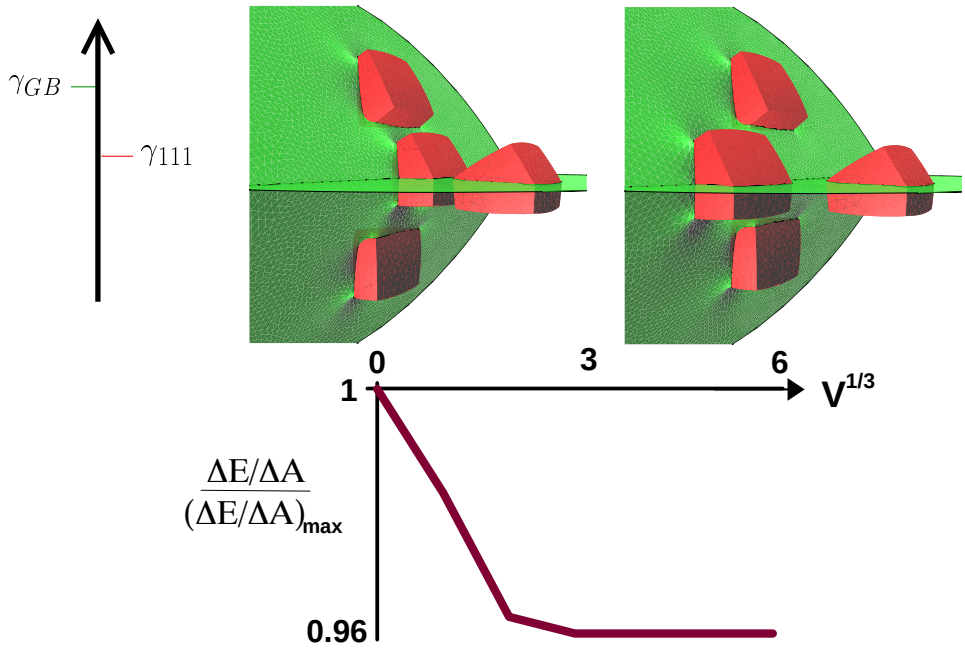

Figure 11.4: (Top) This system of neighboring particles formed from identical $\mathcal{W}^{\text{cube}}$ can lower its interfacial free energy by displacing the triple junction particle from the boundary particle cluster. (Bottom) The change in interfacial free energy per change in area for the formation of the boundary and triple junction particles decreases to an approximately constant value when the triple junction particle is displaced by approximately $2.5V^{1/3}$ for particles of the same volume, V.

More pronounced energy changes occur for displacements of the triple junction particle that is shown in Fig. 11.4. This particle is situated between three boundary particles, where each boundary forming the triple junction contributes one boundary particle. For this example, all particles are formed from combinations of $\mathcal{W}^{\text{cube}}$, and $0.75\gamma_{\text{GB}} = 1.15\gamma_{100}$. Initially the centers of the four particles lie in a $\{001\}$ plane. Interfacial free energy decreases as the triple junction particle is displaced from the other particles along the triple junction, which is oriented along $\langle 001 \rangle$. In this case, energy decreases at small displacements and then increases to a constant value when the triple junction particle is sufficiently removed to have no interaction with the other particles. Larger changes in energy occur with particle displacement because displacements alter rumpling due to four, rather than two, particles.

Both examples reflect highly constrained minima. However, they show that, in addition to selecting boundaries offering low energy configurations, boundary particles can position so as to reduce the total boundary rumpling necessary.

11.2 Microstructural Torques

Second-phase particles can alter the geometric stability of grain boundaries and thereby influence equilibrium grain shapes and the texture of a polycrystal. The torque acting to rotate grains abutting a boundary of fixed $\hat{\mathbf{n}}_{\text{GB}}$, typically observed in the creation of recrystallization nuclei but also in the reduction in grain boundary energy for columnar grains in thin films [119], is considered in Ch. 11.2.1. The torque to rotate a boundary of fixed $\vec{\mathbf{R}}_{\Phi}$ was treated by Herring [120] and is considered for boundaries decorated with particles in Ch. 11.2.2.

In both sections, changes to grain boundary shape are limited to the neighborhood of a particle to avoid complications that would arise in real systems where one grain is connected to a number of others through individual boundaries. This assumption is realized with the embedded spherical grain construct of Ch. 9.4.4. However, for locally planar boundary the embedded grain would necessarily be much larger than a boundary particle, meaning that morphological changes dependent on grain size (*e.g.*, grain rotation accommodated by grain sliding) would proceed more slowly at larger grain sizes [119].

11.2.1 Grain Rotations

Grain rotation may reduce the total interfacial free energy by allowing boundary particles to change shape. When $\hat{\mathbf{n}}_{\mathrm{GB}}$ is fixed, a torque tending to alter particle shape must also tend to alter grain misorientation.

An Example of Grain Rotation in $\mathbf{R^2}$

It is instructive to consider the particle constructed in Ch. 5.3 before proceeding to the numerical examples for particles in $\mathbf{R^3}$. Let boundary orientation be fixed to $\hat{\mathbf{n}}_{\mathrm{GB}} = \langle 01 \rangle$, and let $\gamma_{\mathrm{GB}} = \gamma_{10}$, where γ_{10} is the free energy density of each square particle facet. A change in particle shape can occur if grain C_2 rotates. In this example, the rotation of C_2 produces a family of boundary particle shapes that has four-fold rotational symmetry in Φ for a γ_{GB} that is isotropic in Φ. (In $\mathbf{R^2}$, $\vec{\mathbf{R}}_{\Phi} = \Phi$.)

Figure 11.5 plots changes to the interfacial free energy per unit area of particle as a function of Φ. Each point on the plot gives the equilibrium configuration for the Φ defined by that point. All information is contained in Fig. 11.5(a), which shows $1/8$ of the possible misorientation angles Φ. The results are plotted in polar coordinates in Fig. 11.5(b) for all misorientations to show the symmetry of solutions.

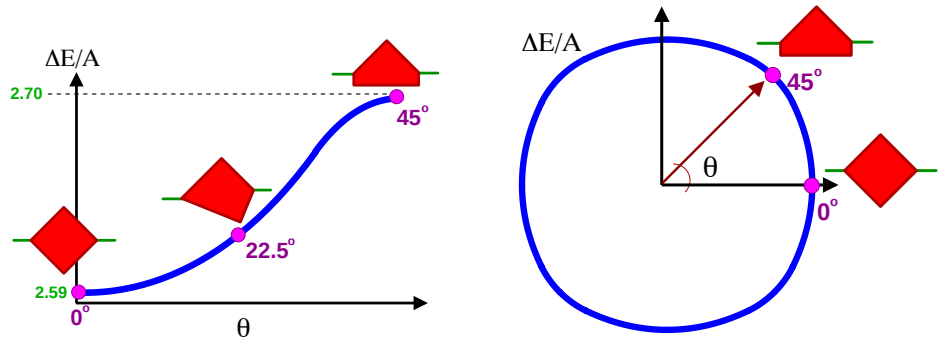

Figure 11.5: Grain rotations in $\mathbf{R}^2$ driven by a reduction in the total interfacial free energy. (a) Cartesian and (a) polar plots of changes to the interfacial free energy, ΔE, for a configuration divided by the area of the particle, A. The boundary jumps at $\Phi = 22.5^\circ$. Values of $\Delta E/A$ that appear in the figure are in terms of $\gamma_{10}/[\text{LENGTH}]$ for a unit area of particle.

For this case, energetic minima occur when there is no misorientation, $\Phi = 90^\circ n$, and maxima occur at the largest misorientations, $\Phi = 90^\circ(n+1/2)$ for any integer n. Thus, a torque will tend to rotate grain C_2 into a configuration of zero misorientation when $\Phi \neq 0$, and the torque will increase as $\Phi \rightarrow (90+1/2)n$.

Generally, interfacial free energy densities are anisotropic in $\vec{\mathbf{R}}_\Phi$ because some Φ provide a larger degree of lattice matching across a boundary than others, and a zero misorientation would imply the absence of a grain boundary and thus of grain boundary energy. However, this result does not suggest that a boundary particle will increase grain size by eliminating an entire grain boundary through grain rotation because it is based on an analysis that assumes γ_{GB} is finite and independent of Φ. In this example, $\Phi = 0$ produces a minimum because the it gives the smallest change in line length for the fixed area of boundary particle.

Grain Rotations in $\mathbf{R^3}$

In $\mathbf{R^2}$, non-zero Φ produce pure tilt grain boundaries. The examples considered in this section pertain to a case not possible in $\mathbf{R^2}$—pure twist boundaries. Particles attached to (001) orientations of grain boundary are considered here. Twist boundaries result from the rotation of one grain (in this case C_2) about the unit normal to the boundary. For $\vec{\mathbf{R}}_\Phi = \Phi\langle 001\rangle$, misorientation angle is the only degree of freedom.

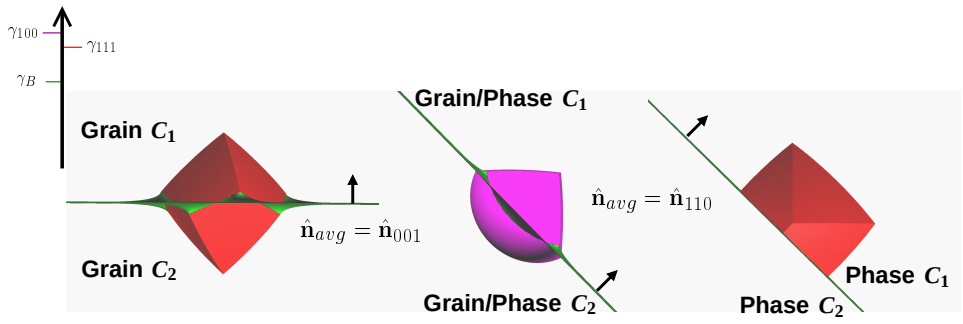

Figure 11.6: Fully crystalline particles attached to pure twist grain boundaries.

As in Ch. 9.4.4, this example considers grain boundary $\mathcal{W}_{\text{cube}}^{\text{cube}}$, $\mathcal{W}_{\text{oct}}^{\text{oct}}$, and $\mathcal{W}_{\text{Toct}}^{\text{Toct}}$ particles for $\gamma_{100}/\gamma_{111} = 1.15$. Here, $\gamma_{\text{GB}} = 0.75\gamma_{111}$. Equilibrium configurations for $0 \leq \Phi \leq 45^\circ$ are given in Fig. 11.6. Because $\hat{\mathbf{n}}_{\text{GB}}$ coincides with four-fold rotation axes of each $\mathcal{W}$, the configurations in the figure comprise the distinct set of configurations.

Plotted with the configurations are changes to the total interfacial free energy per unit volume of boundary particle, $\Delta E(\mathcal{W})/V$. This ratio is useful for considering the energy-minimizing shape for a fixed volume.

For $\mathcal{W}_{\text{oct}}^{\text{oct}}$ and $\mathcal{W}_{\text{Toct}}^{\text{Toct}}$, lowest-energy twist angles give are those that give the least boundary distortion. Distortion and $\Delta E(\mathcal{W})/V$ increase continuously for these shapes from a minimum at $\Phi = 0$ to a maximum at $\Phi = 45^\circ$. In contrast, for $\mathcal{W}_{\text{cube}}^{\text{cube}}$, distortion and $\Delta E(\mathcal{W})/V$ are invariant to Φ. This invariance occurs because γ_{GB} is parallel to orientations of $\mathcal{W}_{\text{cube}}^{\text{cube}}$, meaning that $\Phi \neq 0$ can be accommodated by pushing particle volume entirely to one side of the boundary to give a smaller $\Delta E(\mathcal{W})/V$ than would be produced by accommodating the misorientation by boundary distortions. In effect, determination of $\mathcal{W}_{\text{cube}}^{\text{cube}}$ reverts to a Winterbottom construction for applications in, *e.g.*, MgO [121].

Similar to the results in Chs. 9.4.3–9.4.4,

$$\Delta E(\mathcal{W}_{\text{Toct}}^{\text{Toct}}) < \Delta E(\mathcal{W}_{\text{oct}}^{\text{oct}}) < \Delta E(\mathcal{W}_{\text{cube}}^{\text{cube}})$$

for all Φ. Configurations of the greatest interfacial free energy are formed from $\mathcal{W}_{\text{cube}}^{\text{cube}}$ particles, which are completely described by the larger facet free energy density (γ_{100}) and tend to produce shapes with the most surface area. Truncated octahedral $\mathcal{W}$ produce shapes that use a combination of $\{100\}$ and $\{111\}$ orientations, reducing the total surface necessary to enclose a fixed volume and compensating for the introduction of larger energy $\{100\}$ interface.

As demonstrated here for $\mathcal{W}_{\text{Toct}}^{\text{Toct}}$ and $\mathcal{W}_{\text{oct}}^{\text{oct}}$, boundary particles could affect grain rotation. If grain rotation is inhibited, an energetic minimum can still be reached—*e.g.*, through the nucleation of a new grain at triple line between the boundary and particle, keeping $\hat{\mathbf{n}}_{\text{GB}}$ fixed. Observations that could indicate the effect of boundary particles on (de-)stabilizing a particular Φ include measurements of dihedral angles between three grain boundaries or two free surfaces and a grain

boundary [61] and statistical studies of the frequency of certain pure twist misorientations [121] and misorientations at general $\hat{\mathbf{n}}_{\mathrm{B}}$ [6, 7].

11.2.2 Grain Boundary Rotations

An Example of Grain Boundary Rotation in $\mathbf{R}^2$

When $\vec{\mathbf{R}}_{\Phi}$ is fixed, a boundary particle will exert a torque on the boundary if the free energy of the system can decrease with changes in $\hat{\mathbf{n}}_{\mathrm{GB}}$. Consequently, boundary particles may influence $\mathcal{W}_{\mathrm{GB}}$.

Consider the example in Ch. 11.2.1, and let $\Phi = 45^{\circ}$. Because γ_{GB} for this example is isotropic in $\hat{\mathbf{n}}_{\mathrm{GB}}$, interfacial free energy is minimized for $\Theta = 45^{\circ}n$, where $\hat{\mathbf{n}}_{\mathrm{GB}} = \langle \cos\Theta,\ \sin\Theta \rangle$. The largest interfacial free energy corresponds to a nearly symmetric tilt boundary that occurs at $\Theta = 45^{\circ}(1/2+n)$. The shape does not change continuously as $\hat{\mathbf{n}}_{\mathrm{GB}}$ passes through this maxima, where there is a bifurcation giving two solutions that differ only in which grain borders three particle facets and which grain borders two.

The eight-fold symmetry of solutions given in Fig 11.7 is expected because, as in Ch. 9.4.4, the boundary particles are formed from $\mathcal{W}$ that are misoriented by 45° about an axis parallel to the four-fold axes of the $\mathcal{W}$ [107]. The results plotted in Fig. 11.7(b) indicate changes to the interfacial free energy for a boundary decorated with particles of fixed area. This plot is different from a γ–plot describing the boundary uniformly decorated with the particles, which would give $\Delta E/\Delta l$ as a function of $\hat{\mathbf{n}}_{\mathrm{B}}$, where Δl is the change in line length. In this example, $\gamma_{\mathrm{GB}} = \gamma_{10}$, meaning that $\Delta E/\Delta l$ is a constant and $\mathcal{W}_{\mathrm{GB}}$ remains a circle when uniformly decorated with particles.

For more general cases where $\gamma_{\mathrm{GB}} \neq \gamma_{10}$, $\Delta E/\Delta l$ will vary with $\hat{\mathbf{n}}_{\mathrm{B}}$, and $\mathcal{W}_{\mathrm{GB}}$ will be modified. For instance, the boundary particle that is produced in Fig. 11.7 when $\Theta = 22.5^{\circ}$ replaces more boundary line length than the particle that forms at $\Theta = 0^{\circ}$. If it were possible to retain the same particle shapes for a $\gamma_{\mathrm{GB}} > \gamma_{10}$, a plot of $\Delta E/\Delta l$ would have minima at $\Theta = 45^{\circ}(1/2+n)$, and, for deep cusps in $\Delta E/\Delta l$ $\mathcal{W}_{\mathrm{GB}}$ would be octagonal. To study the effect of boundary particles on changes to $\mathcal{W}_{\mathrm{GB}}$, Anneals of a thin metal wire segmented by grain boundaries to form a bamboo structure, used to study the effect of boundary orientation on γ_{GB} for fixed

$\vec{\mathbf{R}}_{\Phi}$ [13], could be used.

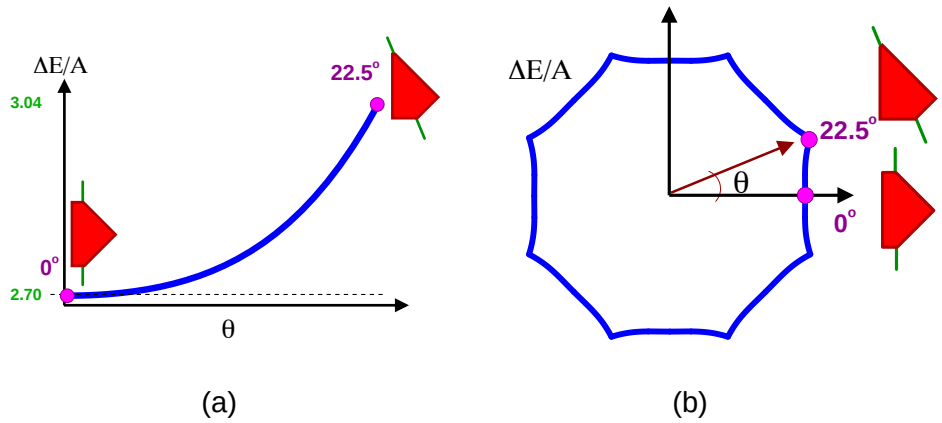

Figure 11.7: Grain boundary rotations in $\mathbf{R^2}$ driven by reductions in the total interfacial free energy. Both (a) and (b) are plotted as in Fig. 11.5. Values of $\Delta E/A$ that appear in the figure are in terms of $\gamma_{10}/\text{LENGTH}$ for a unit area of particle.

Although the polar plots in Figs. 11.7(b) and 11.5(b) give a relative measure of changes in free energy under different geometric constraints, the plots give an equivalent solution at four points. These four points coincide when the plots are superimposed and one plot rotated about the origin by 45°. In this example, the coincident points are $\Phi = 90^\circ(n+1/2)$ and $\Theta = 45^\circ n$, and the solution minimizes changes to the interfacial free energy when the reorientation of the boundary is inhibited but gives a maximum when the reorientation of one grain is inhibited. The boundary geometry providing a global minimum would involve calculations over $0 \leq \Phi \leq 45^\circ$ and $0 \leq \Theta \leq 45^\circ$, and if the boundary free energy constraint, $\gamma_{GB} = \gamma_{10}$, could be replaced with realistic boundary energies, the results could be directly compared to systems such as thin films where $\vec{\mathbf{R}}_\Phi \perp \hat{\mathbf{n}}_{GB}$.

Grain Boundary Rotations in $\mathbf{R}^3$

When $\vec{\mathbf{R}}_\Phi$ is fixed, and for the set of $\mathcal{W}$ and interfacial free energies used in Ch. 11.2.1, boundary orientations giving minima in the total interfacial energy for a fixed volume are most often those that involve the least amount of boundary distortion.

A grain boundary that can rotate at fixed $\vec{\mathbf{R}}_\Phi$ has two degrees of freedom. To determine the dependence of $\Delta E(\mathcal{W})/V$ on $\hat{\mathbf{n}}_{GB}$, boundary configurations for $\vec{\mathbf{R}}_\Phi = 45^\circ\langle 001\rangle$ were calculated with $\hat{\mathbf{n}}_{GB}$ separated by 15° arcs on a spherical grid. (This $\vec{\mathbf{R}}_\Phi$ corresponds to the highest energy configurations given by $\mathcal{W}^{oct}_{oct}$ and $\mathcal{W}^{Toct}_{Toct}$ in Ch. 11.2.1. Those configurations are, in this chapter, allowed to relax into energy minima accessible through boundary rotation.)

As expected from results in Ch. 9.4.4 and [107], an eight-fold rotation axis along $\langle 001\rangle$ relates boundary sites that give energetically equivalent boundary particle configurations. The $8/mmm$ point group symmetry that results is less than that for the individual $\mathcal{W}$, which has cubic symmetry and would indicate that $1/48$ of the solutions are necessary, because configurations occurring at the two pure twist boundary orientations ($\hat{\mathbf{n}}_{GB} \parallel \langle 001\rangle$) differ from those at the tilt boundaries ($\hat{\mathbf{n}}_{GB} \parallel \langle hk0\rangle$). In this case, all boundary orientations between the twist boundary and two points separated by 22.5° on the great circle of tilt boundaries must be considered, increasing the number of necessary calculations from considering $1/48$ to

$1/32$ of all boundary orientations.

The equilibrium boundary geometries for a fixed $\vec{\mathbf{R}}_\Phi$ and $\hat{\mathbf{n}}_{\mathrm{GB}}$ are the same as those in Ch. 9.4.4. Although γ_{GB} differs in this case, the results from Ch. 9.4.5 for fully faceted crystals apply to this chapter. Hence, configurations producing energetic extrema for $\mathcal{W}_{\mathrm{cube}}^{\mathrm{cube}}$ tend to produce extrema of the opposite sense in $\mathcal{W}_{\mathrm{oct}}^{\mathrm{oct}}$ and $\mathcal{W}_{\mathrm{Toct}}^{\mathrm{Toct}}$. From results presented here, $\mathcal{W}_{\mathrm{cube}}^{\mathrm{cube}}$ boundary particles tend to modify $\mathcal{W}_{\mathrm{GB}}$ to resemble the intersection of two octahedra misoriented by $\vec{\mathbf{R}}_\Phi$—this is an octagonal dipyramid—as in [107]. The anisotropy in configurational free energy imposed by $\mathcal{W}_{\mathrm{oct}}^{\mathrm{oct}}$ and $\mathcal{W}_{\mathrm{Toct}}^{\mathrm{Toct}}$, on the other hand, transforms $\mathcal{W}_{\mathrm{GB}}$ into a shape resembling an octagonal prism of height proportional to the total interfacial free energy configurations of particles at the twist boundaries.

The results of this chapter imply that a balance of tensions, which shows that isotropic boundaries meeting at a triple junction must be separated by dihedral angles of 120°, must be replaced with Herring's formula [120] (or a $\vec{\xi}$–triangle [77]) to account for particle-induced γ_{GB} anisotropy in $\hat{\mathbf{n}}_{\mathrm{GB}}$. As shown by King [95], grain boundary anisotropy could lead to transitions in properties at the triple junction, giving, *e.g.*, measurable changes in segregation or junction mobility.

Part IV

Conclusions and Future Directions

Chapter 12

Summary of Contributions

This work uses calculations that approximate equilibrium configurations at fixed T, $\vec{\mu}$, and particle volume to demonstrate the effect of crystallography on the configurational stability of boundaries that contain boundary particles. The calculations account for the average boundary orientation ($\hat{\mathbf{n}}_{\mathrm{B}}$), the crystallographic misorientation across the boundary ($\vec{\mathbf{R}}_{\Phi}$), and the equilibrium particle interface and boundary free energy densities. Equilibrium orientations are obtained from (1) the Wulff shapes ($\mathcal{W}$) corresponding to the particle fully embedded within the each grain or phase abutting at the boundary and (2) the Wulff shape of the boundary ($\mathcal{W}^{\mathrm{B}}$).

The state of knowledge prior to this work is summarized in Part I. There, known constructions are shown for free particles and particles attached to various non-deformable boundaries that give configurations where a boundary remains unaltered aside from a reduction in its total area. The applicability of a classic study of deformable boundaries is addressed analytically in $\mathbf{R^2}$ and numerically in $\mathbf{R^3}$ to consider the effect of a one facet, and sets of parallel facets in a particle shape otherwise described as the abutment of two equivalent spherical caps, is discussed. Part I concludes that there is no known geometric construction for faceted boundary particles in $\mathbf{R^3}$ because one does not generally know *a priori* the equilibrium form of the boundary generated by a convexified γ.

The construction presented in Ch. 5.3 of Part II for $\mathbf{R^2}$ is a extension of ideas of C.A. Johnson [85] for twin boundaries that was later utilized by Hoffman and

Cahn [77] and reformulated for general boundaries by Lee and Aaronson [56]. In Part II, the construction is applied to general cases with the assumption of a boundary that is infinite in extent (*i.e.*, very small particles), and perfect wetting and unique boundary displacements in $\mathbf{R^2}$ are identified.

This thesis develops a numerical framework to determine the equilibrium configuration for anisotropic boundary particles attached to general boundaries (Part II, Chs. 6.1–6.4). The methods specify boundary character with $\vec{\mathbf{R}}_\Phi$, $\hat{\mathbf{n}}_\mathrm{B}$, and the Wulff shape of the boundary, $\mathcal{W}^\mathrm{B}$. In most calculations, a sphere was assigned as the boundary Wulff shape to isolate the effect of particle anisotropy. Particle character is specified by the set of particle Wulff shapes (with energy densities expressed relative to $\mathcal{W}^\mathrm{B}$) belonging to the abutting grains or phases.

Surface Evolver is used to minimize the total interfacial free energy under assumed isothermal conditions for a specified volume, $\vec{\mathbf{R}}_\Phi$, $\hat{\mathbf{n}}_\mathrm{B}$, and set of $\mathcal{W}$. The equilibrium configurations that result show faceting to alter boundary geometry when the triple line has components parallel to $\hat{\mathbf{n}}_{GB}^{avg}$. The methods can be extended to systems imposing further geometric and energetic constraints, *e.g.*, particles attached to triple junctions (Ch. 9.4.6) and quadruple points, particles attached to anisotropic boundaries (Ch. 10), and particles relaxing geometric constraints such as $\hat{\mathbf{n}}_\mathrm{B}$. The methods can also be simplified to calculate unattached particle shapes ($\mathcal{W}$) and boundaries without particles (Ch. 7) as well as, *e.g.*, Winterbottom and Summertop shapes (Ch. 3).

Part III of this work applies the methods developed in Part II to problems integral to microstructure. Results from Ch. 9–10 show that boundary geometry can be used to control heterogeneous nucleation textures, and preferred nucleation sites are strongly dependent on boundary and particle $\mathcal{W}$.

Boundary character has greater influence when $\Delta\gamma_{\mathrm{B}-\mathrm{P}}$ is relatively small. As $\Delta\gamma_{\mathrm{B}-\mathrm{P}}$ is decreased, particle faceting becomes less advantageous at those sites (described by $\hat{\mathbf{n}}_\mathrm{B}$ and $\vec{\mathbf{R}}_\Phi$) giving the largest boundary distortions. When γ_B is similar to the facet free energy densities, large boundary distortions can suppress faceting, and isotropic or partially isotropic boundary particles will then be more prevalent. When γ_B is large, particles may anticoarsen to maximize replaced boundary energy and preferentially align to minimize boundary distortion (Ch. 11.1).

Chapter 11.2 shows that faceting can alter microstructural stability and bound-

ary structure. In particular, when $\hat{\mathbf{n}}_B$ is fixed, grain boundary particles can exert a torque on grains abutting to form a boundary. When grain rotations are constrained, a boundary particle that can reduce its interfacial free energy by changing grain misorientation could influence the orientation of recrystallizing grains that nucleate at the particle interface or particle-boundary triple line. Similarly, when $\vec{\mathbf{R}}_\Phi$ is fixed, boundary particles can exert a torque on the boundary to which they are attached. In both torque examples, particles can affect microstructural changes.

Chapter 13

Conclusions

1. A geometric construction can be used to determine the equilibrium boundary particle shape in $\mathbf{R^2}$. Results from the construction indicate that geometric constraints imposed by the particle can force the boundary to be noncolinear across the particle and that the relative boundary free energy is not always evident from the boundary particle shape.

2. Boundary particle shape in $\mathbf{R^3}$ can be determined numerically when the Wulff shape of the particle within each grain abutting the boundary, the Wulff shape of the boundary, the crystallographic misorientation across the boundary, and the inclination of the boundary are known.

3. At equilibrium, the triple line between the boundary and particle interfaces is generally nonplanar and requires that the boundary rumple around the particle. The boundary will attach to this triple line and assume a shape that gives a constant weighted mean curvature of zero.

4. In $\mathbf{R^2}$ and $\mathbf{R^3}$, the equilibrium configurations contain only those portions of particle interface that appear on the particle Wulff shapes and those portions of boundary that appear on the boundary Wulff shape.

5. Results in $\mathbf{R^3}$ show that, although anisotropic boundary particles may cause a boundary to rumple and reduce the boundary energy that would otherwise be removed, the nucleation rate of the anisotropic particles will exceed that

of isotropic particles with dihedral angles greater than $2\theta_L$. Hence, in cases where $\gamma(\mathcal{W}^{\text{sphere}})$ is relatively large, there may be a high probability of modifications to boundary shape through boundary particle nucleation.

6. When the boundary is anisotropic, boundaries with orientations near facets on the boundary $\mathcal{W}$ may facet in the absence of a boundary particle. The boundaries remain faceted in the presence of a boundary particle, but the details of the faceting are altered.

7. Both isotropic and anisotropic boundary particles may induce boundary faceting.

8. There are a number of ways that boundary particles may interact to reduce interfacial free energy. For instance, particles may coarsen or anticoarsen and spatially arrange to minimize boundary distortion. When there are constraints requiring the particle to adopt a spherical cap in one grain, the particle will place the spherical cap in the appropriate grain to produce the energy-minimizing shape.

9. Boundary particles can exert torques tending to rotate a grain or reorient a grain boundary.

Chapter 14

Directions for Future Research

14.1 Simplification of the Numerical Methods

Because particles that have a crystalline structure are frequently anisotropic, realistic models utilize anisotropic interfacial free energy densities to account for faceted geometries. Currently, the methods introduced in Part II of this thesis—*i.e.*, HD1 functions of general $\gamma(\hat{\mathbf{n}})$ producing the desired $\mathcal{W}$ and the rotation matrices orienting the $\mathcal{W}$ with respect to the crystallographic reference frame—must be formulated on a case-by-case basis.

It will be useful to develop an algorithm that integrates the methods into *Surface Evolver* to render a convenient model accessible to members of the general science and mathematics community. The proposed model will take: (1) symmetry and relative interfacial free energy densities of equilibrium interface to construct the $\gamma^{convex}(\mathcal{W})$ that describe the equilibrium (a) particle shapes embedded within each grain or phase and (b) boundary shape, and (2) the geometry the boundary ($\hat{\mathbf{n}}_{\mathrm{B}}^{avg}$, $\vec{\mathbf{R}}_{\Phi}$). The model will be extended to account for boundary intersections (*e.g.*, triple junctions). A simplified *Evolver* scheme will facilitate research in a number of other problems related to boundaries and boundary particles.

14.2 Calculations for Real Systems

14.2.1 Observed Boundary Energies

Boundary free energy minima have been identified for several materials systems with fixed $\hat{\mathbf{n}}_{\mathrm{B}}$ for particular $\vec{\mathbf{R}}_{\Phi}$ about a given axis [121] and general boundary geometries through through statistical analyses [5, 6, 7, 122] suggested by Shewmon [123] that correlate boundary energy to (frequency of occurrence)$^{-1}$. Although observed boundary orientations generally result from facets of growth shapes that have impinged and the inverse correlation is not exact, growth by extension normal to larger energy facets tends to occur more rapidly, thereby eliminating these high energy orientations from a growing shape [61, 124]. In addition, there are recent indications that boundary energy is proportional to the surface free energy of impinging grain orientations [122].

Direct application of a statistical analysis of observations accounts for, *e.g.*, the absence of boundary geometries predicted from simple boundary models but inhibited due to repulsions between like charges in ionic crystals [121]. Chapter 10 applies the Read Shockley model for low angle grain boundary free energies to calculate anisotropic $\mathcal{W}_{\mathrm{GB}}$. Application of anisotropic $\gamma^{convex}(\mathcal{W}_{\mathrm{GB}})$ derived from observations of boundaries would enable another method of analysis/prediction of boundary configurations for real systems.

14.2.2 Particles with Internal Interfaces

Analytic constructions for anisotropic particles with internal twin boundaries have been considered for free particles of Au [93] and particles attached to boundaries [77, 85] in dilute Pb-Al [50] and Pb-Si [47] alloys. Re-entrant interfaces, which give a particle shape that is non-convex, have been observed for both particle types and identified as equilibrium features [47, 93].

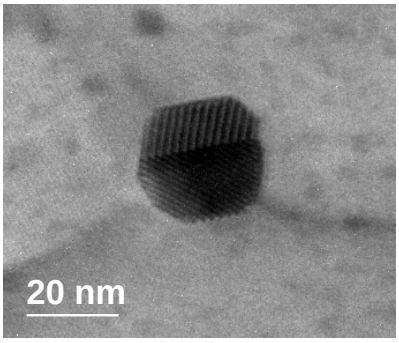

Figure 14.1: Bicrystalline particle of Pb in Al. *(Courtesy of Lihua Zhang, NCEM, LBNL.)*

In addition to the crystallographic misorientation across an internal boundary, the equilibrium shapes of particles with internal boundaries could be calculated with: (1) the average internal boundary orientation, (2) the equilibrium internal boundary orientations and their relative interfacial free energy densities, and (3) the relative amount of particle volume to each side of the internal boundary. Calculations could give both free particles with internal boundaries and particles with internal boundaries attached to external boundaries (*e.g.*, bicrystalline particles at grain boundaries).

14.3 Calculations for Evolving Systems

14.3.1 Limiting Growth Shapes

Particle growth shapes in real systems frequently consist of equilibrium interface in proportions determined by growth kinetics rather than minimization in interfacial free energy. Shape changes governed by a growth velocity, $V(\hat{\mathbf{n}})$, that is anisotropic in the orientation of particle interface give a limiting growth shape that can be determined with the proper formulation of $V(\hat{\mathbf{n}})$ [124].

The boundary geometries calculated in this work assume that configurations are allowed to equilibrate and are thus independent of growth velocity. By default, shape calculations with *Evolver* take mobility as isotropic during and evolution. It is possible [97], however, to define an anisotropic mobility tensor that would give the $V(\hat{\mathbf{n}})$ producing the limiting growth shape of a boundary particle. There are examples [124] demonstrating the formulation of $V(\hat{\mathbf{n}})$ for recrystallization in a number of cubic materials systems.

14.3.2 Metastable Shapes

Metastable particle shapes with steps, kinks, and terraces are frequently observed (Fig. 14.2). Particles in dilute Pb-Al alloys are sometimes found to be "kinetically limited" [125]. The nucleation of steps [126] and the evolution of stepped structures [62] under volume-conserving motions have been studied to determine whether a crystal (of constant volume) will be able to reach an equilibrium shape.

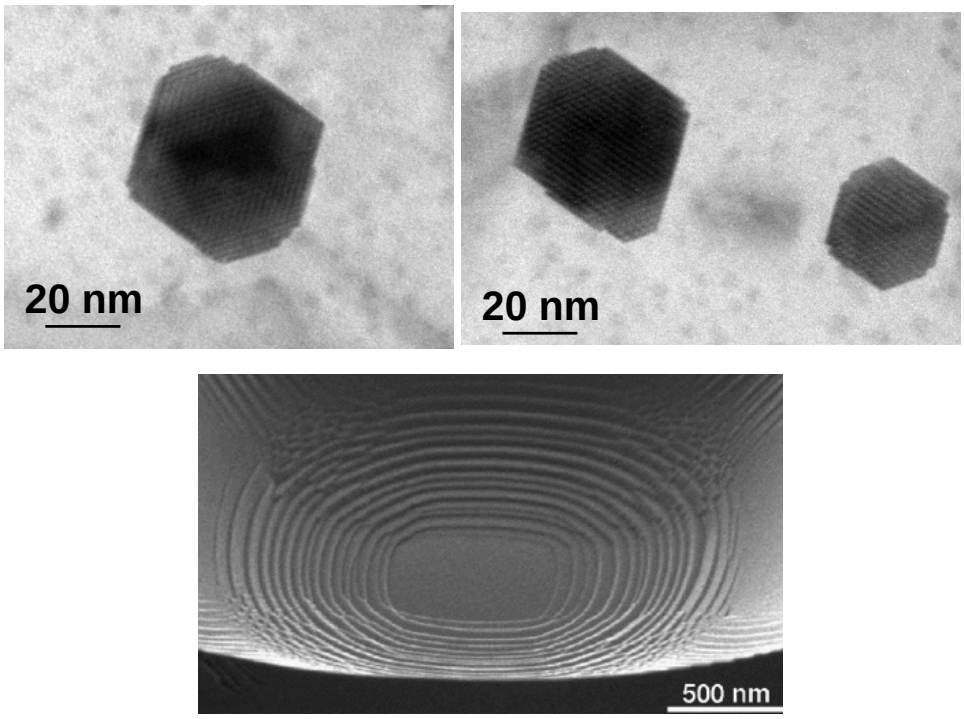

Figure 14.2: Top: Metastable stepped structures of Pb in Al *(Courtesy of Lihua Zhang, NCEM, LBNL)*; Bottom: Metastable UO_2 structure formed by the intersection of one stepped $\{100\}$ and four stepped $\{111\}$ facets [40].

Metastable boundary particles can be introduced into structures calculated as in Part II with the aid of large perturbations or through surface energy minimizations that do not employ the numerical trick discussed in Ch. 6.1 to gradually transform an isotropic shape into an anisotropic one. Steps can be frozen in by reducing the mesh size (increasing the number of vertices) so that the average distance between vertices of the mesh is much smaller than the average height of the steps created. The results could be used as a starting configurations of stepped particle shapes attached to boundaries for calculations as in [62].

14.3.3 Boundary Pinning

Smith [4] demonstrated the effect of grain topology on microstructural evolution, showing large grains with many sides to grow at the expense of smaller grains. Grain growth is often limited (and can thus be controlled by) boundary particles that remove boundary energy and are often approximated as immobile spheres [68].

The effect of particle faceting on the drag force exerted by immobile particles is a natural extension of this work. Calculations of the variation in this force with boundary character for a given set of particle $\mathcal{W}$ could be performed by constraining the boundary to have a non-zero constant mean curvature (*i.e.*, to establish a difference in pressure across the boundary).

There are a number of variations to this problem. For particles with shapes evolving under surface diffusion that are large or attached to boundaries of high curvature, particle shape changes, which scale as TIME^4 [104], might not occur as the triple junction between the particle and boundary moves. Moreover, the nucleation barrier for a facet step [126], as for precipitates in steel [70], can be so large as to inhibit changes to particle shape. Hence, immobile anisotropic particles may not form equilibrium $\mathcal{W}$ in the growing grain, an issue that does not arise when considering spherical particles.

The drag force exerted by particles that do not change shape are expected to be different from those that do. At small boundary velocities, immobile particles could take a sequence of equilibrium shapes dependent on the instantaneous boundary shape. Such cases might occur when many small particles intersect a large area

fraction of the moving boundary, slowing grain growth.

A more difficult case, studied rigorously for isotropic pores in sintering systems [69] and for general systems [127], allows boundary particles to move with the boundary but at a reduced velocity. This case is more difficult because particle shape is typically metastable at a given point in time, and it is not presently clear how to approximate the shape. Metastability drives the atom flux which reshapes and repositions the particle as the boundary moves. The particle breaks away from the boundary when the boundary mobility is greater than that of the particle [69].

It has been shown [127] that particle mobility is dependent on particle size, and a distribution of particle mobilities controls limiting grain size. Hence, when combined with results for heterogeneous nucleation textures, an analysis of the variation in drag force with boundary character could be used to indicate what character of boundaries in a given materials system would be desirable for, *e.g.*, retaining small grain sizes to achieve higher yield strength.

14.3.4 Ductile Fracture

The ideal strength of a material is rarely achieved due to structural inhomogeneities such as dislocations, grain boundaries, and small particles. Fracture, which occurs when a material breaks into one or more parts due to an applied load, typically occurs at stresses dependent on the type, arrangement, and number of inhomogeneities as well as the geometry of the loading. Ductile fracture occurs when there is measurable plastic deformation prior to the breakage [128].

Ductile fracture can result from the nucleation, growth, and coalescence of voids at a particle. In such a case, details (*e.g.*, onset) of the fracture are dependent on the elastic properties of the particle as well as its shape [129]—for instance, elongated carbide and sulfide particles in some steels can produce elongated voids that coalesce to form sheets under a load [130, 131, 132, 133]. Void nucleation tends to occur most easily at particles attached to grain and phase boundaries within materials [134, 135]. However, when the boundary particles are faceted, the relationship between shape and void nucleation is not clear.

To analyze the effect of boundary particle anisotropy on void nucleation in ductile fracture, fracture tests on specimens for which the shape of boundary par-

ticles can be determined are necessary. Boundary particle shape is dependent on boundary geometry as well as the equilibrium boundary and facet free energies. Scanning electron microscopy (SEM) can be used to examine fracture surfaces following fracture tests to determine the initiation and progression of failure. When the surfaces indicate that fracture began with the nucleation of voids at a grain boundary particle, a characterization of that boundary's geometry—*i.e.*, the crystallographic misorientation across and inclination of the boundary plane, obtained with electron back-scattered diffraction and microsectioning [122, 136]—will be necessary to reconstructing the particle shape.

The results will reveal the relationship between the initiation of fracture and the precise boundary particle geometry. The relationship between fracture and slight variations to a *specific* type of boundary particle (*e.g.*, particles attached to a pure 45° twist grain boundary with different inclinations of the boundary plane) is not possible with the post-fracture boundary characterizations above. For this reason, it will be useful to investigate methods of obtaining textured specimens with a given type of boundary and/or methods of testing specimens (such as thin films and wafer-bonded materials) for which the fabrication of bi- and tricrystals with fixed misorientations is relatively simple.

Appendix A

Obtaining Gaussian Curvature from *Surface Evolver* Results

This appendix illustrates how $\mathcal{K}$ was determined at a point on the boundary of an equilibrium configuration calculated with *Evolver*. A quadric surface is fit to the centroids of the elements forming the triangulated surface representing the boundary. For each element M, a local reference frame is defined. The origin of this frame is taken as the centroid P to the element, and the z–axis is taken parallel to the unit normal to the element at P.

Surface curvature at P is then obtained from the coefficients a, b, and c of the explicit form of the resultant quadric surface

$$z(x,y) = ax^2 + by^2 + cxy \tag{A.1}$$

The coefficients are determined from the three exterior vertices $v_i = (x_i, y_i, z_i)$ of the triangle elements sharing edges with M. These vertices provide a measure of the local deviation of the surface from its tangent plane at P, and thereby give a measure of the surface curvature at P.

Substitution of vertex positions into Eq. (A.1) gives three equations with three unknowns. The unknowns can be determined through Cramer's method, and $\mathcal{K}$ is

then

$$\mathcal{K} = 4ab - c^2 \qquad \text{(A.2)}$$

Appendix B

Rodrigues Rotation Matrices in *Surface Evolver*

Consider the triangular element M of particle interface defined by the vertices $\vec{\mathbf{v}}_{M,i} = (x_{M,i},\, y_{M,i},\, z_{M,i})$ taken relative to the *Evolver* coordinate system. Edges connecting vertices are specified by the vectors $\vec{\mathbf{l}}_{M,ij} = \vec{\mathbf{v}}_{M,j} - \vec{\mathbf{v}}_{M,i}$. Triangular element M acts as the tangent plane to the surface at a point, converging to the surface of interest as the area of the element, $\vec{\mathbf{A}}_M = \left(\vec{\mathbf{l}}_{M,ij} \times \vec{\mathbf{l}}_{M,ik}\right)/2$, shrinks to zero.

The unit normal to the element, pointing from the particle into the embedding grain, is

$$\hat{\mathbf{n}}_M = \frac{\vec{\mathbf{l}}_{M,ij} \times \vec{\mathbf{l}}_{M,ik}}{||\vec{\mathbf{l}}_{M,ij} \times \vec{\mathbf{l}}_{M,ik}||}$$

The orientation of element M relative to the *Evolver* reference frame is specified by a 3×3 Rodrigues rotation matrix,

$$\vec{\mathbf{R}}_\Phi = \begin{bmatrix} \cos\Phi(1-r_1^2)+r_1^2 & r_1r_2(1-\cos\Phi)+r_3\sin\Phi & r_1r_3(1-\cos\Phi)-r_2\sin\Phi \\ r_1r_2(1-\cos\Phi)-r_3\sin\Phi & \cos\Phi(1-r_2^2)+r_2^2 & r_2r_3(1-\cos\Phi)+r_1\sin\Phi \\ r_1r_3(1-\cos\Phi)+r_2\sin\Phi & r_2r_3(1-\cos\Phi)-r_1\sin\Phi & \cos\Phi(1-r_3^2)+r_3^2 \end{bmatrix}$$

and for convenience, $\vec{\mathbf{R}}_\Phi$ is denoted $\Phi\langle r_1, r_2, r_3\rangle$.

Grain misorientation angle Φ was set in terms of *Evolver's* coordinate system by applying a rotation matrix of the form $\vec{\mathbf{R}}_\Phi$ to the unit normal components of the

interfacial free energy function describing particle shape in one grain, *e.g.*, grain C_2

$$\gamma_{C_2}(\hat{\mathbf{n}}') = \gamma_{C_2}\left(\vec{\mathbf{R}}_{\Phi}\hat{\mathbf{n}}\right) \tag{B.1}$$

Boundary inclination was then accounted for by applying a second rotation matrix $\vec{\mathbf{R}}_{\Theta} = \Theta < t_1, t_2, t_3 >$ to the normal components of the interfacial energy functions in both grains C_1 and C_2 to incline the particle shape with respect to the boundary

$$\gamma_{C_1}(\hat{\mathbf{n}}')\,\gamma_{C_2}(\hat{\mathbf{n}}'') = \gamma_{C_2}\left(\vec{\mathbf{R}}_{\Theta}\vec{\mathbf{R}}_{\Phi}\hat{\mathbf{n}}\right) \tag{B.2}$$

Appendix C

Heterogeneous Nucleation

C.1 Nucleation Barrier and Critical Volume

The nucleation barrier is related to the critical nucleus volume, V^*, through

$$\Delta G^* = -\left(\frac{V^*}{2}\right)\Delta G_V \tag{C.1}$$

where ΔG_V is the chemical driving force per unit volume.

Equation (C.1) can also be written [109]

$$\Delta G^* = -\left(\frac{4}{\Delta G_V^2}\right)V^{\mathcal{W}} \tag{C.2}$$

where $V^{\mathcal{W}}$ is the volume of the Wulff shape.

It follows that, for a fixed ΔG_V, reductions in ΔG^* are linearly related to those in V^*, or, equivalently, in $V^{\mathcal{W}}$.

C.2 Critical Nucleus Size

For nucleation at an interface,

$$\Delta G = \Delta G_V V + \sum_j \gamma(\hat{\mathbf{n}}_j)A_j \tag{C.3}$$

where the first term on the right hand side is the chemical driving force and the second term accounts for changes in interfacial free energy. Equation (C.3) can be rewritten,

$$\Delta G = \Delta G_V V + V^{2/3} \gamma \sum_j w(\hat{\mathbf{n}}_j) \tag{C.4}$$

where $w(\hat{\mathbf{n}}_j)$ is dimensionless and weights orientation j according to its contribution to ΔG.

The critical volume for a stable nucleus is determined by finding the stationary point of the volume derivative of Eq. (C.4), giving

$$V^* = \left(-\frac{2\gamma \sum_j w(\hat{\mathbf{n}}_j)}{3\Delta G_V} \right)^3 \tag{C.5}$$

For a particle embedded in n–dimensions, the critical nucleus size is

$$B^* = \left(-\frac{(n-1)\gamma \sum_j w(\hat{\mathbf{n}}_j)}{n\Delta G_B} \right)^n \tag{C.6}$$

where B^* is an n-dimensional critical volume.

Critical volume is directly dependent on the change in interfacial free energy brought about by the nucleus. For a fixed critical volume B^*, nucleation will favor sites that minimize the necessary driving force

$$-\left(\frac{n}{n-1} \right) \Delta G_B = \frac{\gamma \sum_j w(\hat{\mathbf{n}}_j)}{(B^*)^{1/n}} \tag{C.7}$$

C.3 Chemical Driving Force

Substituting Eq. (C.5) for volume in Eq. (C.4) gives the heterogeneous nucleation barrier,

$$\Delta G^* = \frac{4\gamma^3 (\sum_j w(\hat{\mathbf{n}}_j))^3}{27 \Delta G_v^2} \tag{C.8}$$

Letting $\gamma(\hat{\mathbf{n}}) = \gamma \sum_j w(\hat{\mathbf{n}}_j)$, a constant driving force ΔG_v gives

$$\frac{\Delta G_1^*}{\Delta G_2^*} = \left(\frac{\gamma_1(\hat{\mathbf{n}})}{\gamma_2(\hat{\mathbf{n}})} \right)^3 \tag{C.9}$$

a ratio independent of ΔG_v.

Results in Ch. 9–10 are found with

$$\frac{\Delta G^*_{\mathrm{HET}}(\mathcal{W}^{\text{shape 1}}_{\text{shape 2}})}{\Delta G^*_{\mathrm{HET}}(\mathcal{W}^{\text{sphere}})} = \left(\frac{\gamma(\mathcal{W}^{\text{shape}})}{\gamma(\mathcal{W}^{\text{sphere}})} \right)^3 \tag{C.10}$$

where $\gamma(\mathcal{W}^{\text{shape 1}}_{\text{shape 2}})$ is the total change in interfacial free energy divided by the total change in interfacial area that occurs on attaching a unit volume of particle to a boundary of specified character. The anisotropic particle is described by $\mathcal{W}^{\text{shape 1}}$ to one side of the boundary and $\mathcal{W}^{\text{shape 2}}$ to the other side of the boundary. The isotropic heterogeneous reference is described by $\mathcal{W}^{\text{sphere}}$ on both sides of the boundary.

Appendix D

Wulff Shape Volume

Solving Eq. (C.2) for $V^{\mathcal{W}}$ gives

$$V^{\mathcal{W}} = -\frac{\Delta G^* \Delta G_V^2}{4} \tag{D.1}$$

Substituting Eq. (C.8) into the result gives

$$V^{\mathcal{W}} = \frac{\gamma^3 (\sum_j w(\hat{\mathbf{n}}_j))^3}{27} \tag{D.2}$$

The volume of the Wulff shape in $\mathbf{R}^{\gamma}$ is thus proportional to the cube of the total interfacial free energy of a fixed volume in $\mathbf{R}^{\mathbf{3}}$, or

$$\sqrt[3]{V^{\mathcal{W}}} \propto \Delta E \tag{D.3}$$

where ΔE is taken to be the total interfacial free energy of a particle.

Appendix E

Shape Table

Name	Aspect Ratio, Υ	(unitless volume of 1)		
		A_{100}^{total}	A_{111}^{total}	A^{total}
cube	$1/\sqrt{3} = 0.577$	6	0	6
	0.667	5.56	0.28	5.84
	0.717	5.08	0.61	5.69
cuboctahedron	0.866	3.39	1.95	5.34
	1	2.1	3.15	5.25
	1.155	1.19	4.12	5.31
	1.245	0.82	4.57	5.39
	1.5	0.18	5.44	5.62
octahedron	$\sqrt{3} = 1.732$	0	5.72	5.72

Table E.1: Surface area of a cube, truncated cubes, a cuboctahedron, truncated octahedra, and an octahedron of unit volume. The minimum *surface area* for a unit volume occurs at an aspect ratio, $\Upsilon = \gamma_{100}/\gamma_{111}$, of 1, which corresponds to a truncated octahedron.

Appendix F

Read Shockley

To make Eq. (10.2) HD1 in $\hat{\mathbf{n}}_{\mathrm{GB}}$, $L(\hat{\mathbf{n}}_{\mathrm{GB}})$ was modified

$$L(\hat{\mathbf{n}}_{\mathrm{GB}}) = M(\hat{\mathbf{n}}_{\mathrm{GB}})(D_o - 1) + \frac{1}{\|\hat{\mathbf{n}}_{\mathrm{GB}}\|^2}(n_{gb,1}^2 a_1 + n_{gb,2}^2 a_2) - a_1 \ln\left(\frac{a_1}{\|\hat{\mathbf{n}}_{\mathrm{GB}}\|}\right) - a_2 \ln\left(\frac{a_2}{\|\hat{\mathbf{n}}_{\mathrm{GB}}\|}\right) + \nu n_{gb,3}^2 \left[\frac{1}{a_1}\ln\left(\frac{a_1}{\|\hat{\mathbf{n}}_{\mathrm{GB}}\|}\right) + \frac{1}{a_2}\ln\left(\frac{a_2}{\|\hat{\mathbf{n}}_{\mathrm{GB}}\|}\right)\right] \tag{F.1}$$

Appendix G

Anticoarsening

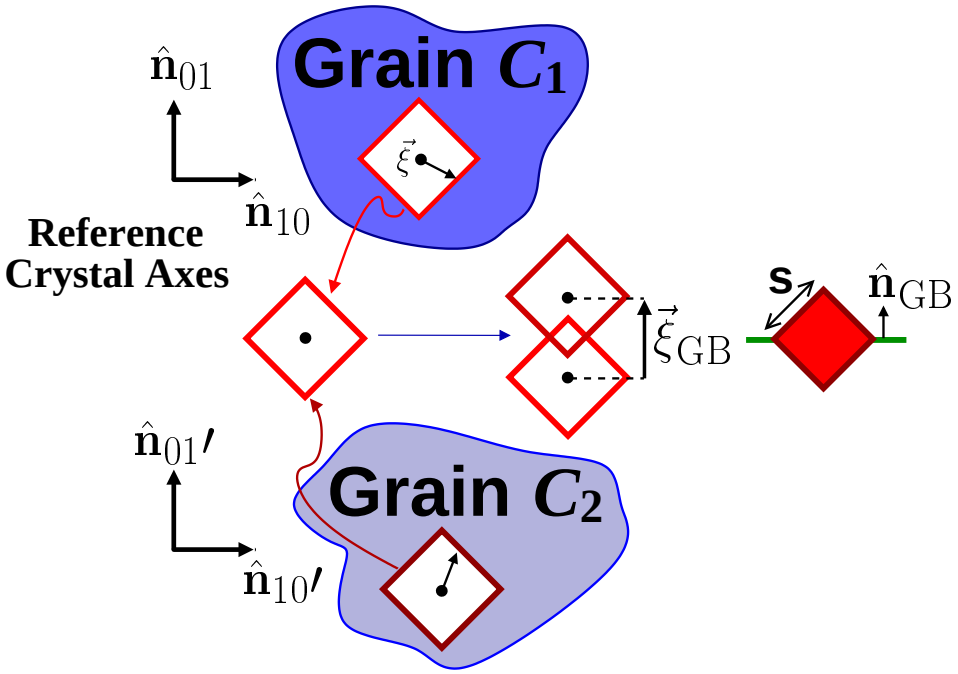

Figure G.1: Interfacial particle construction for $\mathcal{W}^{\text{square}}$ that are similarly oriented for simplicity. The construction gives the same shape for all boundary energies (when non-appearing orientations are given values that approach infinity).

Consider the grain boundary particle in $\mathbf{R^2}$ of fixed area constructed in Fig. G.1. The $\mathcal{W}^{\text{square}}$ used to construct the shape are similarly oriented in C_1 and C_2 for simplicity. Particle shape is independent of γ_{GB} when orientations absent from $\mathcal{W}^{\text{square}}$ have free energies $\to \infty$.

The particle is composed of four sides of equal length, s, and the area of the particle is $A = s^2$. The change in interfacial free energy that occurs when the particle attaches to the grain boundary is

$$\Delta E_1 = s\left(4\gamma(\mathcal{W}^{\text{square}}) - \sqrt{2}\gamma_{\text{GB}}\right) \tag{G.1}$$

The total change in interfacial free energy for two such grain boundary particles, each of side length $s/\sqrt{2}$ and $A = s^2/2$, is

$$\Delta E_2 = 2\frac{s}{\sqrt{2}}\left(4\gamma(\mathcal{W}^{\text{square}}) - \sqrt{2}\gamma_{\text{GB}}\right) \tag{G.2}$$

At a relative boundary free energy of

$$\frac{\gamma_{\text{GB}}}{\gamma(\mathcal{W}^{\text{square}})} > 2\sqrt{2}$$

$\Delta E_2 < \Delta E_1$, and anticoarsening is favorable.

Bibliography

[1] J.W. Gibbs, On the equilibrium of heterogeneous substances (1876), in *Collected Works*, vol. 1. (Longmans, Green, and Co., 1928).

[2] J.W. Cahn, Thermodynamics of solid and fluid interfaces, in *Segregation to Interfaces*, edited by W.C. Johnson and J.M. Blokley (ASM, Metals Park, OH, 1979), pp. 3-23.

[3] J.W. Cahn and J.E. Taylor, Thermodynamic driving forces and equilibrium in multicomponent systems with anisotropic surfaces, in *Mathematics of Microstructure Evolution*, edited by L.Q. Chen, B. Fultz, J.W. Cahn, J.R. Manning, J.E. Morral, and J.A. Simmons (TMS/SIAM, Warrendale, PA, 1996), pp. 149-159.

[4] C.S. Smith, Grain shapes and other metallurgical applications of topology, in *Metal Interfaces* (ASM, Cleveland, 1952), pp. 65-113.

[5] G.S. Rohrer, D.M. Saylor, B. El Dasher, B.L. Adams, A.D. Rollett, and P. Wynblatt, The distribution of internal interfaces in polycrystals, *Z. Metallkd.*, 95(4) (2004) 197-214.

[6] D.M. Saylor, A. Morawiec, and G.S. Rohrer, The relative free energies of grain boundaries in magnesia as a function of five macroscopic parameters, *Acta Mater.*, **51** (2003) 3675-3686.

[7] D.M. Saylor, B. El Dasher, A.D. Rollett, and G.S. Rohrer, The relative free energies of grain boundaries in aluminum as a function of five macroscopic parameters, *Acta Mater.*, **52** (2004) 3649-3655.

[8] G. Wulff, Zur frage der Geschwindigkeit des Wachstums und der Auflosung der Krystalflachen, *Z. Krist. Mineral*, **34** (1901) 449.

[9] W.L. Winterbottom, Equilibrium shape of a small particle in contact with a foreign substrate, *Acta Metall.*, **15** (1967) 303.

[10] E. Johnson, A. Johansen, U. Dahmen, S. Chen, and T. Fujii, Shapes and sizes of nanoscale Pb inclusions in Al, *Mater. Sci. Eng. A—Struct.*, **304-306** (2001) 187-193.

[11] R.S. Nelson, D.J. Mazey, and R.S. Barnes, The equilibrium shape and size of holes in solids, *Philos. Mag.*, **11** (1965) 91-111.

[12] L.E. Murr, *Interfacial Phenomena in Metals and Alloys* (Addison-Wesley, India, 1975), pp. 183-187.

[13] J. Hess, Measurement of solid-solid interfacial energies, in *Metal Interfaces* (ASM, Cleveland, 1952), pp. 134-152.

[14] J.W. Cahn and W.C. Carter, Crystal shapes and phase equilibria: A common mathematical basis, *Metall. Mater. Trans. A*, **27**(6) (1996) 1431.

[15] C.V. Boys, *Soap bubbles and the forces which mould them* (Doubleday, Garden City, New York, 1959).

[16] E.L. Thomas, D.M. Anderson, C.S. Henkee, and D. Hoffman, Periodic area-minimizing surfaces in block copolymers, *Nature*, **334**(6183) (1988) 598-601.

[17] V. Luzzati and P.A. Spegt, Polymorphism of lipids, *Nature*, **215** (1967) 701-704.

[18] A. Ciach and R. Holyst, Periodic surfaces and cubic phases in mixtures of oil, water, and surfactant, *J. Chem. Phys.*, **110**(6) (1999) 3207-3214.

[19] W. Thomson (Lord Kelvin), On the division of space with minimum partition area, *Philos. Mag.*, **25** (1887) 503-514.

[20] F.J. Almgren, Jr. and J.E. Taylor, The geometry of soap films and soap bubbles, *Sci. Am.*, **235**(1) (1976) 82-93.

[21] J.E. Blendell, W.C. Carter, and C.A. Handwerker, Faceting and wetting transitions of anisotropic interfaces and grain boundaries, *J. Am. Ceram. Soc.*, **82**(7) (1999) 1889-1900.

[22] H.U. Hong and S.W. Nam, The occurrence of grain boundary serration and its effect on the $M_{23}C_6$ carbide characteristics in an AISI 316 stainless steel, *Mater. Sci. Eng. A—Struct.*, **332** (2002) 255-261.

[23] S.B. Lee, W. Sigle, W. Kurtz, and M. Rüle, Temperature dependence of faceting in $\Sigma 5(310)[001]$ grain boundary of $SrTiO_3$, *Acta Mater.*, **51**(4) (2003) 975-981.

[24] C. Herring, Some theorems on the free energy of crystal surfaces, *Phys. Rev.*, **82**(1) (1951) 87-93.

[25] J.E. Taylor, Crystalline variational problems, *Bull. Am. Math. Soc.*, **84** (1978) 568-588.

[26] J.W. Cahn, Transitions and phase-equilibria among grain-boundary structures, *J. Phys.—Paris*, **43**(NC-6) (1982) 199-213.

[27] T. Young, An essay on the cohesion of fluids, *Philos. T. Roy. Soc. A*, **95** (1805) 65-87.

[28] P.S. de Laplace, *Mechanique Celeste*, (Supll. au X Livre, Impr. Imperiale, Paris, 1805).

[29] J.E. Taylor, Mean curvature and weighted mean curvature, *Acta Metall. Mater.*, **40** (1992) 1475-1485.

[30] E.J. Siem and W.C. Carter, The stability of several triply periodic surfaces, *Interface Sci.*, **10** (2002) 287-296.

[31] W. Beere, A unifying theory of the stability of penetrating liquid phases and sintering pores. *Acta Metall.*, **23** (1975) 131-138.

[32] W. Beere, Sintering kinetics of powder compacts *Acta Metall.*, **23** (1975) 139-145.

[33] R. Riedel, H. Zipse, and J. Svoboda, Equilibrium pore surfaces, sintering stresses and constitutive equations for the intermediate and late stages of sintering. II. Diffusional densification and creep, *Acta Metall. Mater.*, **42**(2) (1994) 445-452.

[34] C. Templier, H. Garem, J. Grilhe, and J. Delafond, Segregation of xenon implanted in metals—TEM study of the structure of Xe precipitates, C.R. Acad. Sci. II B, **300** (1985) 543-546.

[35] A. vom Felde, J. Fink, T. Mullerheinzerling, J. Pfluger, B. Scheerer, G. Linker, and D. Kaletta, Pressure of neon, argon, and xenon bubbles in aluminum, *Phys. Rev. Lett.*, **53** (1984) 922-925.

[36] J. Arbiol, A. Ruiz, A. Cirera, F. Pèiro, A. Cornet, J.R. Morante, A. Alimoussa, and M.J. Casanove, High resolution electron microscopy analysis of Pt-nanoparticles embedded on crystalline TiO_2, *Inst. Phys. Conf. Ser.*, **169** (2001) 69-72.

[37] B.J. Kooi and J.T.M. de Hosson, Influence of interfacial binding energy and misfit on the shape of the oxide precipitates in metals, *Radiat. Eff. Defect S.*, **156**(1-4) (2001) 19-26.

[38] P. Kopperschmidt, S. Senz, and R. Scholz, Interface defects in integrated hybrid semiconductors by wafer bonding, *Physica B*, **308** (2001) 1205-1208.

[39] V.A. Karachinov, Negative crystals of silicon carbide, *Tech. Phys+.*, **47**(4) (2002) 432-437.

[40] M. Castell, Wulff shape of microscopic voids in UO_2 crystals, *Phys. Rev. B*, **68**(23) (2003) Art. No. 235411.

[41] P.R.F. Barnes, E.W. Wolff, D.C. Mallard, and H.M. Mader, SEM studies of the morphology and chemistry of polar ice, *Microsc. Res. Techniq.*, **62**(1) (2003) 62-69.

[42] J.W. Cahn and J.E. Taylor, A contribution to the theory of surface-energy minimizing shapes, *Scripta Metall.*, **18** (1984) 1117.

[43] E. Bauer, Phänomenologische theorie der kristallabscheidung an oberflächen. II., *Z. Kristallogr.*, **110** (1958) 395-431.

[44] B.E. Sundquist, A direct determination of the anisotropy of the surface free energy of solid gold, silver, copper, nickel, and alpha and gamma iron, *Acta Metall.*, **12** (1964) 67-86.

[45] J.C. Heyraud, J.J. Métois and J.M. Bermond, Surface melting and equilibrium shape: The case of Pb on graphite, *J. Cryst. Growth*, **98** (1989) 355-362.

[46] D. Chatain, V. Ghetta, and P. Wynblatt, Equilibrium shape of copper crystals grown on sapphire, *Interface Sci.*, **12** (2004) 7-18.

[47] S. Hagège Lead inclusions in silicon: Structure, morphology, and thermal behavior, *Interface Sci.*, **7** (1996) 85-101.

[48] D. Chatain, P. Wynblatt, S. Hagège, E.J. Siem, and W.C. Carter, Wetting in multiphase systems with complex geometry, *Interface Sci.*, **9**(3-4) (2001) 191-197.

[49] E. Schroer, S. Hopfe, P. Werner, U. Gösele, G. Duscher, M. Rühle, and T.Y. Tan, Oxide precipitation at silicon grain boundaries, *Appl. Phys. Lett.*, **70**(3) (1997) 327-329.

[50] E. Johnson, S. Hinderberger, S.Q. Xiao, U. Dahmen, and A. Johansen, Structure and morphology of nanosized lead inclusions in aluminum grain boundaries, *Interface Sci.*, **3** (1996) 279-288.

[51] K.N. Tu and D. Turnbull, Morphology of cellular precipitation of tin from lead–tin bicrystals—II, *Acta Metall.*, **15** (1967) 1317-1323.

[52] C.W. Allen, M. Song, K. Furuya, R.C. Birtcher, K. Mitsuishi, and U. Dahmen, Xe precipitates at grain boundaries in Al under 1 MeV electron irradiation, *J. Electron Micros.*, **48**(5) (1999) 503-505.

[53] J.K. Lee, D.W. Dooley, D.E. Graham, S.P. Clough, C.L. White, and H.I. Aaronson, Two families of analytic γ-plots and their influence upon homogeneous nucleation kinetics, *Surf. Sci.*, **62** (1977) 695-706.

[54] G.J. Shiflet, K.C. Russell, and H.I. Aaronson, Homogeneous nucleation kinetics of parallelepipeds, *Surf. Sci.*, **62** (1977) 303-307.

[55] J.W. Cahn and J.E. Taylor, Theory of orientation textures due to surface energy anisotropies, in *Microstructural Science for Thin Film Metallizations in Electronic Applications*, edited by J. Sanchez, D.A. Smith, and N. DeLanerolle (TMS, Warrendale, PA, 1988), pp. 73-77.

[56] J.K. Lee and H.I. Aaronson, Influence of faceting upon equilibrium shape of nuclei at grain boundaries. 1. Two-dimensions, *Acta Metall.*, **23** (1975) 799.

[57] J.K. Lee and H.I. Aaronson, Influence of faceting upon equilibrium shape of nuclei at grain boundaries. 2. Three-dimensions, *Acta Metall.*, **23** (1975) 809.

[58] H.I. Aaronson, M.R. Plichta, G.W. Franti, and K.C. Russell, Precipitation at interphase boundaries, *Metall. Trans. A*, **9** (1978) 363-371.

[59] J.K. Lee, J.H. Choy, and Y. Choi, Equilibrium shape and heterogeneous nucleation barrier at spherical interfaces, *Surf. Sci.*, **256** (1991) 147-158.

[60] K.C. Russell, Nucleation in solids: The induction and steady state effects, *Adv. Colloid Interfac.*, **13** (1980) 205-318.

[61] W.W. Mullins, Morphologies governed by capillarity, in *Metal Surfaces, Structure, Energetics, and Kinetics* (ASM, Cleveland, 1963), pp. 17-66.

[62] W.C. Carter, A.R. Roosen, J.W. Cahn, and J.E. Taylor, Shape evolution by surface diffusion and surface attachment limited kinetics on completely faceted surfaces, *Acta Metall. Mater.*, **43**(12) (1995) 4309-4323.

[63] J.E. Taylor, J.W. Cahn, and C.A. Handwerker, Geometric models of crystal growth, *Acta Metall. Mater.*, **49** (1992) 1443-1474.

[64] J.E. Taylor, Thermodynamic driving forces and interface motion, *J. Mater.*, **48**(12) (1996) 19-22.

[65] W.C. Carter, J.E. Taylor, and J.W. Cahn, Variational methods for microstructural-evolution theories, *J. Mater.*, **49**(12) (1997) 30-36.

[66] A.H. Geisler, Phase transformations at interfaces, in *Metal Interfaces* (ASM, Cleveland, 1952), pp. 269-298.

[67] J.W. Cahn, The kinetics of grain boundary nucleated reactions, *Acta Metall.*, **4** (1956) 449-459.

[68] C.S. Smith (quoting C. Zener), Grains, phases, and interactions: An interpretation of microstructure, *Trans. Metall. Soc. AIME*, **175** (1948) 15-51.

[69] C.H. Hsueh, A.G. Evans, and R.L. Coble, Microstructure development during final intermediate stage sintering, 1. Pore grain-boundary separation, *Acta Metall. Mater.*, **30**(7) (1982) 1269.

[70] R.A. Ricks and P.R. Howell, Bowing mechanism for interphase boundary migration in alloy steels, *Met. Sci.*, **16** (1982) 317-321.

[71] W.F. Lange, III, M. Enomoto, and H.I. Aaronson, Precipitate nucleation kinetics at grain boundaries, *Int. Mater. Rev.*, **34**(3) (1989) 125-150.

[72] J.J. Koenderink, *Solid Shape* (MIT Press, Cambridge, 1990).

[73] A. Dinghas, Über einen geometrischen Satz von Wulff für die Gleichgewichtsform von Kristallen, *Z. Kristollogr.*, **150** (1944) 304-314.

[74] H. Busemann, The isoperimetric problem for Minkowski area, *Am. J. Math.*, **71** (1949) 743-762.

[75] I. Fonseca and S. Müller, A uniqueness proof for the Wulff theorem, *Proc. R. Soc. Edin. A—Ma.*, **119**(1-2) (1991) 125-136.

[76] F.C. Frank, The geometrical thermodynamics of surfaces, in *Metal Surfaces, Structure, Energetics, and Kinetics* (ASM, Cleveland, 1963), pp. 1-15.

[77] D.W. Hoffman and J.W. Cahn, Vector thermodynamics for anisotropic surfaces. I. Fundamentals and applications to plane surface junctions, *Surf. Sci.*, **31** (1972) 368-388.

[78] J.W. Cahn and D.W. Hoffman, Vector thermodynamics for anisotropic surfaces. II. Curved and faceted surfaces, *Acta Metall.*, **22** (1974) 1205-1214.

[79] R. Kaischew, Thermodynamik von kristallkeimen, *B. Bulg. Acad. Sci. Phys.*, **1** (1950) 100; **2** (1951) 191-203.

[80] E. Bauer, Phänomenologische theorie der kristallabscheidung an oberflächen. I., *Z. Kristallogr.*, **110** (1958) 372-394.

[81] Zenodorus, Greek, $\sim$ 200-140 BC.

[82] R.K.P. Zia, J.E. Avron, and J.E. Taylor, The summertop construction: Crystals in a corner, *J. Stat. Phys.*, **50**(3-4) (1988) 727-736.

[83] J. Rankin, *In-situ* heating of nanosized ZrO_2, *J. Am. Ceram. Soc.*, **82**(6) (1999) 1560-1564.

[84] I. Korczagin, S. Golze, M.A. Hempenius, and G.J. Vansco, Surface micropatterning and lithography with poly(ferrocenylmethylphenylsilane), *Chem. Mater*, **15** (2003) 3663-3668.

[85] C.A. Johnson, Some deductions from Wulff's theorem, *Phys. Abs.*, **73** (1970) 3492.

[86] J.R. Bradley and H.I. Aaronson, The stereology of grain boundary allotriomorphs, *Metall. Trans. A*, **8**(2) (1977) 317-322.

[87] R.K.P. Zia, Equilibrium shapes of droplets across grain boundaries, *Physica A*, **251**(1-2) (1998) 40-51.

[88] D. Wolf and K.L. Merkle, Correlation between the structure and energy of grain boundaries in metals, in *Materials Interfaces: Atomic-Level Structure and Properties*, edited by D. Wolf and S. Yip (Chapman & Hall, New York, 1992) pp. 87-150.

[89] J. Kelley, Edge- and surface-energy minimizing crystalline structures, Ph.D. dissertation, Rutgers University, 1996.

[90] I.N. Stranski, Forms of equilibrium crystals, *Discuss. Faraday Soc.*, **5** (1949) 13-21.

[91] L.D. Marks, Particle size effects on Wulff constructions, *Surf. Sci.*, **150** (1985) 358-366.

[92] H. Udin, Measurement of solid:gas and solid:liquid interfacial energies, in *Metal Interfaces* (ASM, Cleveland, 1952), pp. 114-133.

[93] L.D. Marks, Modified Wulff constructions for twinned particles, *J. Cryst. Growth*, **61** (1983) 556-564.

[94] F.M. Orr, L.E. Scriven, T.Y. and Chu, Menisci around plates and pins dipped in liquid: Interpretation of Wilhelmy plate and solderability measurements, *J. Colloid Interface Sci.*, **60** (1977) 402-405.

[95] A.H. King, The geometric and thermodynamic properties of grain boundary junctions, *Interface Sci.*, **7** 251-271 (1999).

[96] F. Almgren and J.E. Taylor, Optimal geometry in equilibrium and growth, *Fractals*, **3** (1995) 713-723.

[97] K.A. Brakke, The surface evolver, *Exp. Math.*, **1**(2) (1992) 141-165; `http://www.susqu.edu/facstaff/b/brakke/evolver`, Source code and manual freely available.

[98] W.C. Carter, Surface evolver as a tool for materials science research, in *Mathematics of Microstructure Evolution*, edited by L.Q. Chen, B. Fultz, J.W. Cahn, J.R. Manning, J.E. Morral, and J.A. Simmons (TMS/SIAM, Warrendale, PA, 1996), pp. 1-14.

[99] E.J. Siem, W.C. Carter, and D. Chatain, The equilibrium shape of anisotropic interfacial particles, *Philos. Mag.*, **84**(10) 991-1010 (2004).

[100] E. Johnson, H.H. Andersen, and U. Dahmen, Nanoscale lead and noble gas inclusions in aluminum—structures and properties, *to appear in Microscopy Research and Technique.*

[101] E.J. Siem and W.C. Carter, Orientation–dependent surface tension functions for surface energy minimizing calculations, to appear in the proceedings of Interfaces and Interphase Boundaries 2005, Queen's University, Belfast, June 2005.

[102] J.H. Evans, The formation of high pressure precipitation phases during the implantation of inert gas and other insoluble elements in metals, *Nucl. Instrum. Meth. B*, **18** (1986) 16-23.

[103] A.R. Roosen, R.P. McCormack, and W.C. Carter, Wulffman: A tool for the calculation and display of Wulff shapes, *Comp. Mater. Sci.*, **11**(1) (1998) 16-26;
`http://www.ctcms.nist.gov/wulffman` Source code and manual freely available.

[104] W.W. Mullins, Flattening of a nearly plane solid surface due to capillarity, *J. Appl. Phys.*, **30** (1959) 77-83.

[105] W.A. Miller and G.A. Chadwick, The equilibrium shapes of small liquid droplets in solid-liquid phase mixtures: Metallic h.c.p. and metalloid systems, *Proc. R. Soc. Lon. Ser—A*, **312** (1969) 257-276.

[106] H.I. Aaronson and H.B. Aaron, Initial stages of the cellular reaction, *Metall. Trans.*, **3** (1972) 2743-2756.

[107] J.W. Cahn, Symmetry constraints on the orientation dependence of interfacial properties: The group of the Wulff plot, *J. Phys.—Paris*, **43**(NC-6) (1982) 23-31.

[108] J.F. Nye, *Physical Properties of Crystals* (Oxford University Press, New York, 1985), 20-24.

[109] K.C. Russell, Diffusional nucleation and growth, in *Precipitation Processes in Solids*, edited by K.C. Russell and H.I. Aaronson (AIME, New York, 1978), pp. 31-86.

[110] W.T. Read and W. Shockley, Dislocation models of crystal grain boundaries, *Phys. Rev.*, **78**(2) (1950) 275-289.

[111] H. Brooks, Theory of internal boundaries, in *Metal Interfaces* (ASM, Cleveland, 1952), pp. 20-64.

[112] G. Gjostein and Rhines, Absolute interfacial energies of $[001]$ tilt and twist grain boundaries in copper, *Acta Metall.*, **7** (1959) 319-330.

[113] Y. He, C. Jayaprakash, and C. Rottman, Shapes of grain inclusions in crystals, *Phys. Rev. B*, **32**(2) (1985) 12-22.

[114] J.P. Hirth and J. Lothe, *Theory of Dislocations* (John Wiley & Sons, New York, 1982), pp. 703-746.

[115] C. Rottman, Roughening of low-angle grain boundaries, *Phys. Rev. Lett.*, **57** (1986) 735-739.

[116] S.B. Lee, S.Y. Choi, S.J. Kang, and D.Y. Yoon, TEM observations of singular grain boundaries and their roughening transition in TiO_2-excess $BaTiO_3$, *Z. Metallkd.*, **94**(3) (2003) 193-199.

[117] M. Yamazaki, The effect of two-step solution treatment on the creep rupture properties of a high carbon 18 Cr–12 Ni stainless steel, *J. Jpn. I. Met.*, **30** (1966) 1032-1036.

[118] X.J. Wu, Grain boundary sliding at serrated grain boundaries, *Adv. Perform. Mater.*, **4** (1997) 409-429.

[119] K.E. Harris, V.V. Singh, and A.H. King, Grain rotation in thin films of gold, *Acta mater.*, **46**(8) (1998) 2623-2633.

[120] C. Herring, Surface tension as a motivation for sintering, in *The Physics of Powder Metallurgy*, edited by W.E. Kingston (McGraw-Hill, New York, 1951), pp. 143-179.

[121] P. Chaudhari and W. Matthews, Coincidence twist boundaries between crystals of MgO smoke, *Appl. Phys. Lett.*, **17** (1970) 115-117.

[122] D.M. Saylor, B. El Dasher, Y. Pang, H.M. Miller, P. Wynblatt, A.D. Rollett, and G.S. Rohrer, Habits of grains in dense polycrystalline solids, *J. Am. Ceram. Soc.*, **87**(4) (2004) 724-726.

[123] P.G. Shewmon, in *Recrystallization, Grain Growth, and Textures* (ASM, Metals Park, OH, 1966) p. 165.

[124] W.C. Carter and C.A. Handwerker, Morphology of grain-growth in response to diffusion induced elastic stresses—cubic systems, *Acta Metall. Mater.*, **41**(5) (1993) 1633-1642.

[125] H. Gabrisch, L. Kjeldgaard, E. Johnson, and U. Dahmen, Equilibrium shape and interface roughening of small liquid Pb inclusions in solid Al, *Acta Mater.*, **49** (2001) 4259-4269.

[126] G.S. Rohrer, C.L. Rohrer, and W.W. Mullins Nucleation energy barriers for volume-conserving shape changes of crystals with nonequilibrium morphologies, *J. Am. Ceram. Soc.*, **84**(9) (2001) 2099-2104.

[127] G. Gottstein and L.S. Shvindlerman, Theory of grain-boundary motion in the presence of mobile particles, *Acta Metall. Mater.*, **41** (1993) 3267-3275.

[128] F.A. McClintock and A.S. Argon, *Mechanical Behavior of Materials* (Ceramic Book and Literature Service, India, 1999) p. 518-541.

[129] R. Raj and M.F. Ashby, Grain boundary sliding and diffusional creep, *Metall. Trans.*, **2**(4) (1971) 1113-1127.

[130] J.W. Hancock and A.C. Mackenzie, Mechanisms of ductile failure in high-strength steels subjected to multi-axial stress states, *J. Mech. Phys. Solids*, **24** (1976) 147-160.

[131] W.A. Spitzig, Effect of sulfides and sulfide morphology on anisotropy of tensile ductility and toughness of hot-rolled steels, *Metall. Trans. A*, **14** (1983) 471-484.

[132] S. Lee, J.W. Rhyu, K.M. Cho, and J. Duffy, Dynamic fracture initiation behavior of an HY-100 steel, *Metall. Trans. A*, **24** (1993) 901-912.

[133] D. Chae, D.A. Koss, A.L. Wilson, and P.R. Howell, The effect of microstructural banding on failure initiation of HY-100 steel, *Metall. Mater. Trans. A*, **31** (2000) 995.

[134] T. Pardoen, D. Dumont, A. Deschamps, and V. Brechet, Grain boundary versus transgranular ductile fracture, *J. Mech. Phys. Solids*, **51** (2003) 637-665.

[135] J.R. Weertman, The pursuit of the small: From grain-boundary cavities to nanocrystalline metals, *Mater. Res. Bull.*, **29**(9) (2004) 616-620.

[136] P.A. Davies, M. Novovic, V. Randle, and P. Bowen, Application of electron backscatter diffraction (EBSD) to fracture studies of ferritic steels, *J. Microsc.—Oxford*, **205**(3) (2002) 278-284.

List of Symbols

$\vec{\mathbf{A}} = A\hat{\mathbf{n}}$: area vector

C_1, C_2: crystals 1 and 2 that abut at a boundary

$D(\hat{\mathbf{n}}_{\mathrm{GB}})$: parameter for Read–Shockley model dependent on the dislocation core energy and $\hat{\mathbf{n}}_{\mathrm{GB}}$

D_o: parameter for He *et al.* extension of Read–Shockley model

$E_o(\hat{\mathbf{n}}_{\mathrm{GB}})$: parameter for Read–Shockley model dependent on the elastic constants of a material

G: isotropic shear modulus

$\Delta G^*(\mathcal{W})$: nucleation barrier [J] for shape $\mathcal{W}$ from a simple model using (1) chemical driving force and (2) interfacial free energies

$\Delta G^*_{\mathrm{HOM}}$: homogeneous ΔG^*

$\Delta G^*_{\mathrm{HET}}$: heterogeneous ΔG^*

$\vec{\Gamma} = \langle \Gamma_1, \Gamma_2, \ldots, \Gamma_c \rangle$: surface excess vector for c components

$J^*(\mathcal{W})$: nucleation rate [nuclei/$s \cdot cm^3$] for shape $\mathcal{W}$

$\mathcal{K}$: Gaussian curvature

$L(\hat{\mathbf{n}}_{\mathrm{GB}})$: parameter for He *et al.* extension of Read–Shockley model

Λ: radial distance from center of boundary particle to point on boundary where $\mathcal{K} \sim 0$

$M(\hat{\mathbf{n}}_{\mathrm{GB}})$: parameter for He *et al.* extension of Read–Shockley model

N_{HET}: number of heterogeneous nucleation sites per unite volume

Ω: grand canonical potential

$P(\hat{\mathbf{n}})$: part of HD1 function of $\gamma(\hat{\mathbf{n}})$ used in *Evolver* calculations

Φ: rotation angle for crystallographic misorientation $\vec{\mathbf{R}}_\Phi$

Q: a constant used to specify the relative depth of $\gamma(\hat{\mathbf{n}})$ minima

$\vec{\mathbf{R}}_\Phi$: crystallographic misorientation, $\vec{\mathbf{R}}_\Phi = \Phi\vec{u}$

$\mathbf{R^2}$: two-dimensional space

$\mathbf{R^3}$: three-dimensional space

$\mathbf{R}^\gamma$: interfacial free energy space

$S(\hat{\mathbf{n}})$: part of HD1 function of $\gamma(\hat{\mathbf{n}})$ used in *Evolver* calculations

T: temperature

$T(\hat{\mathbf{n}})$: a function that equates to 1 at the orientation of an interfacial free energy density minmum and 0 at the antipode to a minmum orientation

V: volume

$\mathcal{W}$: the Wulff shape of a material of fixed volume at constant temperature

$\mathcal{W}^{\text{shape}}$: a $\mathcal{W}$ of shape SHAPE

$\mathcal{W}^{\text{shape 1}}_{\text{shape 2}}$: an equilibrium boundary shape formed by the intersection of $\mathcal{W}^{\text{shape 1}}$ and $\mathcal{W}^{\text{shape 2}}$ that reflects the energy and geometry of the boundary

$\Xi(\mathcal{W}/\mathcal{W}^{\text{sphere}})$: value of a function Ξ for shape $\mathcal{W}$ relative to the shape formed by $\mathcal{W}^{\text{sphere}}$ combinations

Z: Zeldovitch non–equilibrium factor

α: anisotropy factor

a_1, a_2: parameters for He *et al.* extension of Read–Shockley model

b: magnitude of isotropic Burger's vector

β^*: rate of atom attachment to a nucleus

$\chi(\hat{\mathbf{n}})$: the distance from the orientation of an interfacial free energy density minimum

$\Delta\gamma_{\text{B}-\text{P}}$: difference between the interfacial free energy of the boundary and lowest-energy facets

$\gamma(\hat{\mathbf{n}})$: interfacial free energy density $[\text{ENERGY}/\text{LENGTH}^d]$ as a function of $\hat{\mathbf{n}}$; d is the dimension of the interface

$\gamma_{\text{B}}(\hat{\mathbf{n}}_{\text{B}})$: γ of a (grain or heterophase) boundary as a function of $\hat{\mathbf{n}}_{\text{B}}$

$\gamma_{\text{GB}}(\hat{\mathbf{n}}_{\text{GB}})$: γ of a grain boundary as a function of $\hat{\mathbf{n}}_{\text{GB}}$

$\gamma(\mathcal{W}^{\text{shape}})$: γ producing $\mathcal{W}^{\text{shape}}$

$\gamma^i(\mathcal{W}^{\text{shape}})$: γ of orientation i on $\mathcal{W}^{\text{shape}}$

$\gamma^{\text{convex}}(\mathcal{W}^{\text{shape}})$: convex γ producing $\mathcal{W}^{\text{shape}}$

k: Boltzmann's constant

κ: mean curvature

κ_γ: weighted mean curvature

$\vec{\mu} = \langle \mu_1, \mu_2, \ldots, \mu_i \rangle$: a vector of length i determined by the number of chemical species in a system and with entries corresponding to the uniform chemical potential of each species

$\hat{\mathbf{n}} = \langle n_1, n_2, n_3 \rangle$: unit normal to an interface

$\hat{\mathbf{n}}_{\text{B}}$: unit normal to a (grain or heterophase) boundary

$\hat{\mathbf{n}}_{\text{GB}}$: unit normal to a grain boundary

ω_i: variable used to specify the depth of the interfacial free energy density minimum labeled i

ν: Poisson's ratio

p: pressure

t_{min}, t_{max}: the maximum and minimum $\chi(\hat{\mathbf{n}})$ values

θ: contact angle or one–half the dihedral angle

$\vec{u}$: rotation axis for crystallographic misorientation $\vec{\mathbf{R}}_\Phi$

w_P, w_S: weights for $P(\hat{\mathbf{n}})$ and $S(\hat{\mathbf{n}})$, respectively

$\vec{x}$: vector of position

$\vec{\xi}$: Cahn-Hoffman capillarity vector

Index